THE DEVELOPMENT, CHARACTERIZATION, AND APPLICATION OF BIOMIMETIC NANOSCALE ENZYME IMMOBILIZATION

A Dissertation
Presented to
The Academic Faculty

by

Nicholas R. Haase

In Partial Fulfillment
Of the Requirements for the Degree
Doctor of Philosophy in the
School of Chemistry and Biochemistry

Georgia Institute of Technology

December 2012

**THE DEVELOPMENT, CHARACTERIZATION, AND APPLICATION OF
BIOMIMETIC NANOSCALE ENZYME IMMOBILIZATION**

Approved by:

Dr. Nils Kröger, Advisor
Department of Chemistry and Food
Chemistry
Technical University of Dresden

Dr. Donald Doyle
School of Chemistry and Biochemistry
Georgia Institute of Technology

Dr. Adegboyega Oyelere
School of Chemistry and Biochemistry
Georgia Institute of Technology

Dr. Kenneth H. Sandhage
School of Materials Science and
Engineering
Georgia Institute of Technology

Dr. Glenn Johnson
Microbiology and Applied Biochemistry
Air Force Research Laboratory

Date Approved: July 19, 2012

This is dedicated to my Grandfathers, Henry Malcolm Haase and Harold Eugene Sargent.

ACKNOWLEDGEMENTS

TABLE OF CONTENTS

LIST OF TABLES

LIST OF FIGURES

LIST OF EQUATIONS

LIST OF SYMBOLS

A	Ampere
pKa	Acid Dissociation Constant
Δf	Change in frequency
Da	Dalton
n	Electrons in reduction reaction
E_{eq}	Equilibrium Redox Potential
Hz	Frequency
g	Gravitational force
pI	Isoelectric point
V_{max}	Maximum Velocity
K_M	Michaelis Constant
ε	Molar Absorptivity
E	Overall Redox Potential
η	Overpotential
ppm	Parts per million
Ω	Resistivity
S	Siemens
Σ	Summation
E^{0}	Thermodynamic Redox Potential
V	Voltage
wt%	Weight percentage

ζ Zeta potential

LIST OF ABBREVIATIONS

SPECIAL NOTE: The term "substrate" is used in both the biochemistry and materials science disciplines. Here it is used according to the biochemistry discipline, as the reactant in an enzymatic reaction. The term "foundation" is used in place of "substrate" in the materials science discipline.

AATCC	American Association of Textile Chemists and Colorists
AFM	Atomic Force Microscopy
Ag^+	Silver cation
AgNP	Silver Nanoparticle
c-AgNP	Citrate-capped Silver Nanoparticle
t-AgNP	Tiopronin-capped Silver Nanoparticle
BJH	Barrett-Joyner-Halenda
BS3	Bis(sulfosuccinimidyl) suberate
CNT	Carbon nanotube
CNT-BP	Carbon nanotube pressed "buckypaper" electrode
CD	Circular Dichroism Spectroscopy
cfu	Colony forming unit
CV	Cyclic Voltammetry
DMSO	Dimethyl Sulfoxide
DET	Direct Electron Transfer

DLS	Dynamic Light Scattering
E. coli	*Escherichia coli*
GOx	Glucose oxidase
GOx-PA	Glucose oxidase cross-linked to protamine
GT	GOx-PA/t-AgNP composite
GC	GOx-PA/c-AgNP composite
HRP	Horseradish peroxidase
Lac	Laccase
Lac-PA	Laccase cross-linked to protamine
Lac/PBSE	Laccase bonded to PBSE on CNT-BP
Lac-PA/PBSE	Lac-PA bonded to PBSE on CNT-BP
LbL	Layer-by-Layer
MIC	Minimum inhibitory concentration
MBC	Minimum bactericidal concentration
MWCO	Molecular weight cut off
MH	Mueller-Hinton medium
NaAc	Sodium acetate buffer
Na-P	Sodium phosphate buffer
oDS	Ortho-dianisidine dihydrochloride
PDMS	Polydimethyl siloxane
PEO	Polyethylene oxide
PA	Protamine
PBSE	1-pyrenebutanoic acid, succinimidyl ester

QCM	Quartz crystal microbalance
RH	Relative Humidity
RT	Room Temperature
RMS	Root mean squared
S. aureus	*Staphylococcus aureus*
Si-O	Silicon-oxide
SFG	Sum Frequency Generation Vibrational Spectroscopy
Ti-O	Titanium-oxide
TMOS	Tetramethyl orthosilicate
TiBALDH	Ti(IV)-bis(ammonium lactato) dihydroxide
TEM	Transmission electron microscopy
w:w	weight:weight ratio

SUMMARY

The utilization of enzymes is of interest for applications such as biosensors and biofuel cells. Immobilizing enzymes provides a means to develop these applications. Previous immobilization efforts have been accomplished by exposing surfaces on which silica-forming molecules are present to solutions containing an enzyme and a silica precursor. This approach leads to the enzyme being entrapped in a matrix three orders of magnitude larger than the enzyme itself, resulting in low retention of enzyme activity.

The research herein introduces a method for the immobilization of enzymes during the layer-by-layer buildup of Si-O and Ti-O coatings which are nanoscale in thickness. This approach is an application of a peptide-induced mineral deposition method developed in the Sandhage and Kröger groups, and it involves the alternating exposure of a surface to solutions containing the peptide protamine and then an aqueous precursor solution of silicon- or titanium-oxide at near-neutral pH.

A method has been developed that enables *in situ* immobilization of enzymes in the protamine/mineral oxide coatings. Depending on the layer and mineral (silica or titania) within which the enzyme is incorporated, the resulting multilayer biocatalytic hybrid materials retain 20 – 100% of the enzyme activity. Analyses of kinetic properties of the immobilized enzyme, coupled with characterization of physical properties of the mineral-bearing layers (thickness, porosity, pore size distribution), indicates that the catalytic activities of the enzymes immobilized in the different layers are largely determined by substrate diffusion. The enzyme was also found to be substantially stabilized against heat-induced denaturation and largely protected from proteolytic attack.

These functional coatings are then developed for use as antimicrobial materials. Glucose oxidase, which catalyzes production of the cytotoxic agent hydrogen peroxide, was immobilized with silver nanoparticles, can release antimicrobial silver ions. It is demonstrated that these two antimicrobial agents work in a synergistic manner for enhanced antimicrobial efficacy. Evidence of the proposed mechanism of synergy, namely enhanced release of silver ions by reaction of H_2O_2 with silver nanoparticles, is provided. Finally, the deployment of these materials in silk fibroins for development as wound dressings is also presented.

Protamine cross-linking was then extended to the oxygen-reducing enzyme laccase to explore the use of this modified enzyme in an enzymatic biocathode. In this application laccase accepts electrons from the electrode and uses them to reduce oxygen to water molecules. The protamine-cross-linked enzyme exhibits a higher degree of immobilization, better retention of activity once immobilized, and superior electrochemical activity versus the native enzyme.

Finally, preliminary research on the structure-function relationships of 16-mer peptides which adsorb to surfaces and deposit titanium oxide is presented. Specifically, the effect of content and distribution of arginine residues on the ability of peptides to adsorb to surfaces and subsequently deposit mineral oxides was investigated. The data demonstrate that surface adsorption of the peptides relies on both a critical number of arginine residues and their position within the peptide. Furthermore, the exchange of serine against arginine residues in surface-adsorbed peptides is detrimental to Ti-O deposition.

CHAPTER 1: Characterization of Peptide-induced LbL Mineralization

This chapter is distinct from, though represents a summary of, the studies presented in the following publication:

1.1 Abstract

This chapter details biomimetic layer-by-layer mineralization, which is used throughout this dissertation. Subsequent chapters involve the functionalization and application of mineral oxide layers formed using a peptide-induced mineral deposition method. The fundamental materials characteristics presented here will be used to understand the observations from those studies. Using the 31-amino acid peptide protamine from salmon sperm, multiple layers of silicon-oxide and titanium-oxide were deposited on silica foundations. The surface charge characteristics of this process are determined because electrostatic interactions are the driving force for the enzyme immobilization method used in herein. The deposition of the two mineral oxides is compared by measuring the thickness and roughness of the material deposited in each layer. As these functionalized coatings rely on small molecule diffusion, the pore sizes and distribution were characterized. This chapter concludes with a summary of the results and a discussion of future research directions in this area.

1.2 Introduction

1.2.1 Biomimetic Mineralization

In vitro Peptide-induced mineralization processes are inspired by biomineralization. Nature provides spectacular examples of biologically-formed minerals, such as the single domain nanomagnets of magnetotactic bacteria, the mechanically robust and intricate nano- to microscale patterned silica cell walls of diatoms, and the abrasion-resistant enamel of teeth.[1-4] Since biominerals are formed under mild reaction conditions (i.e., aqueous solution, ambient temperature and pressure, near neutral pH) biomimetic approaches to inorganic materials syntheses can provide new means for directly synthesizing composites of often-incompatible functional molecules (e.g., biomolecules and high temperature ceramics). The discovery of the role of long-chain polyamines in the biosynthesis of diatom silica,[5] along with subsequent identification of peptides that can induce the formation of non-biogenic minerals,[6-11] have led to the development of biomimetic strategies for the syntheses of oxide-bearing organic-inorganic hybrid materials in solution and on surfaces. In these approaches, lysine- or arginine-rich peptides and other polycationic organic polymers have been utilized as biomimetic analogs to the diatom long-chain polyamines.[12-25] The biosynthesis of silica in diatom algae is the basis for the biomimetic mineralization research approach used throughout this dissertation.

The method utilized herein for synthesizing ceramic coatings is a process established by Fang *et al*. employing the 31-residue peptide protamine (PA), with sequence H_3N^+-ARRRRSSSRPIRRRRPRRRTTRRRRAGRRRR-CO_2^-, as the mineralizing polyamine to enable the Layer-by-Layer (LbL) deposition of mineral

oxides.[26] The process of LbL mineralization occurs by the alternating exposure of surfaces to solutions containing protamine and a precursor of silicon- or titanium-oxide (Si-O or Ti-O, respectively) in aqueous solutions at near-neutral pH. PA adsorbs to the negatively-charged mineral surface and induces the deposition of Si-O or Ti-O upon exposure of the protamine-coated surface to the mineral precursor. This process results in a newly-formed surface with a negative charge, allowing for the adsorption of more protamine and subsequent mineral oxide deposition. A graphic representation of LbL mineralization is given in **Scheme 1.1**.

The significance of the electrostatic interaction of protamine and the mineral oxide surface was made evident by Fang and co-workers, who showed a decrease in titania deposition when LbL was attempted in solutions that were sufficiently acidic or contained high NaCl concentrations.[26] An acidic solution reduced the presence of negative charges on the mineral oxide surface, while high salt concentration screened the negative charges via Na^+ ions.
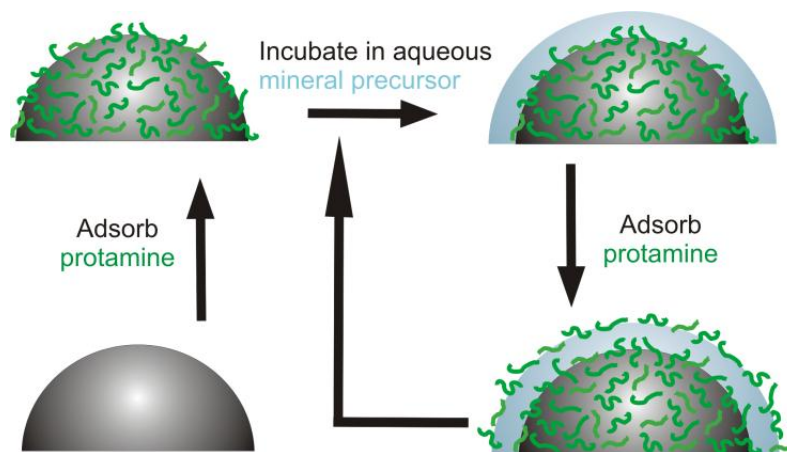
Scheme 1.1: The Protamine-induced Layer-by-Layer (LbL) deposition of Si-O or Ti-O.

LbL mineralization has been performed to coat Ti-O or Si-O on $CaCO_3$ spheres that contain entrapped enzymes.[24,25,27-31] After the deposition of multiple mineral oxide layers the $CaCO_3$ is dissolved and the protamine/mineral oxide coatings are free-standing, resulting in an enzyme-containing solution encased by the mineral oxide shell. LbL mineralization has also been utilized by Berrigan, *et al*. to deposit conformal Ti-O coatings which were subjected to high-temperature treatment to remove organic material, leaving behind a semi-conductive Ti-O material utilized in a photovoltaic cell.[32]

The studies above performed protamine-induced deposition of Si-O and Ti-O;[24,25,27-32] however, a comparison of the materials properties of these Si-O and Ti-O coatings have not been explored. In this chapter a quantitative comparison of the thickness and topography of protamine-induced Si-O and Ti-O coatings, as well as the differences in porosity of these materials, is presented. As protamine adsorption is an electrostatically-driven process, the electrostatic properties of the surfaces during LbL mineralization are compared. Subsequent chapters involve the immobilization of an enzyme during biomimetic mineralization and the diffusion of small molecules throughout Si-O and Ti-O coatings; therefore, the results presented in this chapter are important in interpreting those observations.

1.2.2 Introduction of Techniques used to Study LbL Mineralization

<u>1.2.2.1 Zeta Potential</u>

This research involves the electrostatic adsorption of molecules to particles suspended in pH-buffered solutions. Thus, studying the electrostatic properties of surfaces interacting with bulk solutions is important to gain an understanding of how the peptide adsorption and mineral deposition events of the LbL process may change during

material buildup. The electrostatic properties were evaluated using electrophoretic zeta potential measurements. This technique involves monitoring the movement of particles in a fluid under the influence of an electrical field by using an incident laser to determine their migration velocity; a treatment on the method is given below.

The zeta potential is a measure of a particle's electrostatic interaction with the bulk solution. A particle's surface charge attracts counter ions, some of which tightly bind to the particle surface in what is known as the Stern layer.[33] Ions in this layer stay bound to the particle surface and move with it in the presence of an external electric field. Outside the Stern layer is another layer of counter ions, called the diffuse layer, which are weakly bound to the particle. Ions in this layer have a weaker interaction with the particle than ions in the Stern Layer. Within the diffuse layer resides the boundary of a particle's hydrodynamic diameter, which is the size of the particle and its associated counter-ions. Ions within the hydrodynamic radius exchange with those outside the boundary, but will move with a particle under the influence of an electric field.[33] The Stern layer and ions within the hydrodynamic diameter create an electrical double layer around the particle. At the edge of the double layer there exists a "slipping plane." At this plane counter ions interacting with the particle will not migrate with the particle in the presence of an electric field. The electric potential in this plane is the zeta potential, which is lower in magnitude than the surface potential. Thus, the actual charge calculated in a zeta potential measurement is not the surface charge of the particle itself. A diagram of a particle and its interaction with counter ions out to the slipping plane can be seen in **Figure 1.2**.
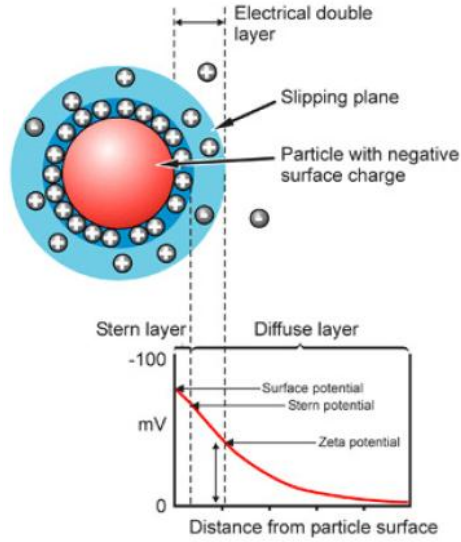
Figure 1.2: Diagram of the electrical double layer of a particle in solution.[33]

To determine the zeta potential of particles dispersed in a liquid, the sample is subjected to electrophoresis while monitoring the particle velocity. The electrical field is produced by placing two electrodes into a pH-buffered liquid and applying an electric potential to them. It must be noted that control of the pH is necessary to maintain a constant surface charge of the particle. The applied electric potential will cause particles to migrate towards the electrode of opposite charge. The higher the magnitude of charge of both particle and electrode, the faster a particle will move towards that electrode. As the particles migrate they cross the beam path of an incident laser and scatter the light; this scattered light is collected by a sensor. From the frequency with which particles scatter light the electrophoretic mobility, U_E, is calculated using Equation 1.1:

$$f = \frac{2U_E \sin(\theta/2)}{\lambda} \qquad\qquad (1.1),^{34}$$

where f is the scattering frequency, θ is the offset angle at which the detector is placed from the beam path, and λ is the wavelength of the light. Therefore, a suspension in

6

which particles move with greater velocity, due to having a higher zeta potential, will have more particles passing through the incident beam, scattering light more often in a given time. The electrophoretic mobility is proportional to the rate of scattering and is used to calculate the zeta potential using the Henry equation, which is written as

$$\zeta = \frac{2\varepsilon U_E f(\kappa a)}{3\eta}$$
(1.2),[35]

where ε is the dielectric constant of the dispersant, η is the viscosity of the dispersant, ζ is the zeta potential, and $f(\kappa a)$ is Henry's function, which relates the thickness of the electrical double layer, κ, to the radius of the particle, a. The form of Henry's function is

$$f(\kappa a) = \frac{2}{3}\left[1 + \frac{1}{2\left(1+\frac{2.5}{\kappa a\{1+2e^{-\kappa a}\}}\right)^3}\right]$$
(1.3).[36]

All measurements in my research were performed in aqueous media, where the $f(\kappa a)$ value used is 1.5. This value is known as the Smoluchowski Approximation, and is used in cases when κ is much smaller than a, meaning the electrical double layer is much smaller than the particle radius, which is common for particles in a dispersant containing ions. The dielectric constant and viscosity of the dispersant have to be included in the calculation since the former will affect electrical conduction through the fluid and the viscosity will act to retard the flow of particles through the fluid.

1.2.2.2 Atomic Force Microscopy

The thickness and roughness of each Si-O and Ti-O layer deposited was explored using Atomic Force Microscopy (AFM). AFM measurements yield quantified information of the deposited coatings by scanning a cantilever probe over the sample surface, as seen in **Figure 1.3**.[37] The probe, which is nanoscale in width at its tip, will deflect as it encounters different forces as it moves along the surface, bending upward

and downward. This changes the deflection angle of a laser incident on the back of the probe, moving the location where the laser strikes a photo-detector, and this movement is translated into a three-dimensional image (**Figure 1.3**).
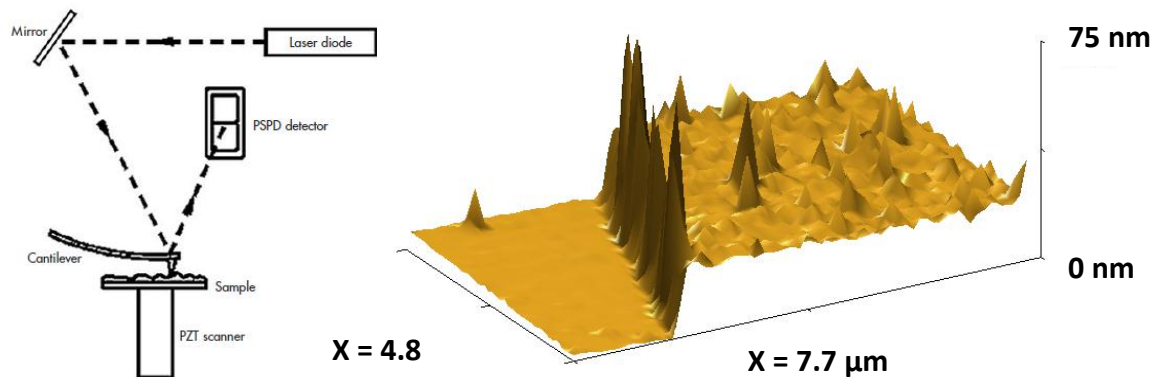
Figure 1.3: Diagram of Atomic Force Microscopy (left)[37] and a 3D image of five PA/Ti-O layers deposited onto a partially PDMS-masked Si wafer (right). PZT = Piezoelectric Table, PSPD = Position Sensitive Photo Diode.

The thicknesses of deposited Si-O and Ti-O coatings presented here were calculated by performing a Bearing Analysis on AFM scans across coated and uncoated regions of silicon wafers. In this analysis the z-axis is divided into planes and the number of data points in each plane are counted (**Figure 1.4**).[38] For LbL buildup, the two highest populations of data points will occur at the base silicon wafer height and the surface of the mineral oxide coating. Subtracting the former from the latter yields the height of the deposited material. The roughness is calculated using the method of root-mean-squares (RMS). This method is displayed in **Equation 1.4**; it is used because it accounts for the magnitude of roughness, and not the directionality.

$$x_{rms} = \sqrt{\frac{1}{n}(x_1^2 + x_2^2 + \cdots + x_n^2)} \hspace{2cm} (1.4).$$

In this equation "x" is the deviation of a peak or valley from the surface. As the value is squared, the direction of the change in elevation is negated. In simpler methods of roughness calculation the direction of elevation change is not negated. In that case a peak extending 5 nm above a surface and valley extending 5 nm below the surface would cancel out, falsely returning no roughness. These analyses will be important in discussing the immobilization of enzymes within mineral oxide layers in later chapters.
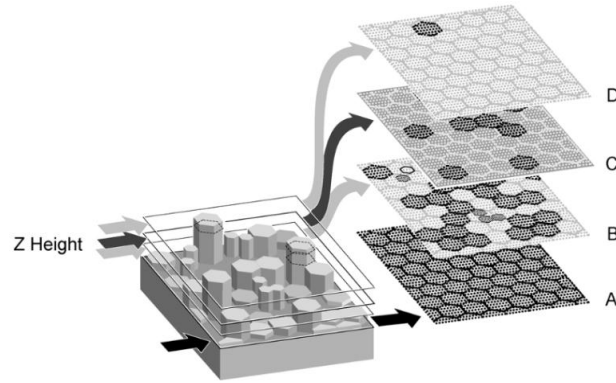
Figure 1.4: Example of Bearing Analysis procedure.[38] The black dots in planes A, B, C, and D denote the presence of features in that plane.

<u>1.2.2.3 Isothermal Gas Desorption</u>

The pore volume of the coated materials was measured using isothermal gas desorption measurements. In this method the sample is immersed in liquid nitrogen, the chamber pressure is incrementally increased with N_2 gas, and the gas infiltrates the pores within the material. As gas fills the pores, from small to large, it condenses to a liquid due to capillary forces. A representation of the adsorption process can be seen in **Figure 1.5**.[39] After the pores are completely filled the chamber pressure is incrementally decreased, and the liquid evaporates, equilibrating the pressure at each step.[40] During pore filling and evacuation the change in pressure is monitored during these steps. The porosity is then calculated using the model developed by Barrett, Joyner, and Halenda (BJH).[41]   Knowledge of the cumulative pore volume, as well as the distribution of pore sizes, yields information which will be valuable when discussing the diffusion of small molecules throughout the deposited coatings in later chapters.
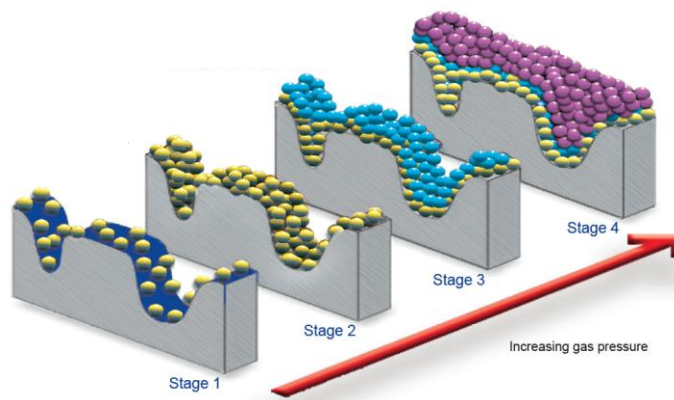
Figure 1.5: Isothermal gas adsorption and pore-filling.[39] Gas adsorbs to the surface and forms a monolayer (Stage 2, yellow). Once the solid surface is completely covered with gas molecules the pore voids begin to fill (Stage 3, blue). Once the pores are full the gas condenses to a liquid (Stage 4, purple).

1.3 Results & Discussion

1.3.1 Zeta Potential of LbL Coatings

Zeta potential measurements were performed at each step during the deposition of five mineral layers, which were formed with the mineral precursor silicic acid or TiBALDH for Si-O and Ti-O deposition, respectively. In every cycle, the adsorption of protamine inverted the surface charge from slightly negative to strongly positive (**Figure 1.6**). After deposition of the first mineral layer, the surface charge upon protamine adsorption (24.7 ± 1.8 mV) and mineral oxide deposition (-9.88 ± 4.06 mV for Si-O, -4.75 ± 2.78 mV for Ti-O) remains fairly constant, which suggests that the relative surface coverage of protamine adsorbed and mineral deposited were similar for each layer. The cause for Si-O surfaces exhibiting lower zeta potential than Ti-O surfaces is likely due a difference in pK_a, being 2-3 for Si-O and 4-5 for Ti-O.
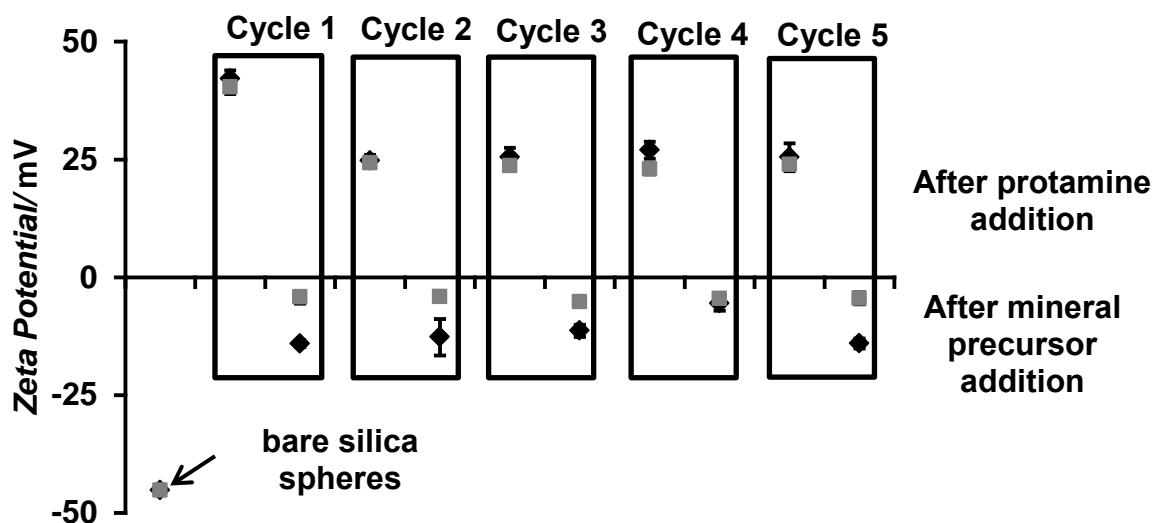
Figure 1.6:   Zeta potential of protamine-induced Si-O (black diamonds) or Ti-O (grey squares) LbL deposition on 150nm diameter silica spheres. All measurements were performed in 50 mM Tris-HCl pH 7.0. The results are the average and standard deviation of three independently measured samples.

1.3.2 Atomic Force Microscopy Analysis of LbL Coatings

To study the thickness and topography of the deposited mineral oxide layers AFM was employed. On partially-masked silicon wafers, cleaned with piranha solution, $1 - 5$ LbL cycles were conducted, and the mask was removed to perform AFM measurements across the mineral-coated and uncoated regions. The thicknesses of the mineral layers increased linearly with the number of LbL cycles, with a 4.8 ± 0.8 nm layer of Si-O and a 6.8 ± 1.0 nm layer of Ti-O deposited per cycle (**Figure 1.7**). These results demonstrate another difference in the materials properties of Si-O and Ti-O deposited by induction from the same peptide. This difference in thickness could be due to the lower pK_a of Si-O screening the positive charge of protamine with less Si-O deposited, which would decrease the attraction of silicic acid precursors to the nascent layer. However, it must be noted that the mineral precursors differ in their ligands, as silicic acid contains only hydroxyl groups, while TiBALDH consists of titanium chelated to two lactate ligands.
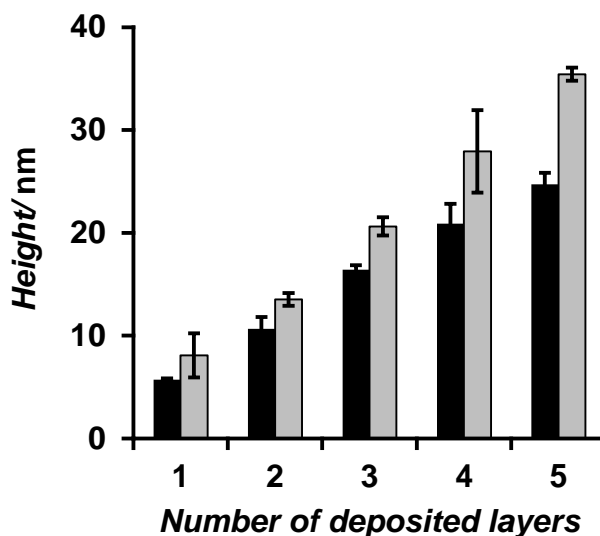
Figure 1.7: Thickness of Si-O-bearing (black) and Ti-O-bearing (grey) layers deposited on silicon wafers via protamine-mediated LbL mineralization. The results are the average and standard deviation of three independently measured samples.

The roughness of deposited Si-O and Ti-O layers is presented in **Figure 1.8**. While the surfaces remained relatively smooth during the first 3 deposition cycles (from 0.9 ± 0.2 nm for the starting silicon wafer to 1.6 ± 0.6 nm for Si-O-bearing coatings, and 2.0 ± 0.3 nm for Ti-O-bearing coatings), the surface roughness increased significantly in the fourth and fifth cycles, doubling to 3.3 ± 0.3 nm for Si-O-bearing coatings and nearly quadrupling to 7.7 ± 0.4 nm for Ti-O-bearing coatings after deposition of the fifth layer. These roughness measurements indicate that, as the buildup of layers continues outward from the foundation, the amount of mineral deposited becomes more varied. The roughness of Ti-O after five layers may be greater than that of Si-O because Ti-O is ~10 nm thicker than Si-O, and the increase in roughness may be correlated to distance from the starting foundation. Observations were not made past the fifth layer, which was the maximum number of layers deposited in my research.
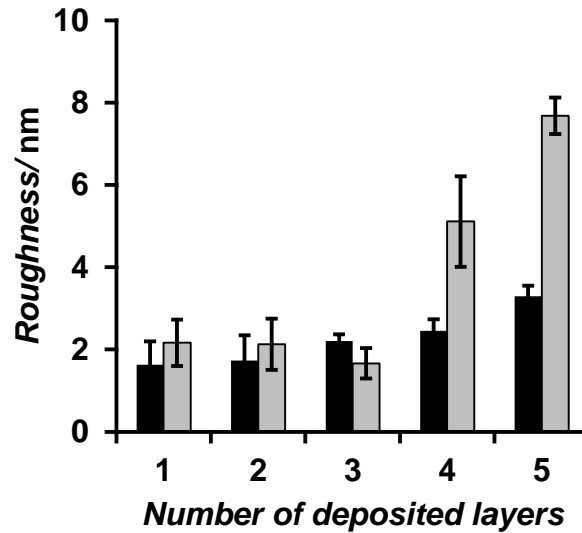
Figure 1.8: Roughness of Si-O (black) or Ti-O (grey) deposited on silicon wafers. The roughness was calculated on a plane-leveled 25 μm^2 area of deposited mineral oxide. The results are the average and standard deviation of three independently measured samples.

1.3.3 Barret-Joyner-Halenda Pore Size Analysis of LbL Coatings

Additional comparison between protamine-deposited Si-O and Ti-O coatings was performed by characterizing the cumulative pore volumes of five protamine/mineral oxide coatings on silica spheres via isothermal gas desorption and Barret-Joyner-Halenda (BJH) analysis. This study was conducted to ascertain the ability of small molecules to diffuse throughout the mineral matrix. The samples were tested without thermal pyrolysis of the organic content for an accurate representation of the cumulative pore volume of functionalized coatings detailed in the subsequent chapters. The cumulative volumes of mesopores (2 – 50 nm diameter) and macropores (>50 nm diameter) of Si-O coated particles were 13.2 ± 6.3% and 37.2 ± 8.8% greater, respectively, than the corresponding cumulative pore volumes of Ti-O coated particles (**Table 1.1**). The porosity is yet another difference in the properties of Si-O and Ti-O using the same method. Lastly, micropores (< 2 nm diameter) appeared to be absent in both Si-O and Ti-O coated articles when the data were analyzed using Density Functional Theory, which is specific for micropores.

Table 1.1: Cumulative pore volumes of LbL-coated silica spheres. Isothermal N_2 desorption was analyzed for silica spheres coated with five layers of Si-O or Ti-O. Pore volumes were calculated using BJH analysis. The results are the average and standard deviation of three independently measured samples.

	Volume (cc g^{-1})	
	Si-O	**Ti-O**
Mesopores (2 - 50 nm diameter)	1.07×10^{-2} $\pm 0.15 \times 10^{-2}$	0.94×10^{-2} $\pm 0.08 \times 10^{-2}$
Macropores (>50 nm diameter)	1.57×10^{-2} $\pm 0.30 \times 10^{-2}$	1.12×10^{-2} $\pm 0.24 \times 10^{-2}$

1.4 Conclusions

1.4.1 Summary of Results

This chapter presented research efforts into the basic characterization of protamine-induced layer-by-layer mineral deposition of Si-O and Ti-O. As this process is generally known to occur via electrostatic adsorption of protamine to the mineral surface, zeta potential measurements were conducted. This analysis revealed that the peptide adsorption and mineral deposition events, for both Si-O and Ti-O, yielded consistent zeta potential values. While protamine layers returned similar zeta potentials, Si-O layers consistently exhibited more negative zeta potential values than did Ti-O. Thus, mineral oxide layers can be deposited continuously as long as the electrostatic profile of the surface remains amenable for peptide adsorption. However, Atomic Force Microscopy measurements revealed the topography of the coatings to change with increased deposition cycles. While the roughness of each material began increasing upon deposition of the fourth layer, the roughness increase for Ti-O occurred at a faster rate than for Si-O. Since zeta potential measurements showed consistent values for all events of the process, this increase in roughness must be due to a reason other than the electrostatic characteristics of the surface. Ti-O layers were 40% thicker than Si-O layers, and the increased distance of newly-formed Ti-O surfaces from the foundation may contribute to the increased roughness. Pore size analysis of the five coatings on silica spheres revealed that Ti-O deposition results in a smaller, less porous mineral matrix than Si-O. Overall, Ti-O layers are thicker, less porous, and slightly rougher than Si-O layers. As the same peptide was used to deposit the mineral oxides, these analyses

indicate that either the precursor used or mineral oxide on which additional buildup occurs, or both, affects the resulting materials properties.

1.4.2 Future Directions

Research of protamine-induced mineral deposition which builds off the progress in this chapter can progress down a number of avenues. Investigations leading to the identification of the factors that cause the differences in materials properties could allow for tuning of the coating characteristics. As the mineral precursors used contained different ligands, attempting to deposit the same mineral oxide with different precursor ligands would indicate what affect factors such as chelation and ligand organic content have on the process. Si-O has been deposited here using silicic acid, $Si(OH)_4$, while Li *et al.* used Na_2SiO_3 with protamine to deposit Si-O. A direct comparison of Si-O layers deposited using these precursors would reveal any differences in the materials properties, and hence what effect the precursor ligand has on the deposition process.

This research was limited to the deposition of five mineral oxide layers. In that time the surface roughness of these layers began to increase. The retention of silicon wafer roughness in the first three deposited layers shows homogeneous mineral deposition, but as the roughness began to increase in the fourth and fifth layers it is suggestive that the deposition process becomes more heterogeneous across the surface. As such, the characterization of additional layers would reve-al to what extent this value increases, and if/when it reaches a consistent roughness value. Since the roughness increase occurred as layers were deposited further from the foundation surface, performing LbL of the same mineral oxides on different surfaces would yield insight into how the foundation affects the change materials properties as layer buildup continues.

Also, comparison of the LbL process performed on different foundation materials and morphologies, such as titanium surfaces and porous, hierarchical morphologies, is of importance in determining how the foundation affects the application of this process.

1.5 Materials & Methods

1.5.1 Materials

Silica spheres 1 μm in diameter were purchased from AngströmSphere (Bedford, MA, USA) and stored in 20 % ethanol in water solution at a concentration of 20 mg mL^{-1}. Silica spheres 150 nm in diameter were purchased from Bangs Laboratories (Fishers, IN, USA) and used as provided. Protamine sulfate (from salmon sperm, Grade X), Tris, Ti(IV)-bis(ammonium lactate) dihydroxyde (TiBALDH), and tetramethoxysilane (TMOS) were purchased from Sigma-Aldrich (St. Louis, MO, USA). Polydimethoxysilane (PDMS) base and curing agent were purchased from Dow Corning (Midland, MI, USA). MilliQ purified water (resistivity: 18.2 MΩ cm) was used for all solutions and washing steps throughout this dissertation.

1.5.2 Methods of Si-O and Ti-O Deposition and Characterization

1.5.2.1 Procedure for Si-O and Ti-O Deposition

The method for peptide-mediated LbL deposition of Si-O or Ti-O nanocoatings utilized in this work is based on previously-established methods requiring the alternating exposure of surfaces to protamine and the mineral precursor silicic acid or titanium (IV) bisammonium-lactato-dihydroxide (TiBALDH), respectively (**Scheme 1.1**).[26,32,42] In this research LbL mineral coatings have been formed using the following conditions. First, the spheres were washed three times in 50 mM Tris-HCl pH 8.0. All washes were

performed by centrifuging for 30 seconds at 16,100 x g, resuspending in the washing solution, and then vortex mixing for 10 seconds. After washing was completed, the spheres were resuspended in 0.1 M Tris-HCl pH 8.0, sonicated for three seconds (Misonix 3000 with tip K04711-90, Farmingdale, NY, USA), and an equal volume of freshly prepared 20 mg mL^{-1} protamine sulfate was added. The suspension was shaken at 1400 rpm for 15 min at RT, washed three times with 50 mM Tris-HCl pH 7.0, resuspended in 100 mM Tris-HCl pH 7.0, and sonicated for three seconds as above. For Ti-O deposition, to the spheres in 50 mM Tris-HCl an equal volume of 0.1 M TiBALDH was added, the suspension was shaken for 15 min, and then washed three times with 50 mM Tris-HCl pH 8.0. For Si-O deposition the protamine-coated spheres were resuspended in 50 mM Tris-HCl pH 7.0. Freshly prepared silicic acid (prepared by acid hydrolysis of TMOS as described elsewhere[42]) was added to a final concentration of 40 mM silicic acid, and the suspension was shaken for 5 minutes and then washed three times with 50 mM Tris-HCl pH 8.0. The sequence of "protamine adsorption - washing - incubation with mineral precursor - washing" was repeated until the desired number of mineral layers was produced. Upon deposition of the terminal layer the spheres were washed three times in 50 mM Tris-HCl pH 7 and stored in a suspension of the same buffer at 4 °C until further use.

For the deposition of mineral oxide coatings on silicon wafers, the wafers were cleaned with piranha solution (9 M H_2SO_4 and 4.5 M H_2O_2 in H_2O), then cut into sections of approximately 1 cm x 2 cm, rinsed extensively with water, and dried with a stream of compressed air. The dried wafers were coated with PDMS, which was freshly prepared by combining a 2:1 (w:w) base:curing agent ratio, and heated in an oven at 100°C for 1

hour. After curing, approximately half of the PDMS was removed by gently cutting through the polymer with a razor blade and peeling off one portion. LbL mineralization was performed as described above using freshly prepared solutions that were filtered (0.2 μm pore size). The following modifications were introduced: (i) adsorption/depositions were performed in a 48-well plate using 1 mL volumes per well in each step, (ii) samples were not shaken during incubations, and (iii) after deposition of the terminal layer, the coated wafers were washed three times with 5 mL H_2O, gently dried with a tissue, and placed in a parafilm-sealed container.

1.5.2.2 Zeta Potential Characterization of LbL Coatings

To track protamine adsorption and mineral deposition through zeta potential measurements, LbL mineralization was performed on 150 nm diameter silica spheres as described above. After each adsorption/deposition step, the spheres were washed three times in 50 mM Tris-HCl pH 7.0, then suspended in 1 mL 50 mM Tris-HCl pH 7.0, and subjected to measurements in a Malvern Instruments Zetasizer Nano ZS (Malvern Instruments, Worcestershire, United Kingdom). Data were averaged over 10 measurement runs, and data evaluation was performed using the Smoluchowski Approximation, silica material settings, and General Mode Analysis (Malvern Zetasizer Software v6.20). Samples were prepared in three independent experiments and the results were averaged.

1.5.2.3 Atomic Force Microscopy Analysis of LbL Coatings

AFM measurements of layer thickness and roughness were performed on LbL-coated wafers using a Veeco Dimension 3100 Scanning Probe Microscope (Veeco, Plainview, NY, USA) and the 10 nm radius general purpose probe of MikroMasch AFM

NSC36 (Mikromasch USA, San Jose, CA, USA). The protecting PDMS was removed and the samples were placed on the measurement stage and tapping-mode measurements were executed across the uncoated/PDMS coated boundary on a 15 µm x 30 µm area. For data analysis, the program Nanoscope Analysis v1.20 (Bruker Corp., Santa Barbara, CA, USA) was used. The silicon portion of each scan was plane-leveled and a Bearing Analysis was performed on the entire sample area. The thickness was calculated by recording the two highest peaks from the depth histogram and subtracting the lesser peak height from the greater peak height. To calculate roughness, a 5 µm x 5 µm area of deposited material was plane-leveled and the root mean square roughness was calculated in Nanoscope Analysis. For each layer, analysis was performed on three independently-prepared samples.

1.5.2.4 Barrett-Joyner-Halenda Pore Size Analysis of LbL Coatings

Barrett-Joyner-Halenda (BJH) cumulative pore volume analysis was performed on LbL coatings after depositing five layers of Si-O or Ti-O on 200 mg of silica spheres (1 µm diameter). After completion, the samples were washed three times in H_2O, resuspended in 5 mL H_2O, flash-frozen in liquid nitrogen, and lyophilized for 24 h. About 150 mg of each dry sample was placed in a 6 mm elliptical-bottom glass tube and degassed in a Quantachrome Autosorb AS-1 (Quantachrome Instruments, Boynton Beach, FL, USA) at room temperature. The samples were then backfilled with nitrogen gas, massed, and isothermal gas adsorption/desorption was performed in a liquid nitrogen bath (~77 K) using the same instrument with nitrogen gas as the adsorbate. A total of 40 adsorption and 40 desorption data points were collected for each sample. Three independent preparations of each sample were analyzed and averaged. BJH analysis was

performed on the isothermal desorption data to ascertain the pore volume in the meso- and macroporous ranges.

1.5.2.5 Table and Figure Data Analysis

The zeta potential data displayed are the average and standard deviation of the analysis of ten sample runs from each of three independently prepared samples. AFM thickness measurements represent the average and standard deviation of Bearing Analysis from three independently prepared samples. AFM roughness measurements represent the average and standard deviation of the root-mean-square roughness of a 25 μm^2 section from three independently prepared samples. Cumulative pore volume data are the average and standard deviation of BJH analysis performed on the desorption isotherm of three independently prepared samples.

1.6 References

1.   Lowenstam, H. A., and Weiner, S. (1989) *On Biomineralization*, Oxford University Press, Oxford.

2.   Jogler, C., and Schuler, D. (2009) Genomics, Genetics, and Cell Biology of Magnetosome Formation, *Annu. Rev. Microbiol. 63*, 501.

3.   Hamm, C. E., Merkel, R., Springer, O., Jurkojc, P., Maier, C., Prechtel, K., and Smetacek, V. (2003) Architecture and Material Properties of Diatom Shells Provide Effective Mechanical Protection, *Nature 421*, 841.

4.   Lichtenegger, H. C., Schoberl, T., Bartl, M. H., Waite, H., and Stucky, G. D. (2002) High Abrasion Resistance with Sparse Mineralization: Copper Biomineral in Worm Jaws, *Science 298*, 389.

5.   Kröger, N., Deutzmann, R., Bergsdorf, C., and Sumper, M. (2000) Species-specific Polyamines from Diatoms Control Silica Morphology, *Proc. Natl. Acad. Sci. 97*, 14133.

6.   Naik, R. R., Jones, S. E., Murray, J. C., McAuliffe, J. C., Vaia, R. A., and Stone, M. O. (2004) Peptide Templates for Nanoparticle Synthesis Derived from Polymerase Chain Reaction-Driven Phage Display, *Adv. Funct. Mater. 14*, 25.

7.	Dickerson, M. B., Naik, R. R., Stone, M. O., Cai, Y., and Sandhage, K. H. (2004) Identification of Peptides that Promote the Rapid Precipitation of Germania Nanoparticle Networks Via Use of a Peptide Display Library, *Chem. Commun. 40*, 1776.

8.	Sano, K., Sasaki, H., and Shiba, K. (2005) Specificity and Biomineralization Activities of Ti-Binding Peptide-1 (TBP-1), *Langmuir 21*, 3090.

9.	Dickerson, M. B., Jones, S. E., Cai, Y., Ahmad, G., Naik, R. R., Kröger, N., and Sandhage, K. H. (2007) Identification and Design of Peptides for the Rapid, High-Yield Formation of Nanoparticulate TiO2 from Aqueous Solutions at Room Temperature, *Chem. Mater. 20*, 1578.

10.	Dickerson, M. B., Sandhage, K. H., and Naik, R. R. (2008) Protein- and Peptide-Directed Syntheses of Inorganic Materials, *Chem. Rev. 108*, 4935.

11.	Kröger, N., Dickerson, M. B., Ahmad, G., Cai, Y., Haluska, M. S., Sandhage, K. H., Poulsen, N., and Sheppard, V. C. (2006) Bioenabled Synthesis of Rutile (TiO2) at Ambient Temperature and Neutral pH, *Angew. Chem. Int. Ed. 413*, 291.

12.	Brott, L. L., Naik, R. R., Pikas, D. J., Kirkpatrick, S. M., Tomlin, D. W., Whitlock, P. W., Clarson, S. J., and Stone, M. O. (2001) Ultrafast Holographic Nanopatterning of Biocatalytically Formed Silica, *Nature 413*, 291.

13.	Patwardhan, S. V., Mukherjee, N., and Clarson, S. J. (2001) The Use of Poly-L-Lysine to Form Novel Silica Morphologies and the Role of Polypeptides in Biosilicification, *J. Inorg. Organomet. Pol. 11*, 193.

14.	Patwardhan, S. V., and Clarson, S. J. (2002) Silicification and Biosilicification Part 1. Formation of Silica Structures Utilizing A Cationically Charged Synthetic Polymer At Neutral pH and Under Ambient Conditions Part 1. Formation of Silica Structures Utilizing A Cationically Charged Synthetic Polymer At Neutral pH and Under Ambient Conditions, *Polym. Bull. 48*, 387.

15.	Rodriguez, F., Glawe, D. D., Naik, R. R., Hallinan, K. P., and Stone, M. O. (2004) Study of the Chemical and Physical Influences upon in Vitro Peptide-Mediated Silica Formation, *Biomacromolecules 5*, 261.

16.	Knecht, M. R., and Wright, D. W. (2003) Functional Analysis of the Biomimetic Silica Precipitating Activity of the R5 Peptide from *Cylindrotheca fusiformis*, *Langmuir 20*, 4728.

17.	Kim, D. J., Lee, K. B., Chi, Y. S., Kim, W. J., Paik, H. J., and Choi, I. S. (2004) Biomimetic Formation of Silica Thin Films by Surface-Initiated Polymerization of 2-(Dimethylamino)ethyl Methacrylate and Silicic Acid, *Langmuir 20*, 7904.

18. Belton, D., Paine, G., Patwardhan, S. V., and Perry, C. C. (2004) Towards an Understanding of (bio)silicification: the Role of Amino Acids and Lysine Oligomers in Silicification, *J. Mater. Chem. 14*, 2231.

19. Jin, R. H., and Yuan, J. J. (2005) Synthesis of Poly(ethyleneimine)s–silica Hybrid Particles with Complex Shapes and Hierarchical Structures, *Chem. Commun. 41*, 1399.

20. Sewell, S. L., and Wright, D. W. (2006) Biomimetic Synthesis of Titanium Dioxide Utilizing the R5 Peptide Derived from *Cylindrotheca fusiformis*, *Chem. Mater. 18*, 3108.

21. Laugel, N., Hemmerle, J., Porcel, C., Voegel, J. C., Schaaf, P., and Ball, V. (2007) Nanocomposite Silica/Polyamine Films Prepared by a Reactive Layer-by-Layer Deposition, *Langmuir 23*, 3706.

22. Marner, W. D., Shaikh, A. S., Muller, S. J., and Keasling, J. D. (2008) Enzyme Immobilization via Silaffin-Mediated Autoencapsulation in a Biosilica Support, *Biomacromolecules 9*, 1.

23. Belton, D., Patwardhan, S. V., Annenkov, V. V., Danilovtseva, E. N., and Perry, C. C. (2008) From Biosilicification to Tailored Materials: Optimizing Hydrophobic Domains and Resistance to Protonation of Polyamines, *Proc. Natl. Acad. Sci. 105*, 5963.

24. Jiang, Y., Yang, D., Zhang, L., Li, L., Sun, Q., Zhang, Y., Li, J., and Jiang, Z. (2008) Biomimetic Synthesis of Titania Nanoparticles Induced by Protamine, *Dalton Trans. 37*, 4165.

25. Zhang, Y., Wu, H., Li, J., Li, L., Jiang, Y., Jiang, Y., and Jiang, Z. (2008) Protamine-Templated Biomimetic Hybrid Capsules: Efficient and Stable Carrier for Enzyme Encapsulation, *Chem. Mater. 20*, 1041.

26. Fang, Y., Wu, Q., Dickerson, M. B., Cai, Y., Shian, S., Berrigan, J., Poulsen, N., Kröger, N., and Sandhage, K. H. (2009) Protein-Mediated Layer-by-Layer Syntheses of Freestanding Microscale Titania Structures with Biologically Assembled 3-D Morphologies, *Chem. Mater. 21*, 5704.

27. Jiang, Y., Sun, Q., Jiang, Z., Zhang, L., Li, J., Li, L., and Sun, X. (2009) The Improved Stability of Enzyme Encapsulated in Biomimetic Titania Particles, *Mater. Sci. and Eng. C 29*, 328.

28. Jiang, Y., Yang, D., Zhang, L., Sun, Q., Sun, X., Li, J., and Jiang, Z. (2009) Preparation of Protamine–Titania Microcapsules Through Synergy Between Layer-by-Layer Assembly and Biomimetic Mineralization, *Adv. Funct. Mater. 19*, 150.

29.   Li, J., Jiang, Z., Wu, H., Zhang, L., Long, L., and Jiang, Y. (2010) Constructing Inorganic Shell onto LBL Microcapsule Through Biomimetic Mineralization: A Novel and Facile Method for Fabrication of Microbioreactors, *Soft Matter 6*, 542.

30.   Zhang, L., Jiang, Y., Shi, J., Sun, X., Li, J., and Jiang, Z. (2008) Biomimetic Polymer-inorganic Hybrid Microcapsules for Yeast Alcohol Dehydrogenase Encapsulation, *Reac. & Funct. Polym. 68*, 1507.

31.   Zhang, Y., Wu, H., Li, L., Li, J., Jiang, Z., Jiang, Y., and Chen, Y. (2009) Enzymatic Conversion of Baicalin into Baicalein by β-glucuronidase Encapsulated in Biomimetic Core-shell Structured Hybrid Capsules, *J. Molec. Catal. B: Enzym. 57*, 130.

32.   Berrigan, J. D., Kang, T. S., Cai, Y., Deneault, J. R., Durstock, M. F., and Sandhage, K. H. (2011) Titania Nanotubes: Protein-Enabled Layer-by-Layer Syntheses of Aligned, Porous-Wall, High-Aspect-Ratio TiO2 Nanotube Arrays, *Adv. Funct. Mater. 21*, 1693.

33.   Mangelsdorf, C. S., and White, L. R. (1990) Effects of Stern-layer Conductance on Electrokinetic Transport Properties of Colloidal Particles, *J. Chem. Soc. Faraday Trans. 86*, 2859.

34.   Eastoe, J., Rankin, A., Wat, R., and Bain, C. D. (2010) *Inter. Rev. in Phys. Chem.*, Vol. 20.

35.   Ohshima, H. (2002) Electrophoretic Mobility of a Charged Spherical Colloidal Particle Covered with an Uncharged Polymer Layer, *Electrophoresis 23*, 1993.

36.   Ohshima, H. (1994) A Simple Expression for Henry's Function for the Retardation Effect in Electrophoresis of Spherical Colloidal Particles, *J. Coll. Inter. Sci. 168*, 269.

37.   (2005) A Practical Guide to Scanning Probe Microscopy, Veeco Instruments, Inc.

38.   (2010) Nanoscope Analysis User Manual, Bruker Corporation.

39.   (2001) Gas Sorption Analysis, (Micromeritics, Ed.), Micromeritics, Norcross, GA.

40.   Kruk, M., and Jaroniec, M. (2001) Gas Adsorption Characterization of Ordered Organic-Inorganic Nanocomposite Materials, *Chem. Mater. 13*, 3169.

41.   Barrett, E. P., Joyner, L. G., and Halenda, P. P. (1951) The Determination of Pore Volume and Area Distributions in Porous Substances. I. Computations from Nitrogen Isotherms, *Vol. Area Distr. Por. Subst. 73*, 373.

42.   Kröger, N., Deutzmann, R., and Sumper, M. (1999) Polycationic Peptides from Diatom Biosilica That Direct Silica Nanosphere Formation, *Science 286*, 1129.

CHAPTER 2: Enzyme Immobilization in Mineral Matrices

This chapter is distinct from, though represents a summary of the studies presented in the following publication:

Haase, N.; Shian, S.; Sandhage, K.H.; Kröger, N. Biocatalytic Nanoscale Coatings Through Biomimetic Layer-by-layer Mineralization. *Adv. Funct. Mater.* **2011,** *21 (22),* 4243-4251.

2.1 Abstract

This chapter presents the functionalization of protamine-induced mineral oxide coatings detailed in Chapter 1 by immobilizing a modified enzyme during the LbL process. The discussion of results is linked to the materials properties presented in section 1.3. This discussion includes the influence of the surface chemistry of mineral oxide coatings on the immobilization of unmodified GOx, as well as the effect of materials properties on the catalysis and stability of the modified enzyme upon its entrapment within LbL coatings.

2.2 Introduction

2.2.1 Enzyme Encapsulation in Minerals

Perhaps one of the most impactful application areas for biomimetic mineral formation is the immobilization of functional enzymes within mineral matrices, as this process can be performed under mild reaction conditions. Immobilized enzymes are of substantial interest in a variety of areas, including biosensing, biofuel cells, and stereoselective organic syntheses.[1,2] Previously, immobilizing enzymes during biomimetic mineralization has been achieved by adding silicic acid and a mineral-

forming polycationic polymer to an enzyme solution,[3-14] or by fusing a silica-forming peptide with the enzyme before addition of silicic acid.[15,16] These methods have yielded entrapment of the enzyme inside the mineral phase and generally resulted in excellent retention and stabilization of enzyme activity.[17] However, these methods of enzyme immobilization result in the enzyme being suspended in solution (in its encapsulating mineral matrix) and not truly immobilized in the mineral.

2.2.2 Enzyme Immobilization on Surfaces

A largely unexplored aspect of enzyme immobilization is the application of this process on surfaces. Surface attachment of enzymes allows for the use of surface patterning techniques and foundation morphology to control enzyme distribution, while mineral entrapment can enable the syntheses of environmentally-robust functional composites (e.g., enzyme-bearing electrodes for biosensor arrays or biofuel cells).[1,2] Furthermore, the ability to generate a conformal, mineral-entrapped enzyme layer of nanoscale thickness on a foundation may allow for significant enhancement of the specific activity of the embedded enzyme (i.e., enzyme activity per mass), compared to the same enzyme immobilized within a thick (microscale) 3D mineral matrix, due to reduced diffusion distances and times for the substrates. Previously, efforts towards this end have been to attach enzymes to surfaces through chemical cross-linking, physisorption, or entrapment in polyelectrolyte films generated in a layer-by-layer process.[1,18]

To our knowledge, there are only two studies on the surface deposition of a mineral-entrapped enzyme.[5,13] In one study, Swartz and co-workers used piezoelectric inkjet printing to deposit a patterned array of polycationic dendrimer spots on a gold

surface, which was then exposed to a silicic acid solution containing Glucose oxidase (GOx) at pH 7.[13] The negatively-charged GOx molecules (pI = 4.2) bound electrostatically to the dendrimer-bearing regions as silica deposition was induced by the dendrimer, thus generating mineralized spots of ~20 μm diameter and ~4.5 μm height. The spots exhibited GOx activity that was stable over extended periods of time and were reusable without significant loss in activity. While this method allows for the rapid generation of micropatterned arrays of immobilized enzymes, it is not applicable to templates of complex (non-planar, sub-micron features) morphology. The thickness of the mineral matrix (~1 μm) was also several orders of magnitude larger than the hydrodynamic radius of the enzyme (~10 nm); that is, the enzyme was essentially entrapped in a 3D, rather than 2D, matrix. Furthermore, a low retention of enzyme activity (≤25%) was reported.[13] In a related approach, Ivnitski and co-workers have immobilized GOx on a carbon electrode surface by utilizing the silica-forming activity of surface-adsorbed lysozyme exposed to a silicic acid solution containing GOx.[5] This method also did not yield a continuous nanoscale mineral layer on the surface, and the authors reported a relatively low retention (18-25%) of enzyme activity after immobilization.[5] As both of these methods resulted in the enzyme entrapped in a surface-bound, microscale precipitate, the enzyme may not largely be immobilized near the surface of the foundation, but rather encased somewhere farther away within the mineral matrix.

2.2.3 The Motivation for Selecting Glucose Oxidase for Immobilization

GOx is a homodimeric oxidoreductase enzyme which exists as two 80 kDa monomers with two flavin adenine dinucleotide (FAD) molecules incorporated into the

center of the dimer as a cofactor.[19] FAD is a transient electron acceptor, accepting two electrons from glucose before transferring them to oxygen in the following reaction:[20]

$$O_2 + \quad \text{(glucose)} \xrightarrow{\text{GOx}} \text{(gluconolactone)} + H_2O_2 \qquad (2.1).[20]$$
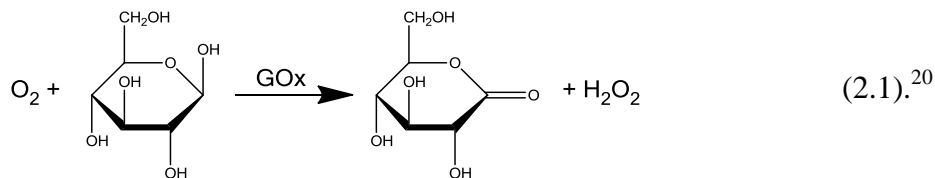
GOx is a widely-studied enzyme that has been incorporated as a glucose sensor due to its stability, and is also being investigated as a potential anodic enzyme in biofuel cell applications.[5,21] The research presented in Chapter 3 details the utilization of GOx as an antimicrobial agent since its enzymatic reaction produces cytotoxic hydrogen peroxide. In addition to an application stand-point, the fact that it is oft-studied makes it an ideal model enzyme; that is, the study of its immobilization within mineral oxides has the potential to yield information which could be useful for the immobilization of other enzymes.

2.2.4 The Study of Enzyme Properties upon Immobilization

As the effect of the immobilization process on the enzyme activity is presented here, a description of the properties studied is now given. Section 2.2.2 summarized two previous studies on the surface-immobilization of enzymes within mineral-oxide coatings which resulted in ≤25% retention of enzyme activity.[5,13] The activity of an enzyme is the rate at which it converts its substrate to the product at a given substrate concentration, expressed in units of moles min^{-1}. This metric was used to quantify the molar amount of active enzyme present in the mineral matrix and to calculate the retention of enzymatic activity upon immobilization by comparing it to standard GOx activity in solution. More detailed information on the enzyme's physical state and surrounding environment was

gained by investigating the Michaelis-Menten kinetic properties of the enzyme. The properties determined are the Michaelis constant, K_M, and the maximum velocity of the enzymatic reaction, V_{max}. K_M, which is expressed in terms of inverse concentration, is correlated to the enzyme's affinity for its substrate, yields information on any disturbance to the functional conformation of the enzyme upon immobilization. A rise in K_M indicates the enzyme has less affinity for its substrate. Decreases in an enzyme's V_{max} upon immobilization have been assumed to result from hindered substrate and product diffusion through the immobilizing matrix,[22-24] providing insight into the overall effect of the encapsulation matrix on the enzymatic reaction. Together these properties can reveal information into the effectiveness of this immobilization method.

Benefits of immobilization on protection of the enzyme from harsh environmental conditions were also investigated. Immobilization of enzymes within a mineral matrix often leads to increased stability towards elevated temperatures.[25] However, immobilization of GOx in silica has previously been found to result in both an increase[26] and decrease[27] in enzyme stability, depending on the conditions of immobilization, making this property a pertinent aspect to study. Increased thermal stability of enzymes inside mineral matrixes has been attributed to molecular confinement caused by entrapment of each enzyme molecule inside solvent-filled cavities that are only slightly larger than the enzyme molecule.[25] Inside such cavities, protein unfolding (which increases the protein volume) is inhibited, thus stabilizing the native conformation of the enzyme. To test whether this mechanism may also play a role in proteolytic stabilization of GOx-PA molecules that are immobilized within Ti-O and Si-O nanoscale coatings, protease accessibility experiments were performed on immobilized enzymes. These

stability studies were performed to assess the usefulness for deployment of this method in specific applications.

2.3 Immobilization of Native and Modified Glucose Oxidase

2.3.1 Immobilization of Native Glucose Oxidase

A modification of the protamine-enabled LbL deposition process was utilized for the stable adsorption of GOx on surfaces and its incorporation into mineral layers. GOx possesses an isoelectric point pI of 4.2,[28] and therefore did not bind to the negatively-charged Si-O or Ti-O surfaces at pH 7.0 (**Figure 2.1a**). However, after the mineral surfaces were rendered positively-charged by protamine adsorption, appreciable GOx binding was detected (**Figure 2.1a**).

To investigate whether adsorbed GOx could be immobilized within a mineral layer *in situ*, additional protamine was adsorbed onto the GOx-containing surfaces and these samples were incubated with either silicic acid or TiBALDH to allow the formation of new Si-O- or Ti-O-bearing layers, respectively. A relative GOx activity of 86.5 ± 3.6% was retained by the coating after Si-O deposition, with the supernatant possessing only 2.6 ± 0.1% of the GOx activity. This result indicated that most of the surface-adsorbed GOx molecules became entrapped in the newly-deposited Si-O layer but did lose some activity (this observation will be discussed in section 2.4.1). In contrast, GOx completely desorbed from the surface during Ti-O deposition (**Figure 2.1a**). The cause of the drastic difference in GOx retention by the coatings upon Si-O and Ti-O deposition is not entirely clear, but it may be related to the apparent enhanced binding of polycationic peptides/proteins to solid Ti-O relative to solid Si-O.[29] Therefore, during surface

mineralization GOx molecules bound to protamine may be displaced by the rapidly

increasing number of nascent negatively-charged polymeric Ti-O molecules.
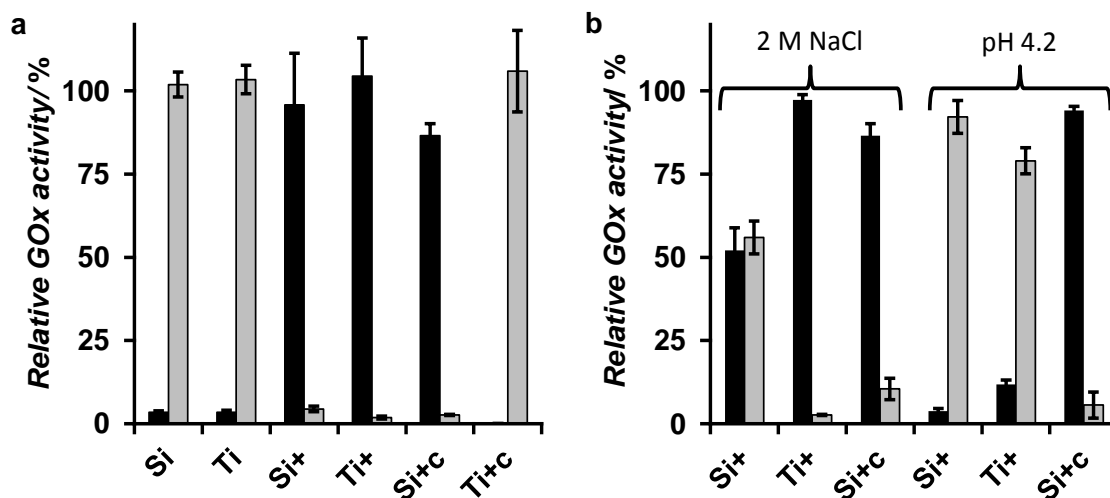
Figure 2.1: Immobilization and retention of GOx on silica surfaces. (a) GOx bound to silica spheres coated with Si-O (Si), Ti-O (Ti), protamine-coated Si-O (Si+) or Ti-O (Ti+), or inside new Si-O (Si+c) or Ti-O (Ti+c) coatings. GOx bound to the materials (black bars) or unbound (grey bars) was determined. After incubation of GOx-coated surfaces with silicic acid or TiBALDH, the amounts of GOx that were released (grey bars) or retained on the particles (black bars) were determined. **(b)** Analysis of the retention (black bars) and release (grey bars) of GOx from the indicated particles that were incubated in the presence of 2 M NaCl at pH 7 or 0.5 M phosphate-citrate at pH 4.2. The data are the average and standard deviation of three independent measurements.

To further evaluate the role of electrostatic interactions on GOx immobilization

the specimens were subjected to treatment with high salt concentrations and acidic pH

solutions. A high NaCl concentration was expected to screen electrostatic interactions of

protamine with both the mineral layer and GOx, whereas the acidification of the

suspension to pH 4.2 (the isoelectric point of GOx) was intended to weaken electrostatic

interactions by decreasing the negative charges on the mineral surfaces and rendering the

overall charge of GOx neutral. In the presence of 2 M NaCl 52.1 ± 6.8% of GOx

31

detached from protamine-coated Si-O, but essentially all of the GOx remained adsorbed to protamine-coated Ti-O (**Figure 2.1b**). When incubated at pH 4.2 the vast majority of GOx molecules detached from both protamine-coated Si-O ($92.2 \pm 4.9\%$) and protamine-coated Ti-O ($79.0 \pm 3.9\%$). In contrast, GOx immobilized within a freshly-deposited layer of Si-O remained almost completely bound to the silica spheres both during treatment with NaCl ($10.4 \pm 3.2\%$ detachment) and with pH 4.2 ($5.6 \pm 3.9\%$ detachment) (**Figure 2.1b**). These data indicate that: (i) GOx attachment to protamine-coated Ti-O surfaces is significantly less dependent on electrostatic interactions than GOx attachment to protamine-coated Si-O surfaces, and (ii) entrapment of GOx within a layer of silica drastically enhances retention of the enzyme, likely due to the inability of GOx to diffuse out of the material through the nanoscale pores observed via BJH analysis in section 1.3.3.

2.3.2 Immobilization of Modified Glucose oxidase

Since the immobilization of GOx was strongly dependent on the natural pI of the enzyme and sensitive to the ionic strength and pH of the solution, efforts were undertaken to modify GOx by cross-linking it to protamine to take advantage of the peptide's strong mineral-binding ability. This hybrid molecule is referred to as GOx-PA. DLS and zeta potential measurement showed that at pH 7 GOx-PA possessed a hydrodynamic diameter ($d = 22.4 \pm 3.7$ nm) more than twice that of GOx ($d = 10.4 \pm 5.0$ nm) and, unlike GOx, exhibited a positive zeta potential ($\zeta = +5.07 \pm 1.04$ mV for GOx-PA vs. $\zeta = -2.87 \pm 1.64$ mV for GOx). These data are consistent with the presence of multiple protamine molecules on GOx-PA. The cross-linked enzyme exhibited the same specific activity as

the unmodified enzyme (**Figure 2.2**), demonstrating that the attached protamine moieties did not impede catalysis.
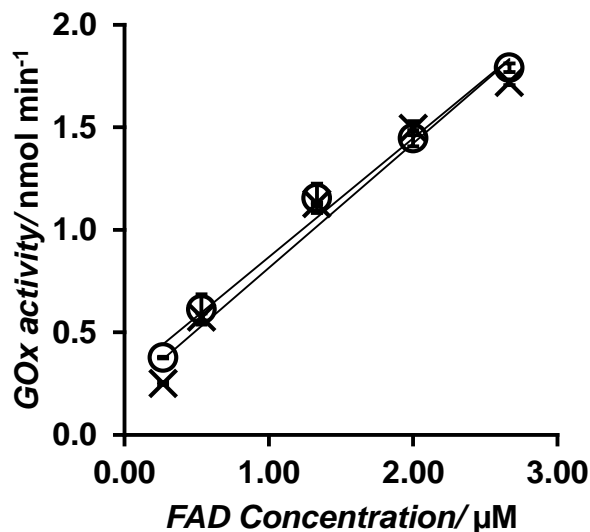
Figure 2.2: Enzymatic activity of GOx (X) and GOx-PA (O). Enzyme concentrations were determined by measurement of the absorbance at 451 nm of the permanently bound redox cofactor FAD (ε_{451} = 11,300 L mol^{-1} cm^{-1}). Each GOx monomer contains 1 FAD molecule. The data are the average and standard deviation of three independent measurements.

The retention of protamine function was tested by exposing Si-O- and Ti-O-coated spheres to GOx-PA. As expected, the enzyme was capable of adsorbing to the negatively-charged surfaces of Si-O- and Ti-O-coated silica spheres without the need for a protamine layer on the mineral surface (**Figure 2.3a**). Furthermore, GOx-PA remained attached to the surfaces even when exposed to a high salt concentration (2 M NaCl) or a low pH solution (pH 4.2), indicating the protamine moieties on GOx-PA were highly effective in mediating binding to Si-O and Ti-O surfaces (**Figure 2.3b**). As a result, GOx-PA remained attached not only during subsequent deposition of a silica layer, but

also during subsequent incubation with TiBALDH, thus allowing for the incorporation of the enzyme into a Ti-O layer *in situ* (**Figure 2.3a**).
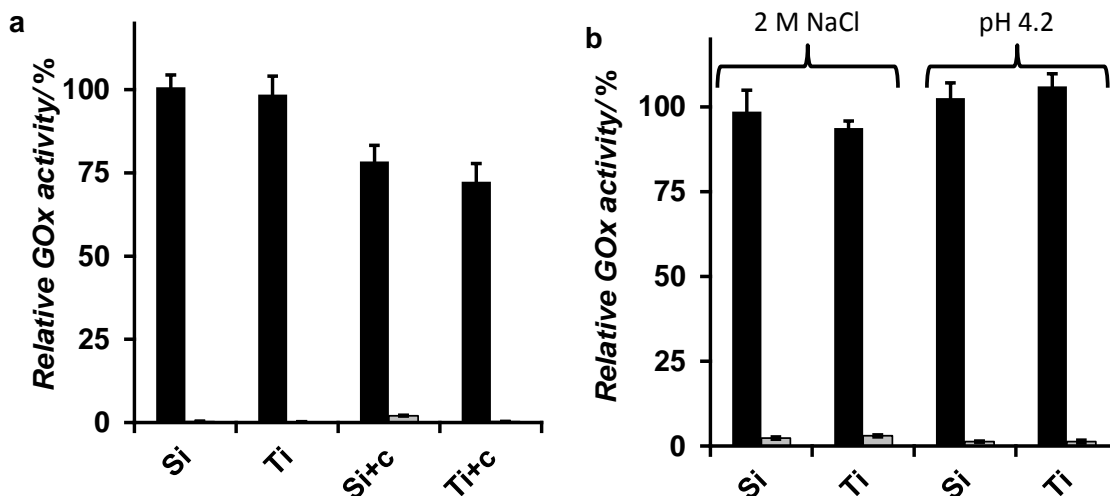
Figure 2.3: Immobilization and retention of GOx-PA on silica surfaces. Enzyme activities are normalized against the activity of free GOx-PA in solution. **(a)** GOx-PA was incubated with aqueous suspensions of silica spheres coated with Si-O (Si) or Ti-O (Ti), or within a new coating of Si-O (Si+c) or Ti-O (Ti+c). The amounts of GOx-PA bound (black bars) or unbound (grey bars) from the materials were determined. After incubation of GOx-PA-coated surfaces with with silicic acid or TiBALDH the amounts of GOx-PA that were released (grey bars) or retained on the particles (black bars) during mineral deposition were determined. **(b)** Analysis of the retention (black bars) and release (grey bars) of GOx-PA from the indicated particles that were incubated in the presence of 2 M NaCl at pH 7 or 0.5 M phosphate-citrate at pH 4.2. The data are the average and standard deviation of three independent measurements.

2.4 In situ LbL Immobilization of GOx-PA and Its Characterization

This section discusses the immobilization of GOx-PA in different layers during the LbL buildup of several protamine/mineral oxide coatings, whose material properties were discussed in Chapter 1. The effect of immobilization at different points of the LbL buildup on the enzyme properties is also discussed.

2.4.1 LbL Incorporation of GOx-PA

The utility of GOx-PA for incorporation *in situ* was performed by immobilization into selected specific layers during the buildup of five mineral layers, which were entirely Si-O or Ti-O, in a given specimen. Interestingly, the GOx-PA activities of the different enzyme-bearing samples were dependent on both the mineral oxide and layer in which the enzyme was immobilized. The activity of the enzyme was modestly higher in Si-O coatings as compared to Ti-O coatings and also increased as the enzyme was placed closer to the outer surface (**Figure 2.4**). Indeed, GOx-PA immobilized in the fourth of five Si-O-bearing layers exhibited essentially the same activity as the enzyme in solution, while a slightly lower activity level resulted when the enzyme was immobilized in the corresponding Ti-O coatings. In all cases these differences in enzyme activities could not be attributed to varying degrees of protein incorporation into the mineral layers, as only very low amounts of enzyme ($\leq$7.2%) remained unincorporated (**Figure 2.4**). Despite the high yield of enzyme incorporation *in situ*, GOx-PA immobilized within the first Si-O or Ti-O layer (Si1 or Ti1, respectively, **Figure 2.4**) exhibited only $\leq$25.4% activity, which is similar to the activities in separate reports by Schwartz *et al.* and Ivnitski *et al.*[5,13] In contrast, GOx-PA immobilized in the adjacent second layer, and fourth layer, exhibited >72.3% activity. Also, GOx-PA immobilized directly on the silica spheres, on layer 2, or on layer 4 without subsequent mineralization exhibited essentially the same activity as free GOx-PA in solution (**Figure 2.5**), indicating the loss of activity occurs after mineral oxide coating.

While the exact molecular reasons for the drastically reduced activity of the enzyme immobilized in layer 1 of Si-O or Ti-O coatings are unclear, the effect is

apparently a consequence of the characteristics of the interface between silica spheres and the first *in situ*-deposited Si-O and Ti-O layers. Local gradients in hydration, oxide concentration, and/or the concentration of surface charges at the interface between the silica sphere and these first deposited layers may differ from such gradients at the interfaces between subsequent deposited layers. Thus, local conditions in the first mineral layer could be different from the conditions in other layers, which would mean GOx-PA in the first layer would be in a different local environment than in other layers.
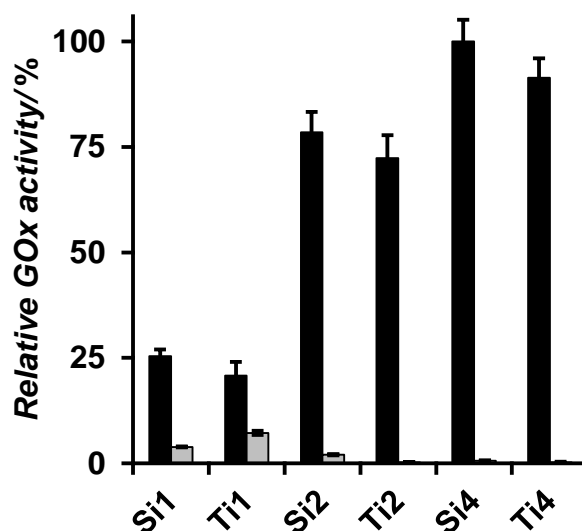
Figure 2.4: Layer dependence of enzyme activity. Enzyme activities are normalized against the activity of free GOx-PA in solution. GOx-PA has been immobilized *in situ* during LbL buildup of five layers of either Si-O (Six) or Ti-O (Tix) on silica spheres (x = layer in which GOx-PA was immobilized). Enzyme activities bound to the particles (black bars) and in the supernatants (grey bars) were determined. The data are the average and standard deviation of three independent measurements.
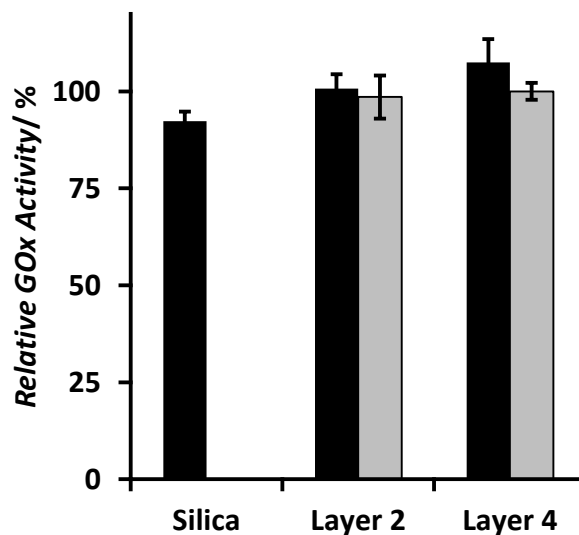
Figure 2.5: Activity of GOx-PA on surfaces. Enzyme activities are normalized against the activity of free GOx-PA in solution. The activities of GOx-PA adsorbed on bare silica spheres ("Silica"), Si-O (black) and Ti-O (grey) surfaces generated by two cycles ("Layer 2") and four cycles ("Layer 4") of LbL mineralization are shown. The data are the average and standard deviation of three independent measurements.

2.4.2 Additive Effect of Enzyme Activity with Multiple GOx-PA Layers

From the results in section 2.4.1 it can be inferred that the LbL mineralization process should lend itself to repeated immobilization of enzyme molecules in multiple mineral layers, which would allow for significant amplification of enzyme activity in a given system. To investigate this possibility five Si-O layers were deposited on silica spheres and GOx-PA was immobilized in the second, third, and fourth layers (this product was named "Si{2-4}"). As controls, three different LbL-mineralized products were generated which carried GOx-PA only in layer 2 (Si2), 3 (Si3), or 4 (Si4). For each control a similarly high amount of enzyme became immobilized (i.e., no significant amounts of enzyme remained unbound), and the sum of the enzyme activities of the Si2, Si3, and Si4 particles was virtually identical to the activity of the Si{2-4} particle. This

demonstrates that LbL enzyme immobilization and the resulting net enzyme activity is additive (**Figure 2.6**), and also that immobilization of the enzyme in one layer did not affect immobilization of the enzyme in another layer.
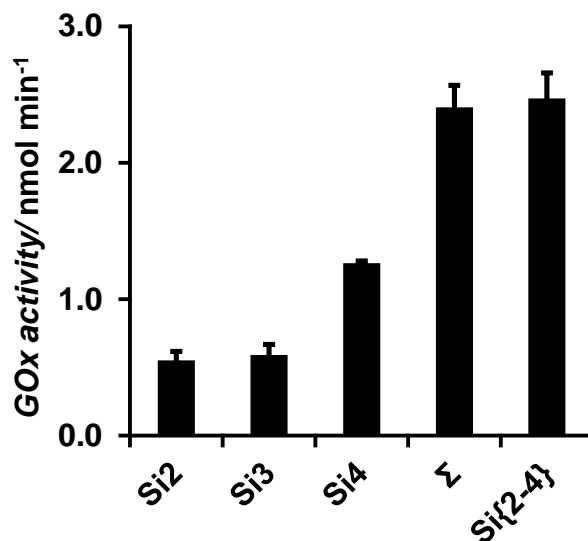
Figure 2.6: *In situ* **Immobilization of GOx-PA in multiple layers during LbL mineralization.** The GOx-PA activities of particles bearing five Si-O layers in which GOx-PA has been incorporated *in situ* into the second (Si2), third (Si3), or fourth layer (Si4). The bar denoted Σ represents the arithmetic sum of the activities of samples Si2, Si3, and Si4. The bar denoted Si{2-4} is the enzyme activity of a particle bearing five Si-O layers in which GOx-PA has been successively incorporated *in situ* into the second, third, and fourth layers. The data are the average and standard deviation of three independent measurements.

2.4.3 Characterization of Immobilized GOx-PA Kinetics

The effects of nanoscale confinement on the kinetic properties of the immobilized GOx-PA molecules, the Michaelis constant (K_M) and the maximum velocity (V_{max}), were determined. These experiments revealed the values of K_M (**Figure 2.7a**) for the different enzyme-loaded materials (average values between 22.4 – 31.9 mM), and free GOx-PA in

solution (33.1 ± 6.0 mM) to be similar. As K_M is correlated to the affinity of an enzyme for its substrate, this result indicates that the functional conformation of GOx-PA is not significantly affected by immobilization in different Si-O or Ti-O layers. In contrast, V_{max} varied substantially between the different samples (**Figure 2.7b**). The V_{max} values were generally lower for GOx-PA immobilized within a given Ti-O layer compared to the corresponding Si-O layer, and V_{max} values decreased when the enzyme was positioned in deeper coatings (farther from the outer surface) (**Figure 2.7b**).

The trend in V_{max} values was in agreement with the observed differences in enzyme activities of the samples (see **Figure 2.4**). Therefore, it can be concluded that the decrease in V_{max} was largely responsible for the significantly decreased activities of GOx-PA immobilized in mineral layers one (Si1, Ti1) and two (Si2, Ti2) relative to GOx-PA within mineral layers four (Si4, Ti4). The decline in V_{max} as the enzyme is placed further from the outer surface can be explained by the enzyme's substrate having to diffuse through a greater distance in the material matrix to reach the enzyme. The increased thickness, decreased pore volume, and prevalence of smaller pores in Ti-O coatings versus Si-O coatings (in section 1.3) accounts all provide additional hindrance of glucose diffusion in Ti-O, accounting for lower V_{max} in the corresponding specimens (Si4 and Ti4, Si2 and Ti2).
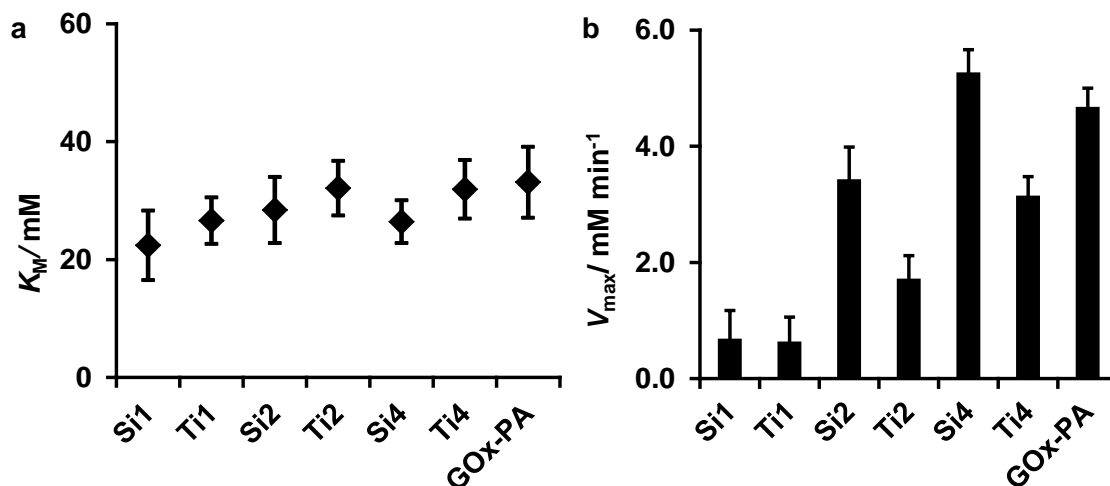
Figure 2.7: **Layer dependence of kinetic properties of GOx-PA.** GOx-PA immobilized *in situ* in particles containing five Si-O (Si*x*) or Ti-O (Ti*x*) layers on silica spheres (*x* = layer in which GOx-PA was immobilized, GOx-PA = the enzyme in solution). **(a)** Michaelis constant (K_M), **(b)** maximum velocity (V_{max}). The data are the average and standard deviation of three independent measurements.

2.4.4 Enhanced Stability of Immobilized GOx-PA

2.4.4.1 Thermal Deactivation of GOx-PA

To investigate the thermal stability of GOx-PA-loaded Si4 and Ti4 particles were incubated at 65 °C for 48 hours. Aliquots were periodically removed and assayed for GOx activity. A rapid decrease in activity for GOx-PA in solution was observed, with complete loss of activity after 90 min; this observation was consistent with previous results observed for the thermal denaturation of GOx in solution.[26] In contrast, GOx-PA immobilized in Si-O and Ti-O retained 41.4 ± 7.5% and 21.9 ± 1.7% activity, respectively, after 90 min. Even after 3 hours of incubation at 65 °C, immobilized GOx-PA still exhibited 27.6 ± 4.0% (Si4) and 16.4 ± 2.8% (Ti4) of the original activity (**Figure 2.8**).
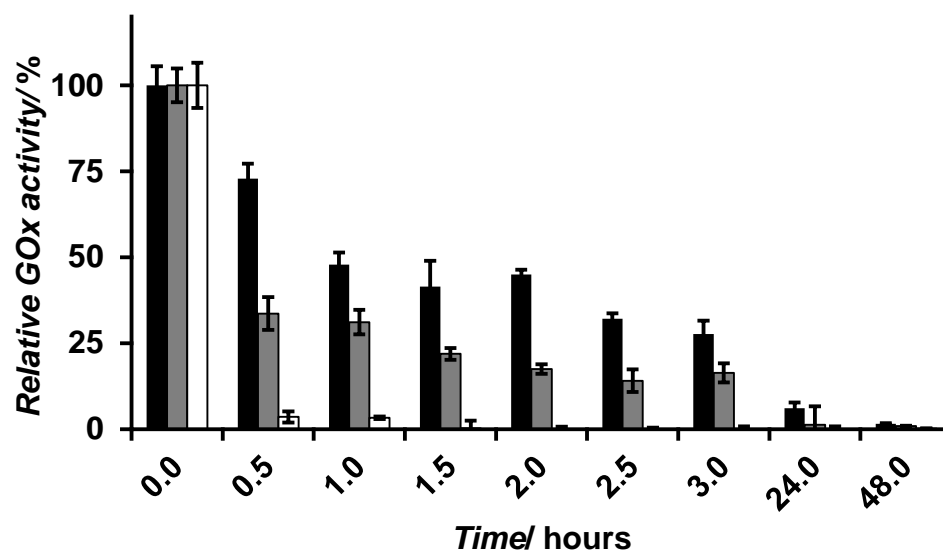
Figure 2.8: Thermal deactivation of immobilized GOx-PA. Time course of thermal deactivation at 65 °C of GOx-PA in solution (white bars), immobilized in Si-O (black bars), or Ti-O (gray bars). GOx-PA was deposited in layer 4 of LbL-mineralized particles containing a total of 5 mineral layers. Activity data were normalized to the sample activity at the beginning of the experiment (0 hours). The data are the average and standard deviation of three independent measurements.

2.4.4.2 Protection from Proteolysis

GOx-PA-loaded Ti4 and Si4 particles and free GOx-PA were exposed for 24 hours to pronase (a highly-active protease mixture[30]). While >75% of free GOx-PA in solution was degraded, >81% of the immobilized GOx-PA activity remained in the Ti4 and Si4 samples (**Figure 2.9**). This result is consistent with the GOx-PA molecules being largely protected from protease attack inside nanoscale cavities. This protection is likely due to the pore sizes in the coatings, which prevent the enzyme from diffusing out, retarding inward diffusion of the pronase proteases.
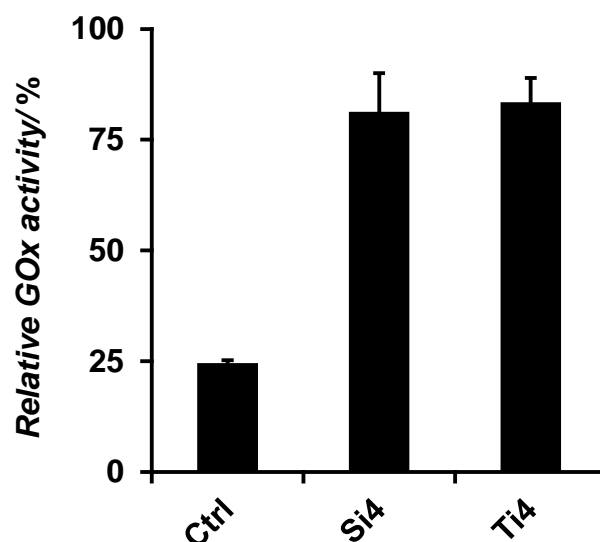
Figure 2.9: Protection from proteolysis of immobilized GOx-PA. Enzyme activities of GOx-PA in solution (Ctrl), immobilized in Si-O (Si4), or immobilized Ti-O (Ti4) after 24 hours of incubation with pronase.   GOx-PA was deposited in layer 4 of LbL-mineralized particles containing a total of 5 mineral layers. Activity data were normalized to the sample activity at the beginning of the experiment (0 hours).   The data are the average and standard deviation of three independent measurements.

2.5 Conclusions

2.5.1 Summary of enzyme *in situ* LbL immobilization

This work demonstrates, for the first time, that a peptide-enabled LbL coating process, involving the use of a properly-modified *and* properly-distributed functional enzyme within the nanoscale bio-organic/inorganic coating, can allow for full retention of enzymatic activity while providing enhanced stability against thermal and biochemical (protease) degradation. A hybrid molecule comprised of a mineralizing peptide (protamine, PA) covalently bound to a redox enzyme (glucose oxidase, GOx), was utilized to control the incorporation of the enzyme at a high yield within nanoscale bio-organic/inorganic coatings.   The controlled positioning of the enzyme within the

nanoscale mineral oxide coating was accomplished via insertion of GOx-PA at the appropriate stage of this LbL process. By using this approach to locate GOx-PA at the fourth of five Si-O layers full retention of the enzyme activity was achieved; appreciable enhancements in thermal stability and resistance to protease (pronase) attack were also realized. It was also observed that the enzyme could be incorporated into multiple layers during the coating process, with the catalytic activity being additive across all layers. The effect of immobilization on the enzymatic activity was correlated with the materials properties discussed in section 1.3 and show this immobilization method does not affect the enzyme's functional conformation, but that diffusion of the enzyme's substrate and product through the mineral matrix largely determines the enzyme activity.

2.5.2 Method Development Outlook

While the method presented herein is a general method for the two-dimensional immobilization of enzymes, further development can occur in two key aspects, biochemical and material. Biochemically, it was shown that the enzyme could be deposited in multiple layers and immobilization in one layer did not affect the activity in another. Therefore, studies in which multiple enzymes are immobilized in multiple layers are of interest. In these multi-enzyme cascades, the product of one enzymatic reaction would be the substrate for another, yielding a multifunctional material with the capability to usher a molecule through multiple processing steps, possibly mimicking a biochemical pathway *in vitro*.

From a material standpoint, this method can be developed for enzyme immobilization on other foundations appropriate for specific applications. Silica spheres were chosen for their ease of use in this study; however, this same method could be

developed for any surface with a negative charge at neutral pH, such as silk textiles. Utilizing other mineral oxide-depositing peptides and polymers, such as polyethyleneimine (PEI), would enable the comparison of different mineral precipitating agents in functional materials. This approach would allow the generation of functional and robust biomolecule-bearing nanoscale composite coatings for a variety of highly-demanding (bio)technological applications.

2.6 Materials and Methods

2.6.1 Materials

All materials used in section 1.2.1 were used in this section. Glucose oxidase (from *Aspergillus niger*), horseradish peroxidase (HRP, from *Amoracia rusticana*), and D-glucose were purchased from Sigma-Aldrich (St. Louis, MO, USA). *o*-dianisidine dihydrochloride (oDS), sodium chloride, and sodium acetate (NaAc) were purchased from VWR (Radnor, PA, USA). Bis(sulfosuccinimidyl) suberate (BS3) was purchased from Thermo Scientific (Rockford, IL, USA). HEPES was purchased from VWR (Radnor, PA, USA).

2.6.2 Procedure and Conditions for Glucose Oxidase Adsorption and Retention

2.6.2.1 Immobilization of GOx

For adsorption of GOx to protamine-coated spheres (prepared as described in section 1.2.2.1), 3 μg of GOx was added to 1 mg of spheres in 1 ml of 50 mM Tris-HCl pH 7.0 and shaken at 1400 rpm at room temperature for 15 min. The spheres were then washed three times in 50 mM Tris-HCl pH 7.0 and resuspended in 50 mM Tris-HCl pH 7.0. The pellet and all supernatants were tested for GOx activity.

For incorporation of GOx into mineral layers, spheres bearing surface-adsorbed GOx were washed three times in 50 mM Tris-HCl pH 8.0 and incubated with 10 mg of protamine in 50 mM Tris-HCl pH 8.0 while shaking at room temperature for 15 min. Next, the spheres were washed three times in 50 mM Tris-HCl pH 7.0 and mineral deposition was performed as described in section 1.2.2.1. The spheres were then washed three times in 50 mM Tris-HCl pH 7.0 and resuspended in 50 mM Tris-HCl pH 7.0. The pellet and all supernatants were tested for GOx activity.

2.6.2.2 Assay of GOx Activity

For assays of GOx in solution, 25 µL of 8 mM of oDS, 18 µL of 1 M D-glucose, 10 µL of 10 mg mL^{-1} HRP, and 10 µL of 1 M NaAc pH 5.1 were mixed, and H$_2$O was added to a final volume of 200 µL. The reaction was started by the addition of GOx, incubated for 20 minutes at room temperature, and the absorbance was recorded at 460 nm. For assays of immobilized GOx, the enzyme-containing particles were resuspended in 18 µL of 1 M D-glucose and 192 µL of 50 mM NaAc pH 5.1, then incubated for 20 minutes at room temperature under constant shaking. The reaction mixture was then filtered through a 0.2 µm pore size filter, and 100 µL of the filtrate was combined with 25 µL of 8 mM oDS and 10 µL of 10 mg mL^{-1} HRP, incubated for 2 min at room temperature, and the absorbance at 460 nm was recorded. All absorption measurements were recorded on a Biotek Synergy 2 multi-well plate reader (Biotek, Winooski, VT, USA). As negative controls, reaction mixtures without GOx or with GOx but without D-glucose were recorded. The percentage of "relative GOx activity" was obtained by comparing the activity of GOx immobilized within a given specimen with that of free GOx in solution.

Desorption of GOx from coated spheres was tested after incubation with 2 M NaCl in 50 mM Tris-HCl pH 7.0 or incubation with 0.5 M phosphate-citrate pH 4.2 solution; both were performed for 30 min at room temperature. The suspensions were then washed three times in 50 mM Tris-HCl pH 7.0. The pellet and all supernatants were tested for GOx activity.

2.6.3 Crosslinking of Glucose Oxidase to Protamine

GOx and protamine (PA) were chemically cross-linked using the homobifunctional amine-reactive molecule bis(sulfosuccinimidyl) suberate (BS^3).[31] Cross-linking was performed using 1:10 GOx:protamine and 1:40 GOx:BS3 molar ratios. A typical cross-linking reaction was conducted as follows: 1 mg GOx and 0.51 mg PA were dissolved in a 1 ml solution containing 10 mM HEPES pH 7.5 and 120 mM NaCl. Subsequently, 0.286 mg BS3 was added and the reaction solution was incubated for 1 hour at room temperature on a rotator mixer, followed by quenching with the addition of 1 M Tris-HCl pH 7.5 to a final concentration of 100 mM. The reaction solution was then dialyzed against three changes of 50 mM NaAc pH 5.1, flash-frozen in liquid nitrogen, lyophilized for 24 h, diluted to a GOx concentration of 1 mg mL^{-1} (determined by absorption of FAD), and stored at 4 °C.

2.6.3.1 Optical Spectroscopy of GOx-PA

To ascertain the concentration of GOx-PA solutions after lyophilization linear optical spectroscopy measurements were taken using the absorption of the GOx cofactor FAD, which has an absorption peak at 451 nm.[32] This method was chosen when BCA

protein quantification assays resulted in the formation of precipitates in GOx-PA samples.

<u>2.6.3.2 Dynamic Light Scattering Measurement</u>

The size of native and cross-linked GOx was determined using Dynamic Light Scattering (DLS) measurements. These measurements were performed using a 0.1 mg mL^{-1} concentration of the enzyme in 50 mM Tris-HCl pH 7 in a Malvern Instruments Zetasizer Nano ZS (Malvern Instruments, Worcestershire, United Kingdom). Data was recorded using the 173° Backscatter measurement angle and analyzed using the protein material specification and protein analysis mode in the Malvern Zetasizer Software (v6.20). Samples were prepared in three independent experiments, each averaged across ten consecutive data runs, and the results of the three measurements were averaged.

2.6.4 Procedure for LbL Immobilization and Characterization of GOx-PA

The incorporation of GOx-PA into mineral layers was performed using the LbL mineralization process detailed in section 1.5.2. GOx-PA was immobilized during the protamine adsorption step(s) of this process and is described briefly as follows. 3 µg of GOx-PA and 10 mg of protamine were added to 1 mg of spheres in 1 ml of 50 mM Tris-HCl pH 8.0. Subsequent mineral deposition was then performed as described in section 1.5.2. The pellet and all supernatants were saved and tested for GOx-PA activity using the procedure stated in section 2.6.2.2.

To obtain V_{max} and K_M values of both free and immobilized GOx-PA the enzyme-bearing particles, with equal amounts of enzyme incorporated, were resuspended at identical particle densities (1 mg spheres per mL) and assay times of the different constructs were adjusted to yield equal overall H_2O_2 production for the different

specimens. Assay times were as follows: Si4 – 10 min, Si2 and Ti4 – 15 min, Ti2 – 20 min, and Si1 and Ti1 – 50 min. The assay time for GOx-PA in solution was 4 min. Within these assay times H_2O_2 production was well within the linear regime, approximating the initial velocities of the reaction. All samples were assayed as described in section 2.6.2.2 with the exception of the glucose concentration, which was varied at 10, 20, 50, 100, 200, and 500 mM. Activities were plotted as 1/[glucose] vs. 1/activity (Lineweaver-Burke plot), and K_M and V_{max} were obtained from the negative x-intercept and reciprocal y-intercept, respectively. A total of 30 samples, ten from each of three separate sample preparations, were assayed for each construct at each glucose concentration.

2.6.5 Figure Data Analysis

GOx and GOx-PA activity data are the average and standard deviation of three independently prepared samples. DLS and zeta potential data are the average and standard deviation of ten sample runs from each of three independently prepared samples. Michaelis-Menten kinetic data are the average and standard deviation of ten measurements from three independently prepared samples.

2.7 References

1.   Guisan, J. M. (2006) *Immobilization of Enzymes and Cells*, Vol. 2, Humana Press.

2.   Gill, I., and Ballesteros, A. (2000) Bioencapsulation within Synthetic Polymers (Part 1): Sol–gel Encapsulated Biologicals, *Trends Biotechnol. 18*, 282.

3.   Berne, C., Betancor, L., Luckarift, H. R., and Spain, J. C. (2006) Application of a Microfluidic Reactor for Screening Cancer Prodrug Activation Using Silica-Immobilized Nitrobenzene Nitroreductase, *Biomacromolecules 7*, 2631.

4.   Betancor, L., Berne, C., Luckarift, H. R., and Spain, J. C. (2006) Coimmobilization of a Redox Enzyme and a Cofactor Regeneration System, *Chem. Commun. 42*, 3640.

5.   Ivnitski, D., Artyushkova, K., Rincón, R. A., Atanassov, P., Luckarift, H. R., and Johnson, G. R. (2008) Entrapment of Enzymes and Carbon Nanotubes in Biologically Synthesized Silica: Glucose Oxidase-Catalyzed Direct Electron Transfer, *Small 4*, 357.

6.   Lai, J. K., Chuang, T. H., Jan, J. S., and Wang, S. S. S. (2010) Efficient and Stable Enzyme Immobilization in a Block Copolypeptide Vesicle-templated Biomimetic Silica Support *Coll. Surf. B 80*, 51.

7.   Luckarift, H. R., Dickerson, M. B., Sandhage, K. H., and Spain, J. C. (2006) Rapid, Room-Temperature Synthesis of Antibacterial Bionanocomposites of Lysozyme with Amorphous Silica or Titania, *Small 2*, 640.

8.   Luckarift, H. R., Nadeau, L. J., and Spain, J. C. (2005) Continuous Synthesis of Aminophenols from Nitroaromatic Compounds by Combination of Metal and Biocatalyst, *Chem. Commun. 41*, 383.

9.   Luckarift, H. R., Spain, J. C., Naik, R. R., and Stone, M. O. (2004) Continuous Synthesis of Aminophenols from Nitroaromatic Compounds by Combination of Metal and Biocatalyst, *Nature Biotechnol. 22*, 211.

10.   Miller, S. A., Hong, E. D., and Wright, D. (2006) Rapid and Efficient Enzyme Encapsulation in a Dendrimer Silica Nanocomposite, *Macromol. Biosci. 6*, 839.

11.   Naik, R. R., Tomczak, M. M., Luckarift, H. R., Spain, J. C., and Stone, M. O. (2004) Entrapment of Enzymes and Nanoparticles Using Biomimetically Synthesized Silica, *Chem. Commun. 41*, 1684.

12.   Neville, F., Broderick, M. J. F., Gibson, T., and Millner, P. A. (2011) Fabrication and Activity of Silicate Nanoparticles and Nanosilicate-Entrapped Enzymes Using Polyethyleneimine As a Biomimetic Polymer, *Langmuir 27*, 279.

13.   Swartz, J. D., Deravi, L. F., and Wright, D. W. (2010) Bottom-Up Synthesis of Biologically Active Multilayer Films Using Inkjet-Printed Templates, *Adv. Funct. Mater. 20*, 1488.

14.   Zamora, P., Narváez, A., and Dománguez, E. (2009) Enzyme-modified Nanoparticles Using Biomimetically Synthesized Silica, *Bioelectrochemistry 76*, 100.

15.   Chien, L. J., and Lee, C. K. (2008) Biosilicification of Dual-fusion Enzyme Immobilized on Magnetic Nanoparticle, *Biotech. Bioeng. 100*, 223.

16. Marner, W. D., Shaikh, A. S., Muller, S. J., and Keasling, J. D. (2009) Enzyme Immobilization via Silaffin-Mediated Autoencapsulation in a Biosilica Support, *Biotechnol. Progr. 25*, 417.

17. Betancor, L., and Luckarift, H. R. (2008) Bioinspired Enzyme Encapsulation for Biocatalysis, *Trends Biotechnol. 26*, 566.

18. Ariga, K., Ji, Q., and Hill, J. P. (2010) Enzyme-Encapsulated Layer-by-Layer Assemblies: Current Status and Challenges Toward Ultimate Nanodevices, In *Adv. Polym. Sci.* (Caruso, F., Ed.), p 51, Springer-Verlag, Berlin, Germany.

19. Wilson, R., and Turner, A. P. F. (1992) Glucose Oxidase: an Ideal Enzyme, *Biosensors & Bioelec. 7*, 165.

20. Cao, H., Zhu, Y., Tang, L., and Li, C. (2008) A Glucose Biosensor Based on Immobilization of Glucose Oxidase into 3D Macroporous TiO2, *Electroanalysis 20*, 2223.

21. Minteer, S. D., Liaw, B. Y., and Cooney, M. J. (2007) Enzyme-based Biofuel Cells, *Curr. Op. in Biotech. 18*, 228.

22. Dror, Y., Kuhn, J., Avrahami, R., and Zussman, E. (2008) Encapsulation of Enzymes in Biodegradable Tubular Structures, *Macromolecules 41*, 4187.

23. Jiang, Y., Yang, D., Zhang, L., Sun, Q., Sun, X., Li, J., and Jiang, Z. (2009) Preparation of Protamine–Titania Microcapsules Through Synergy Between Layer-by-Layer Assembly and Biomimetic Mineralization, *Adv. Funct. Mater. 19*, 150.

24. Portaccio, M., Lepore, M., Ventura, B. D., Soilova, O., Manolova, N., Rashkov, I., and Mita, D. G. (2009) Fiber-optic Glucose Biosensor Based on Glucose Oxidase Immobilised in a Silica Gel Matrix, *J. Sol-Gel Sci. Technol. 50*, 437.

25. Jin, W., and Brennan, J. D. (2002) Properties and Applications of Proteins Encapsulated within Sol–gel Derived Materials, *Anal. Chim. Acta 461*.

26. Chen, Q., Kenausis, G. L., and Heller, A. (1998) Stability of Oxidases Immobilized in Silica Gels, *J. Am. Chem. Soc. 120*.

27. Przybyt, M., Miller, E., and Szreder, T. (2011) Thermostability of Glucose Oxidase in Silica Gel Obtained by Sol–gel Method and in Solution Studied by Fluorimetric Method, *J. Photochem. Photobiol. 103*, 22.

28. Aldrich, S. Product Information: Glucose Oxidase from Aspergillus niger.

29. Kröger, N., Dickerson, M. B., Ahmad, G., Cai, Y., Haluska, M. S., Sandhage, K. H., Poulsen, N., and Sheppard, V. C. (2006) Bioenabled Synthesis of Rutile (TiO2) at Ambient Temperature and Neutral pH, *Angew. Chem. Int. Ed. 45*, 7239.

30. Narahashi, Y. (1970) [47] Pronase, *Meth. Enzymol. 19*, 651.

31. Hermannson, G. T. (2008) *Bioconjugate Techniques*, Academic Press, Oxford.

32. Lewis, J. A., and Escalante-Semerena, J. C. (2006) The FAD-Dependent Tricarballylate Dehydrogenase (TcuA) Enzyme of Salmonella enterica Converts Tricarballylate into cis-Aconitate, *J. Bacteriol. 188*, 5479.

CHAPTER 3: Bio/inorganic Multifunctional Antimicrobial Nanocomposites

This chapter is distinct from, though represents a summary of the studies presented in the following publication:

Haase, N. R.; Eby, D. M.; Dickerson, M.; Cai, Y.; Sandhage, K. H.; Johnson, G. R.; Kröger, N. "Multifunctional Antimicrobial Coatings from Enzyme/Nanoparticle Nanocomposites," in preparation.

3.1 Abstract

This chapter details efforts towards utilizing the enzyme-functionalized coatings developed in Chapter 2 as antimicrobial materials. First, the synthesis of silver nanoparticles and construction of enzyme/nanoparticle composite Si-O coatings will be presented. Next, tests to assess the antimicrobial efficacy of these coatings against general infectious strains of *Escherichia coli* and *Staphylococcus aureus* will be presented. Then the experimental progression to form the most effective antimicrobial material will be explained, followed by an investigation into the chemical reasons for observed augmented antimicrobial action between the enzyme and nanoparticle agents. Finally, the general application of these coatings in a wound dressing material and the storage stability of these composites will be discussed.

3.2 Introduction

3.2.1 Antimicrobial Materials Introduction

As bacterial infections can be caused by a number of species, the utilization of general cytotoxic compounds which are effective against multiple types of bacterial infection is of interest. Silver ions (Ag^+), a well-known general antimicrobial agent,[1-4]

perform their bactericidal action by triggering proton leakage through the cell membrane, destroying the proton gradient which prevents production of ATP, thus robbing cells of vital energy.[5] Ag^+ has also been utilized as an antimicrobial agent by using silver nanoparticles (AgNPs) as a source of the cations for the prevention of bacterial growth.[6-9] This approach enables slowed release of Ag^+, resulting in sustained antimicrobial activity over longer time periods.[10]

Another commonly used antimicrobial agent is the reactive oxygen species hydrogen peroxide (H_2O_2). This agent is generally employed by direct application to an infection, but new methods are being developed which involve immobilization of Glucose oxidase.[11] As described in section 2.2.3, GOx uses glucose to catalyze the formation of H_2O_2, making it the generator of an antimicrobial agent. Vartiainen *et al.* immobilized GOx on polypropylene films and demonstrated their antimicrobial activity against *E. coli* and *B. subtilis* at a glucose concentration of 55.6 mM.[11] This demonstrated the ability to use H_2O_2 as an antimicrobial agent by a means other than direct application. However, it is not known if this will be effective at lower glucose concentrations, as H_2O_2 production may not be sufficient.

3.2.2 Synergistic Antimicrobial Activity

While the use of general antimicrobial agents is desired because of their bactericidal activity against a range of bacteria, these agents will not be as effective against a species resistant to them. Therefore, combining multiple antimicrobial agents with complimentary bactericidal effectiveness into a single deployable system broadens the spectrum of bacteria against which such a system could defend. Also, for bacteria susceptible to multiple agents in a composite, there exists the possibility that synergistic

antimicrobial activity could occur, wherein the bactericidal potency of the composite system is greater than the sum of the two agents. Eby and coworkers have shown evidence of this when they synthesized lysozyme-capped AgNPs, both of which display antimicrobial activity.[12] Silver-resistant strains of *P. mirabilis* tested against this enzyme/nanoparticle system were resistant to Ag^+ and lysozyme alone; however, when exposed to lysozyme-capped AgNPs bacteria growth was inhibited by AgNP concentrations below 10 μg mL^{-1}.[12] This indicated a concerted mechanism of antimicrobial action, wherein the presence of both agents resulted in antimicrobial activity. The authors hypothesized that this could be due to cellular membranes undergo when exposed to silver. Membrane proteins which can pump Ag^+ out of the cell will be expressed upon exposure to Ag/lysozyme composites, altering the membrane and possibly making it more susceptible to lysozyme.[12] Zan *et al.* demonstrated another form of synergistic antimicrobial activity by immobilizing Ag^+ and AgNPs into polyelectrolyte multilayers.[8] The fast release of immobilized Ag^+ imparted immediate antimicrobial activity to the films, while the slow release of Ag^+ from AgNPs yielded longer-term defense against bacteria, demonstrating a chronologically-based synergistic effect. This type of synergistic effect would be useful to clear an infection upon application of the material, and still allow defense against future infection. However, since the system is based upon the antimicrobial activity of Ag^+, silver-resistant bacteria will persist.

This chapter discusses the combination of GOx with AgNPs immobilized in/on LbL Si-O coatings to achieve synergistic antimicrobial activity. To my knowledge there is only one study utilizing this enzyme/nanoparticle composite for the antimicrobial purposes. Ben-Yoav, *et al.* encapsulated GOx in AgNP-doped polyglutaraldehyde and

demonstrated the system's ability to kill *E. coli* cells in biofilms in the absence of glucose.[13] The authors hypothesized that GOx was able to penetrate into the biofilms and scavenge glucose, producing H_2O_2 which reacted with AgNPs, releasing antibacterial Ag^+; this interaction has been evidenced by Guo, *et al.*[14] However, while cell death was observed, the antimicrobial activity decreased when 11 mM glucose was added to the system. This is an interesting result, as having more glucose available to produce more H_2O_2 should result in a more effective antimicrobial system. Also, no evidence of the hypothesized interaction between H_2O_2 and AgNPs was presented. This hypothesis is addressed in the research presented here. The proposed mechanism of synergistic antimicrobial activity is presented in the reactions below, where the production of hydrogen peroxide by GOx can both act as an antimicrobial agent and react with AgNPs to release cytotoxic Ag^+. While these reactions are known to occur separately, they have not been utilized together for synergistic antimicrobial activity.

$$Glucose + O_2 \xrightarrow{GOx} Glucolactone + H_2O_2 \qquad\qquad (3.1)^{15}$$
$$H_2O_2 + Ag_n \rightarrow HO\cdot + OH^- + Ag_n^+ \qquad\qquad (3.2)^{14}$$
$$Ag_n^+ \rightarrow Ag_{n-1} + Ag^+ \qquad\qquad (3.3)^{14}$$
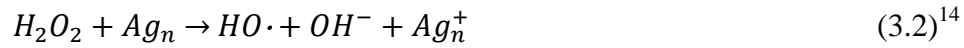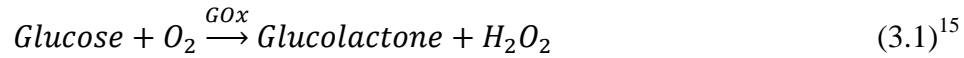
3.2.3 Antimicrobial Activity Testing

The antimicrobial activity tests utilized to ascertain the antimicrobial activity of composite coatings were detailed by Wiegand *et al.*[16] This is a broth dilution method in which antimicrobial agents are incubated with bacteria at dilutions ranging from 1:2 to 1:512, via serial dilutions. The broth dilution method tests first for the minimal concentration of an agent which inhibits cell growth (Minimum Inhibitory Concentration = MIC). Samples which show no cell growth are plated onto Agar plates to allow any

remaining bacteria to grow. The minimal agent concentration at which no bacteria grow on plates is identified as the Minimum Bactericidal Concentration (MBC). Enzyme/nanoparticle composites were also electrospun into regenerated silk fibroins to investigate whether or not these coatings would be functional in a textile. The antimicrobial activity of textile fabrics is tested using industry-established methods to assess the efficacy of diffusible antimicrobial materials.[17,18] In these tests fabrics are placed on agar plates on which bacteria have been spread, and as antimicrobial agents diffuse outward they kill the surrounding bacteria. The region of lethal activity is called the clearing zone. A larger clearing zone indicates higher potency of the agents.

3.2.4 Glucose/H_2O_2, Ag^+, and ATP Testing

As mentioned previously, the antimicrobial activity of GOx/AgNP composites is based on the reaction of H_2O_2 and AgNPs to release Ag^+.[13,14] To observe any interaction of these two antimicrobial agents, assays for glucose and H_2O_2 determinations were performed in parallel and compared with quantification of Ag^+ release. To determine H_2O_2 concentration the GOx-based assay discussed in Chapter 2 was used. The glucose quantification is based on a coupled enzyme assay, in which the production of NADH is used as a measure for glucose consumption. In the first step of this assay hexokinase catalyzes the phosphorylation of glucose to glucose-6-phosphate (G6P) with ATP as a substrate. G6P Dehydrogenase then catalyzes the oxidation of G6P with NAD+ to yield 6-phosphogluconate and NADH; the absorption of the latter at 340 nm is recorded. This assay is not based on detection of H_2O_2 and therefore will not interfere with its determination. Performing these experiments on enzyme/nanoparticle composites will indicate if AgNPs interact with H_2O_2. Elemental analysis of Ag^+ release from AgNPs in

the presence and absence of GOx-PA will show if the interaction of H_2O_2 stimulates the release of silver cations.

To investigate the immediate influence of each antimicrobial agent on the antimicrobial activity of composites within the first few hours of bacteria exposure, ATP production by bacterial cultures was monitored. This is a general measurement of the growth of cultures and their metabolic activity. In this assay cells are lysed and ATP reacts with a substrate to produce a luminescent product, and the total luminescence is measured. Comparing the ATP production of composites and single-agent controls will provide insight into the contribution of H_2O_2 and Ag^+ to the antimicrobial activity of the composite. This experiment will be combined with MIC determination to correlate any short-term suppression of ATP production with overall antimicrobial activity.

3.3 Preparation of Enzyme/Nanoparticle Composites

This section will detail the characterization of water-stable silver nanoparticles (AgNPs) with one of two capping agents, citrate and tiopronin. These capping agents were selected because they impart a negative zeta potential on the AgNPs, owing to their carboxylate groups which are distal to the AgNP when bound, and because citrate and tiopronin bind to AgNPs via hydroxyl and thiol linkages, respectively, allowing for observation of any effect of the capping agent on AgNP antimicrobial activity.

3.3.1 Characterization of Silver Nanoparticles

Previously-developed methods were adapted to prepare water-stable AgNPs capped with either tiopronin[19] or citrate,[20] denoted as t-AgNPs and c-AgNPs, respectively; these are shown in **Figure 3.1**. DLS and zeta potential measurements were

performed to obtain size and surface charge information of the AgNPs. The c-AgNPs aggregated in Tris-HCl buffer, so all measurements were performed in sodium phosphate-buffered solutions at pH 7. This revealed t-AgNPs to possess a zeta potential of $\zeta = -19.7 \pm 2.27$ mV, while that of c-AgNPs was $\zeta = -38.7 \pm 1.76$ mV, indicating both
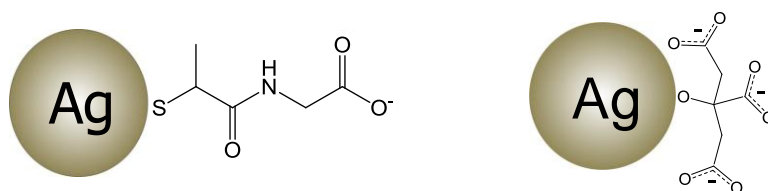
Figure 3.1: Water-stable AgNPs capped with tiopronin (left) and citrate (right). Note, structures are not drawn to scale.

should electrostatically adsorb to positively-charged surfaces. DLS measurements showed t-AgNPs consisted of two separate populations, primarily ranging from $2 - 10$ nm in diameter with an average of 5.93 nm, and a smaller population from ~$15 - 30$ nm in diameter with an average of 21.1 nm. DLS analysis of c-AgNPs revealed polydispersity as well, with most AgNPs ranging from $7 - 35$ nm in diameter with an average of 21.33 nm, and a small population of $2.3 - 3.7$ nm diameter with an average of 3.00 nm. These results were confirmed with transmission electron microscopy (TEM) measurements of the AgNPs, showing t-AgNPs to have a prevalence of <10 nm particles and c-AgNPs with a prevalence of >10 nm particles (**Figure 3.2**).
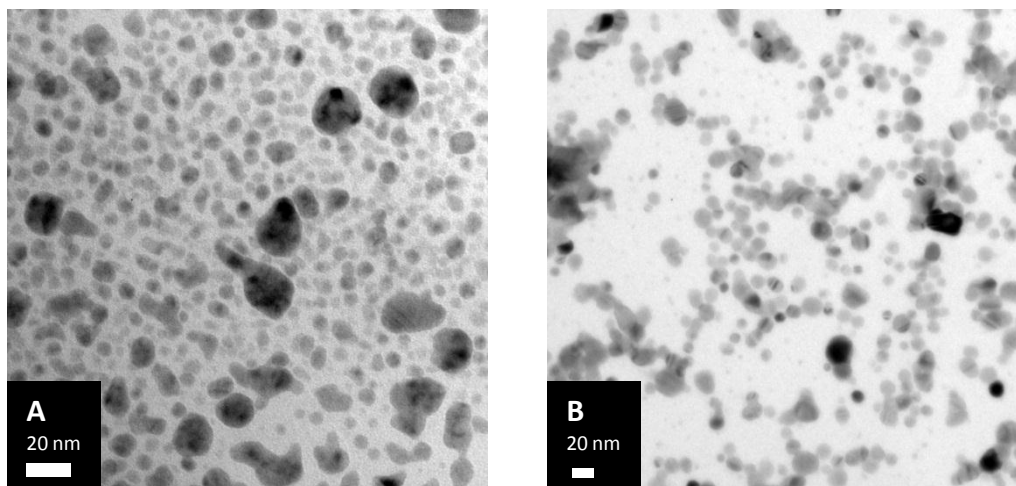
Figure 3.2: Transmission electron micrographs of t-AgNPs (A) and c-AgNPs (B). Images taken by Dr. Ye Cai.

3.3.2 Construction of Composites

AgNPs were immobilized on silica spheres coated with Si-O using the method detailed in Chapter 1.[21] The outer surface of the Si-O layers was coated with protamine to render it positively charged, allowing the AgNPs to electrostatically adsorb to the protamine-coated surface. TEM observations showed this to be successful (**Figure 3.3**).
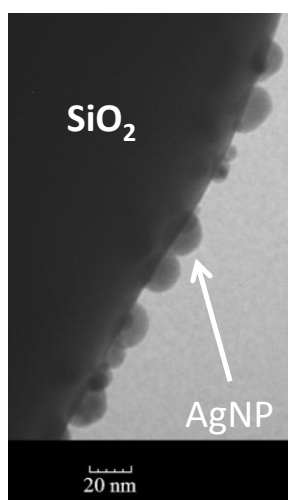
Figure 3.3: Transmission electron micrograph of t-AgNPs immobilized on protamine-coated 1 μm diameter silica sphere. This image taken by Dr. Samuel Shian.

To prepare enzyme/nanoparticle composites, three protamine-induced Si-O coatings were deposited onto 150 nm diameter silica spheres. During adsorption of the second layer of protamine a saturating amount of GOx-PA was immobilized as described in Chapter 2;[21] AgNPs were immobilized to the outer surface of protamine-coated LbL particles. A general schematic of these composites is shown in **Figure 3.4**. The concentration of composite used in antimicrobial activity testing was always reported as the µg mL^{-1} of silica spheres, as that was the constant material in all samples tested. Composites containing GOx-PA and tiopronin-capped AgNPs were labeled *GT* while those with citrate-capped AgNPs were labeled *GC*.
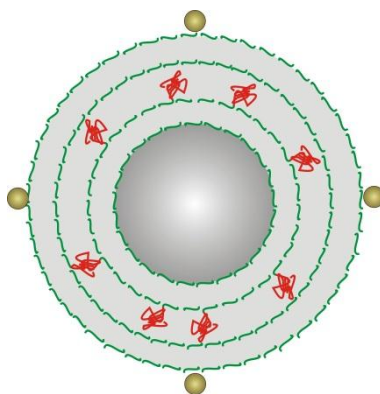
Figure 3.4: General layout of antimicrobial composites. In this layout GOx-PA (shown in red) is immobilized during adsorption of the second layer of protamine. Two more layers of Si-O are then deposited, protamine is adsorbed, and lastly AgNPs (shown in bronze) are adsorbed.

3.4 Results & Discussion

3.4.1 MIC/MBC Testing

Initial antimicrobial efficacy tests were performed to ascertain the concentration of glucose needed to inhibit cell growth and kill all bacteria present (Minimum Inhibitory

and Bactericidal Concentrations, MIC and MBC, respectively). These tests were conducted on GOx-PA-only coatings at glucose concentrations of 90, 50, 10, 5, and 1 mM (**Table 3.1**). At a glucose concentration of 10 mM GOx-PA exerted antimicrobial activity over both *E. coli* and *S. aureus*; below this concentration no activity against *E. coli* was seen. From this result, 10 mM was the concentration used for future experiments.

Table 3.1: Antimicrobial activity of immobilized GOx-PA at varying glucose concentrations. The MIC and MBC of GOx-PA immobilized in Si-O coatings on 150 nm diameter silica spheres is reported as range in µg mL^{-1} of silica spheres. The data are the average and standard deviation of triplicate measurements. "N.A." – No Activity.

E. coli – 1.2 x 10^6 ± 0.56 cfu		
Glucose Concentration (mM)	**MIC (µg mL^{-1})**	**MBC (µg mL^{-1})**
90	62.5 – 125	62.5 – 500
50	62.5	125
10	62.5 – 250	250
5	N.A.	N.A.
1	N.A.	N.A.
S. aureus – 2.5 x 10^5 ± 0.71 cfu		
90	2.0	2.0
50	3.9	3.9
10	3.9 – 7.8	7.8
5	31.2 – 62.5	31.2 – 62.5
1	31.2 – 62.5	31.2 – 62.5

In testing GOx-PA/AgNP composites, it is generally thought that thiol compounds act as a neutralizing agent to silver's antimicrobial activity.[22] Therefore, simultaneous testing of t-AgNPs and c-AgNPs was performed to determine any effect of tiopronin on the antimicrobial activity of AgNPs. Neither t-AgNPs nor c-AgNPs exhibited antimicrobial activity alone, and t-AgNPs were more effective than c-AgNPs

when used with GOx-PA, resulting in MIC and MBC values against *E. coli* 25% that of GOx-PA alone (**Table 3.2**). Therefore, tiopronin did not inhibit the antimicrobial activity of the system, and since neither capping agent exhibited antimicrobial activity at the concentrations used to synthesize AgNPs (**Tables A.1 and A.2**), the AgNPs must be responsible for the observed effect. While the composite showed greater potency against *S. aureus* versus *E. coli*, no synergistic effect was seen by *GT*, which is in agreement with the study by Jung *et al.*, which showed *E. coli* to be more susceptible to Ag^{+} than *S. aureus*.[7]

Table 3.2: Comparison of AgNP capping agents on antimicrobial activity. The MIC and MBC range of GOx-PA/AgNP composites are reported in µg mL^{-1} of silica spheres tested in 10 mM glucose. The results are the average and standard deviation of triplicate measurements. Sample definitions – *G*, GOx-PA; *GT*, GOx-PA/t-AgNP; *T*, t-AgNP; *GC*, GOx-PA/c-AgNP, *C*, c-AgNP. "N.A." – No Activity.

E. coli – 7.3 x 10^5 ± 0.47 cfu		
Antimicrobial Construct	**MIC (µg mL^{-1})**	**MBC (µg mL^{-1})**
G	250 – 500	≥500
GT	60 – 62.5	60 – 62.5
T	N.A.	N.A.
GC	250 – 500	>500
C	N.A.	N.A.
S. aureus – 3.6 x 10^5 ± 0.37 cfu		
G	3.9	3.9 – 7.8
GT	2.0 – 3.9	3.9
T	N.A.	N.A.
GC	3.9	3.9 – 7.8
C	N.A.	N.A.

The presence and absence of synergistic activity when t-AgNPs and c-AgNPs were used, respectively, with GOx-PA, could be due to the difference in size of the two

AgNPs. Ivanova, *et al*., studied the electrochemical oxidation of c-AgNPs and found that as the nanoparticle diameter decreased their oxidation to Ag^+ occurred at lower driving potentials.[23] The t-AgNPs are smaller than c-AgNPs by a factor of 3.6, and thus may exhibit greater susceptibility to H_2O_2 oxidation than c-AgNPs. This could also be due to differences in the surface area/volume ratio of the two AgNPs. The smaller AgNPs will have more of their Ag atoms on the surface; and thus more accessible for H_2O_2.

3.4.2 Tuning GOx-PA/t-AgNP Composite Antimicrobial Activity

After analyzing the MIC/MBC results of antimicrobial composites, efforts were made to increase the effectiveness of the highest-performing composite, GOx-PA and t-AgNPs in Si-O coatings. Two approaches were taken towards this end: tuning the GOx-PA:AgNP ratio to identify the ratio with the most potent synergistic activity, and increasing the loading of each antimicrobial agent in the coatings. These tests were performed against *E. coli* only, since MIC/MBC test results showed no difference between composites and enzyme-only controls against *S. aureus* (**Table 3.2**).

Towards tuning the enzyme/nanoparticle ratio, GOx-PA and t-AgNPs were placed on separate coated spheres so they could be easily mixed in different amounts. When the loading of GOx-PA was cut in half an increase in MIC/MBC was observed, indicating that H_2O_2 is critical to the antimicrobial efficacy of the composite. A decrease in t-AgNP loading only showed an attenuation of antimicrobial efficacy when the t-AgNP loading was decreased to $^1/_{32}$ of the original amount (**Table A.3**). These experiments indicated H_2O_2 to have the most pronounced antimicrobial activity. From an application perspective, since the AgNPs are employed to act in a stoichiometric fashion by releasing

Ag$^+$, it is beneficial to have as many nanoparticles present as possible to yield longer-term antimicrobial activity.

To attempt to increase the overall efficacy of the composites, the loading of one agent was held constant while the other was increased (composite coatings on silica spheres were prepared for these tests). To increase the amount of immobilized GOx-PA, a five-layer system was prepared wherein saturating amounts of GOx-PA (200 µg) were immobilized in layers two, three, and four; t-AgNPs were immobilized on the outer surface of the fifth layer. This resulted in a composite with three times the amount of GOx-PA used before, but the same amount of AgNPs (termed *3G-1T*). To increase the amount of AgNPs on the coatings the amount of GOx-PA was held constant and t-AgNP immobilization steps were performed multiple times on the outer surface of the three-layer composite. One sample was made with twice the amount of t-AgNPs (*1G-2T*). After five immobilization steps the t-AgNPs were seen in the immobilization supernatant, indicating saturation point of t-AgNP adsorption; this sample was termed *1G-5T*. These are shown in **Figure 3.5**.

3G-1T   *1G-2T*   *1G-5T*
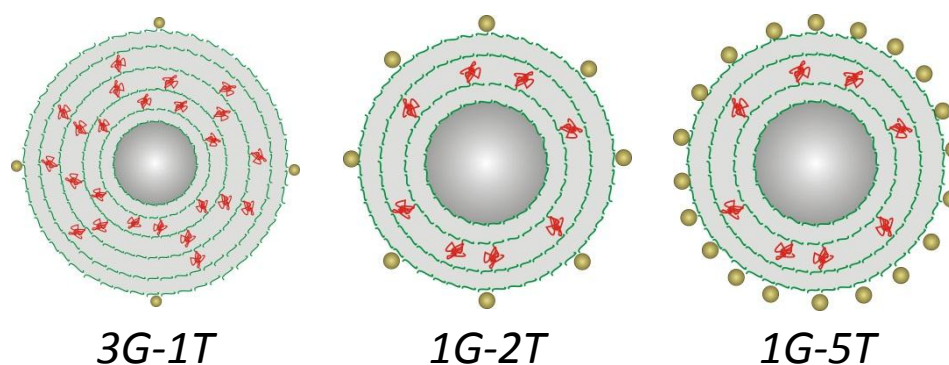
Figure 3.5: GOx-PA/AgNP composites with adjusted enzyme and nanoparticle loadings. The controls *3G* and *5T* are similar to the graphics on the left and right, respectively, without the other agent present. Note, the graphics are not equal in scale.

The results of MIC/MBC testing showed no greater potency for *1G-2T*, and the MIC/MBC increased when AgNPs saturated the coatings (*1G-5T* versus *GT*, **Table 3.3**). This indicated that having too many t-AgNPs immobilized may hinder the antimicrobial activity of H_2O_2. This could to be due to the additional AgNPs reacting with more H_2O_2 which, even if releasing more Ag^+, does not compensate for the loss of H_2O_2. to the overall antimicrobial activity of the composite. It could also be due to AgNPs clogging the pores of the Si-O coatings, limiting glucose and H_2O_2 diffusion through the material. Finally, increasing GOx-PA loading in composites did not result in greater potency, thus GOx-PA loading was kept at its initial level.

Table 3.3: MIC/MBC testing with altered antimicrobial agent concentrations. The values are reported in μg mL^{-1} of silica spheres tested in 10 mM glucose. The sample definitions are the same as those in Table 3.2, while the numbers beside *G* and *T* denote the amount of additional enzyme or nanoparticle, respectively, expressed as a multiple of the original loading. The results are the average and standard deviation of triplicate measurements. "N.A." – No Activity.

	E. coli – 5 x 10^5 cfu	
Sample	**MIC (μg mL^{-1})**	**MBC (μg mL^{-1})**
GT	31.3 – 62.5	31.3 – 62.5
3G-1T	31.3 – 62.5	31.3 – 62.5
1G-2T	31.3 – 62.5	31.3 – 62.5
1G-5T	≥250	≥250
G	125 – 250	125 – 250
3G	31.3 – 62.5	31.3 – 62.5
5T	N.A.	N.A.

3.4.3 Investigation of the Mechanism of Antimicrobial Activity

3.4.3.1 Interaction of H_2O_2 and Ag^+ in Composites

The antimicrobial activity of GOx-PA/t-AgNP composites presented in **Table 3.2** revealed that the presence of H_2O_2 and AgNPs resulted in synergistic antimicrobial activity, decreasing the MIC/MBC below either agent alone (GOx-PA or t-AgNPs). To identify reaction of t-AgNPs and H_2O_2 three complimentary experiments were performed. These experiments were: i) a H_2O_2 quantification assay of the composite performed in concert with ii) quantification of the residual glucose concentration from this assay, and iii) elemental analysis of Ag^+ released by the composite. Experiments to quantify Ag^+ release were performed in M-H medium, while glucose/H_2O_2 experiments were performed in buffer since no H_2O_2 was detected when this was attempted in the medium. This was likely due to H_2O_2 oxidizing the nutrients in the medium. Performing H_2O_2 and Ag^+ quantification assays in concert with a glucose determination assay, which measures the concentration of glucose left after the assay, would indicate if a decrease in detected H_2O_2 was caused by the inhibition of the enzymatic reaction or the reaction of H_2O_2 and t-AgNPs. This showed the glucose concentration in the presence of *GT* after the enzyme activity assay was identical to the GOx-PA-only control, while the concentration of H_2O_2 measured was 26.7% lower (**Table 3.4**). This indicated that t-AgNPs are reacting with H_2O_2 and not inhibiting GOx-PA. The quantification of Ag^+ released by the interaction of t-AgNPs with H_2O_2 in conditions mimicking MIC/MBC testing indicated that after 2 h *GT* has released over 13-times more Ag^+ than immobilized t-AgNPs alone (**Table 3.5**). As these experiments were performed in MH medium, the subsequent decrease in Ag^+ concentration with time could be due to the Ag^+ interacting

with nutrients and salts in the medium and becoming reduced or precipitated as AgCl. It

is also possible that reaction of AgNPs with H_2O_2 oxidizes the AgNP surface, passivating

it against further reaction.

Table 3.4: Glucose and hydrogen peroxide concentrations of GOx-PA/t-AgNP incubation in glucose. GOx activity and glucose determination assays were performed to quantify the H_2O_2 and glucose concentrations. The results are the average and standard deviation of triplicate measurements.

Sample	[glucose] (mM)	[H_2O_2] (mM)
G	1.090 ± 0.007	3.00 ± 0.31
GT	1.082 ± 0.003	2.20 ± 0.12

Table 3.5: Release of Ag$^+$ by *GT*. GOx-PA/t-AgNP and t-AgNP functionalized Si-O coatings were incubated in MH medium supplemented with 10 mM glucose at 37 °C and the concentration of Ag$^+$ was determined via ICP-OES. The results are the average and standard deviation of triplicate measurements.

Time (h)	*GT* [Ag$^+$] (ppb)	*T* [Ag$^+$] (ppb)
2	5.50 ± 2.14	0.40 ± 0.22
4	4.60 ± 1.61	0.20 ± 0.10
6	2.30 ± 1.66	0.10 ± 0.04
16	0.90 ± 0.62	0.10 ± 0.01

Taken together, the GOx activity and glucose determination assays, along with

Ag$^+$ elemental analysis, show the GOx-PA/t-AgNP composite consumes glucose at an

equal rate as the enzyme-only control. Furthermore, t-AgNPs react with H_2O_2,

accelerating the release of Ag$^+$. Therefore, it can be concluded GOx-PA and t-AgNPs do

act in a synergistic manner, and the addition of Ag$^+$ to an environment containing H_2O_2 is

the likely cause for the increase in potency of enzyme/nanoparticle versus either agent

alone.

After characterizing the reaction of H_2O_2 and t-AgNPs, a more descriptive picture of the composite antimicrobial action *in situ* was sought. To this end, the ATP production in *E. coli* cultures was monitored during incubation with *GT* coatings, as well as GOx-PA, t-AgNP, and no-agent controls. Identical silica sphere concentrations were used and the ATP production was monitored periodically. These experiments showed that presence of H_2O_2 to suppress ATP production, and the presence of Ag^+ yielded a 120 min delay in the increase of ATP production (**Figure 3.6**). However, samples were left overnight to serve as MIC tests, and 62% of cultures incubated with just GOx-PA grew, while all cultures incubated with *GT* were dead in the morning.
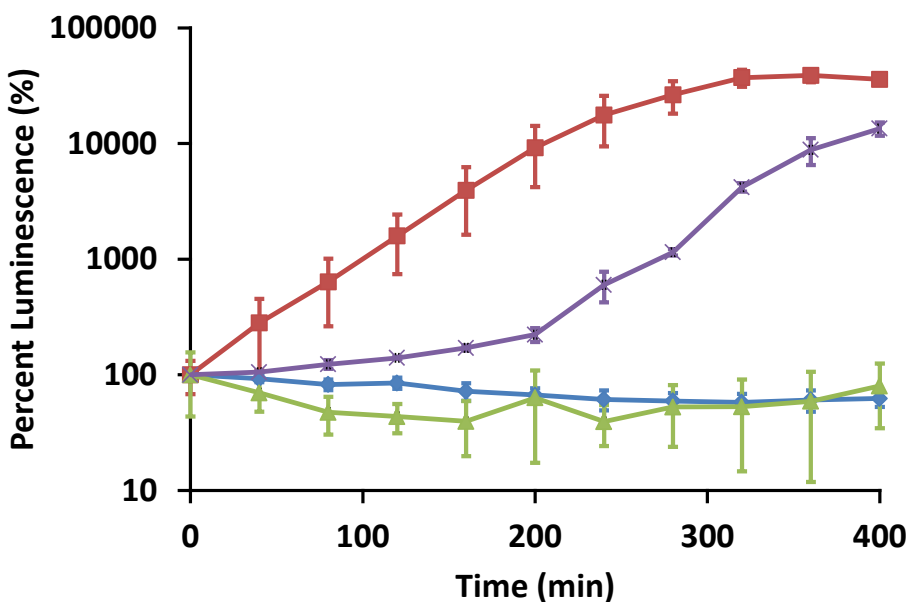
Figure 3.6: Luminescence showing ATP production for *E. coli* cultures. 120 μg mL^{-1} of *GT* (♦), immobilized t-AgNPs (✗) and GOx-PA (▲), and *E. coli*-only controls (■). A starting cell concentration of 3.9 x 10^5 ± 3.4 cells mL^{-1} was used. Luminescence data were normalized to 100% at the start of the assay and plotted logarithmically. Note: the instrument sensitivity was higher for GOx-PA and *GT*. The results are the average and standard deviation of eight independent measurements.

3.4.4 Storage Stability of Composite Coatings

The degradation of antimicrobial activity over time in storage conditions reflective of this application was studied by storing *GT* at -20 °C and periodically removing samples for MIC/MBC testing. The results, shown in **Table 3.6**, showed a two-fold increase in MIC/MBC against *E. coli* after one month of storage ($\geq$60 µg mL^{-1} to $\leq$120 µg mL^{-1}) and three-fold increase after three months ($\geq$60 µg mL^{-1} to $\leq$200 µg mL^{-1}).

Table 3.6: Stability of *GT* during long-term storage at -20 °C. Samples were suspended in 50 mM NaAc pH 5.1 and placed at -20 °C, stored for one to three months, then subjected to MIC/MBC testing. The results are the average and standard deviation of triplicate measurements.

E. coli – 1.65 x 10^5 cfu		
Storage time	**MIC (µg mL^{-1})**	**MBC (µg mL^{-1})**
0 months	60 – 62.5	60 – 62.5
1 month	100 – 120	100 – 120
3 months	180 – 200	180 – 200

3.4.5 Textile Deployment of Antimicrobial Composite Coatings

To test the effectiveness of the enzyme/nanoparticle composite coatings in an application setting, 150 nm diameter silica spheres were electrospun into silk fibroins to simulate a wound dressing (**Figure 3.7**). These fibroins were then subjected to clearing zone tests, wherein bacteria were spread onto MH-Agar plates that had been supplemented with 10 mM glucose, and then a 2 cm *x* 2 cm square or 1 cm diameter circular patch of fibroin was placed over the bacteria. The performance of these fibroins was evaluated by measuring the distance between the edge of the patch and that of the
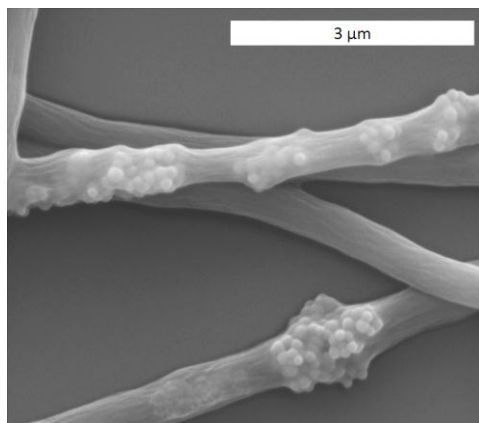
Figure 3.7: SEM of *GT* immobilized in regenerated silk fibroin. Image taken by Dr. Matthew Dickerson.

surrounding bacteria. This space, in which all bacteria are killed, is termed the "clearing zone" and is larger for more potent samples. A sample picture of this is given in **Figure 3.8** (All pictures can be found in **Figures A.1 and A.2**). Quantified clearing zone results are presented in **Table 3.7** and show that controls, which contained coated silica spheres absent GOx-PA and t-AgNPs, exerted no antimicrobial activity against both *E. coli* and *S. aureus*. *GT* displayed millimeter-level clearing zone against both bacteria, with a larger clearing zone against *S. aureus*. That *GT* exhibited antimicrobial activity in silk fibroins is a basic demonstration that these composites can be deployed over large areas, not just on the nanometer scale.
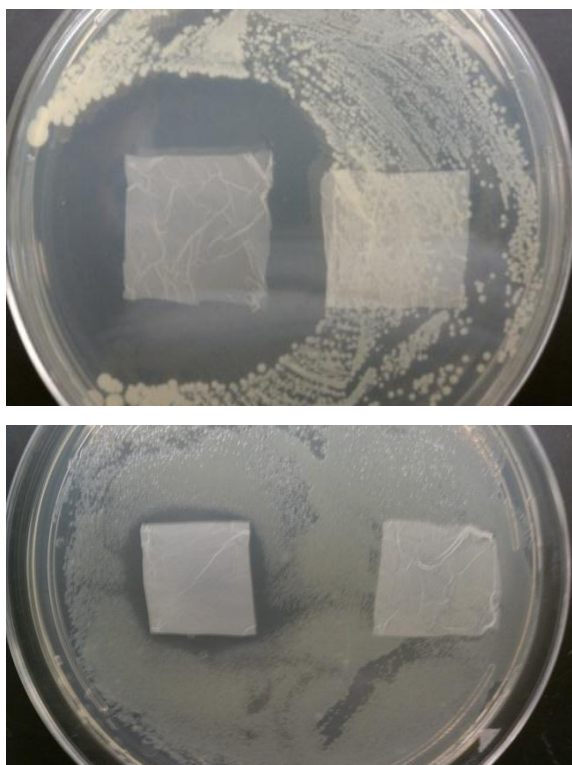
Figure 3.8: Typical elecrospun silk fibroin clearing zone test of electrospun *GT* on plates containing *S. aureus* (top) and *E. coli* (bottom). Within each plate, silk fibroin containing *GT* is on the left and the control (containing silica spheres) is on the right.

Table 3.7: Clearing zone test of electrospun silk fibroin fibers containing *GT*. Note: fibroins containing no composite exerted no antimicrobial activity. The results are the average and standard deviation of triplicate measurements.

$E.\ coli - 1.1 \times 10^6 \pm 0.56$ cfu	
Silk fibroin	**Clearing zone (mm)**
Disk	1.05 ± 0.70
Square	1.18 ± 0.68
$S.\ aureus - 4.5 \times 10^5 \pm 0.38$ cfu	
Disk	16.19 ± 1.30
Square	15.21 ± 2.26

3.5 Conclusions

3.5.1 Summary of Antimicrobial System Development

This chapter detailed the synthesis of water-stable AgNPs, the construction and antimicrobial testing of enzyme/nanoparticle composite antimicrobial coatings, an investigation into the mechanism of antimicrobial activity, and the deployment of these coatings in a textile. These composites consisted of a modified form of the enzyme Glucose oxidase which produces the cytotoxic agent hydrogen peroxide, and silver nanoparticles that release antimicrobial silver cations upon reaction with peroxide. These composites showed a four-fold decrease in the minimum inhibitory and bactericidal concentrations versus enzyme-only samples at physiological glucose concentration, while the silver nanoparticles showed no antimicrobial activity when used alone. This indicated that the composite acts in a synergistic fashion, with H_2O_2 triggering the release of Ag^+. When the capping agent of the silver nanoparticles was switched from tiopronin to citrate the synergistic activity was lost, showing that the capping agent used to construct silver nanoparticles is important.

Experiments into the interaction of hydrogen peroxide and silver nanoparticles revealed, qualitatively, a loss of peroxide in the presence of silver nanoparticles coupled with an increase in silver ion concentration. This investigation indicates H_2O_2 does react with t-AgNPs, resulting in the release of silver cations at a ratio of 11.4 μmol Ag^+ released for every mole of H_2O_2 consumed. However, as the concentration of Ag^+ changes with time (likely due to precipitation), the ratio of H_2O_2 consumed by AgNPs and Ag^+ released cannot be reliably quantified. I believe this concerted action is the cause for enhanced antimicrobial activity of enzyme/nanoparticle composites over single-

agent controls. When the concentration used was below the MIC/MBC value, a recovery in ATP luminescence was observed after all glucose had been consumed by the composite. This underscores hydrogen peroxide as being the chief antimicrobial agent in this system.

When the enzyme/nanoparticle composite-coated spheres were immobilized into electrospun silk fibroins, the antimicrobial activity of the system was retained, as these samples were able to kill bacteria in the vicinity of the fibroin. Their function in regenerated silk fibroin is a proof-of-concept for application of these coatings as wound dressings to prevent bacterial infection at physiological glucose concentration.

3.5.2 Outlook of Antimicrobial System Development and Application

To further develop the current antimicrobial coatings, they should be tested in an environment more reflective of that a wound dressing would encounter. The basic viability of this antimicrobial solution has been shown, but in development it would need to be tested in the presence of human cells to investigate two aspects. First, their toxicity towards human cells is necessary information to ensure this composite is safe for deployment. Second, it must be investigated if these coatings are susceptible to cellular and tissue defenses, as they would be then unusable in their current form. Furthermore, these coatings were deposited onto silica spheres since they were easy to use in the MIC/MBC testing setup employed in this research.

Developing the construction of these antimicrobial coatings on foundations more appropriate for wound dressings and fluid decontamination applications is of significant importance. For fluid decontamination, performing LbL composite construction on porous foundations would allow fluid to pass through the construct and bring bacteria in

close proximity to the immobilized antimicrobial agents. For deployment in a textile, because silk fibroins are negatively charged, they should be a suitable foundation on which to perform LbL buildup and the construction of enzyme/nanoparticle composite coatings. Lastly, the layer-by-layer method of immobilizing antimicrobial agents allows for the addition of other agents, such as protease and chitinase enzymes. The addition of other antimicrobial agents would expand the general antimicrobial capability of these systems.

3.6 Materials & Methods

3.6.1 Chemicals

Silica spheres (150 nm diameter) were purchased from Bangs Laboratories (Fishers, IN, USA). Tiopronin, sodium borohydride, Glucose oxidase (from *Aspergillus niger*), horseradish peroxidase (from *Amoracia rusticana*), protamine sulfate (from salmon), D-glucose, and tetramethoxisilane (TMOS) were purchased from Sigma-Aldrich (St. Louis, MO, USA). *o*-Dianisidine dihydrochloride, Mueller-Hinton broth nutrient, tri-sodium citrate, silver nitrate, and sodium acetate (NaAc) were purchased from VWR (Radnor, PA, USA). Bis(sulfosuccinimidyl) suberate (BS3) was purchased from Thermo Scientific (Rockford, IL, USA). MilliQ purified water (resistivity: 18.2 MΩ cm) was used for all solutions and washing steps.

3.6.2 Water-Stable Silver Nanoparticles

3.6.2.1 Synthesis of tiopronin-capped Silver Nanoparticles

Tiopronin-capped AgNPs (t-AgNPs) were synthesized using a modification of the method established by Huang et. al.[19] First, the following solutions were prepared − 0.12

M AgNO$_3$, 0.88 M tiopronin, 1.06 M NaBH$_4$ (fresh). After preparation all solutions were cooled in an ice water bath for 1 hour. Next, 20 mL of tiopronin were added to 50 mL AgNO$_3$ and mixed in an ice water bath under vigorous stirring for 2 hours. Then 15 mL NaBH$_4$ was added to the AgNO$_3$/tiopronin mixture evenly over the course of 5 minutes. The mixture was then stirred for 30 minutes in an ice water bath. To stop the reaction concentrated HCl was added until the solution was acidic; then it was neutralized with 2 M NaOH.

To purify the t-AgNPs the synthesis solution was placed into 50 mL conical tubes and centrifuged for 30 minutes at 4,000 x *g*. The supernatant was then decanted into 85 mL tubes and centrifuged for 1 hour at 16,500 x *g*. These supernatants were then poured into a gas pressure filter assembly fitted with a 3 kDa nitrocellulose membrane (Millipore Corp., Billerica, MA). Under an N$_2$ gas stream with a pressure of 70 PSI and during slow stirring, the nanoparticles were concentrated to a volume of 10 mL. Then 190 mL water was added, the volume was again decreased to 10 mL, and the washing process was repeated for a total of five washes with water. The nanoparticles were finally concentrated to 10 mL and stored in a foil-wrapped 15 mL conical tube at 4 °C.

3.6.2.2 Synthesis of Citrate-capped Silver Nanoparticles

Citrate-capped AgNPs (c-AgNPs) were synthesized using a modified method established by Kobayashi et al.[20] First, the following solutions were prepared – 0.1 M AgNO$_3$, 3 mM tri-sodium citrate, and 10 mM NaBH$_4$ (fresh). The solutions were then placed in an ice-water bath for 1 h. Next, 9.9 mL of tri-sodium citrate was added to 79.2 mL water and 9.9 mL NaBH$_4$ was added to the diluted tri-sodium citrate during vigorous stirring. This mixture was cooled for 1 hr in an ice-water bath, and 1 mL of AgNO$_3$ was

added to the mixture during stirring. The final reaction mixture was stirred for 30 min in an ice-water bath and then allowed to warm to room temperature.

To wash and purify the c-AgNPs the synthesis solution was first centrifuged for 1 hr at 16,500 x *g* in 85 mL tubes. The supernatants were then poured into a gas pressure filter assembly fitted with a 3 kDa nitrocellulose membrane. Under an N_2 gas stream with a pressure of 70 PSI and slow stirring the nanoparticles were concentrated to a volume of 20 mL. Then 180 mL water was added, the volume was again decreased to 20 mL, and this washing process was repeated for a total of five washes with water. The nanoparticles were finally concentrated to a volume of 20 mL and stored in a foil-wrapped 50 mL conical tube at 4 °C.

3.6.2.3 DLS and Zeta Potential Characterization of Silver Nanoparticles

All AgNPs were subjected to size determination by DLS and TEM, as well as surface charge characterization by zeta potential measurement. For zeta potential characterization AgNPs in 50 mM phosphate/citrate pH 7 were subjected to measurements in a Malvern Instruments Zetasizer Nano ZS (Malvern Instruments, Worcestershire, United Kingdom). Data were averaged over 10 measurement runs, and data evaluation was performed using the Smoluchowski Approximation, silver material settings, and Multiple Narrow Mode Analysis (Malvern Zetasizer Software v6.20). Samples were prepared in three independent experiments and the results were averaged.

For DLS characterization measurements were performed in 50 mM phosphate/citrate pH 7 in a Malvern Instruments Zetasizer Nano ZS (Malvern Instruments, Worcestershire, United Kingdom). Data were recorded using the 173° Backscatter measurement angle and analyzed using the silver material specification and

General Mode Analysis in the Malvern Zetasizer Software (v6.20). Samples were prepared in three independent experiments, each averaged across ten consecutive data runs, and the results of the three measurements were averaged.

3.6.2.4 Transmission Electron Microscopy of Silver Nanoparticles

TEM observation was performed by placing a droplet of each AgNP suspension onto wax paper, placing a TEM grid (Holey carbon film on 300 mesh copper grid, Electron Microscopy Sciences, Hatfield, PA, USA) on top of the droplet, and wicking the liquid through the grid with a tissue. Observations were made on a JEOL 4000 EX (Tokyo, Japan) operating at 400 KV.

3.6.3 Construction of Enzyme/Nanoparticle Composite Coatings

Functionalized Si-O coatings were prepared according to the method developed by Haase *et al.*[21] Briefly, silica spheres were exposed to alternating solutions of protamine and silicic acid in pH-buffered solutions to adsorb protamine and deposit Si-O on the surface to build up three Si-O layers. During adsorption of the second protamine coating GOx-PA (prepared according to Haase *et al.*[21]) was immobilized in a saturating amount. After the third Si-O coating was deposited an additional protamine layer was adsorbed and AgNPs were adsorbed to this surface in 50 mM phosphate-citrate pH 7.

3.6.4 Antimicrobial Agent Testing

3.6.4.1 MIC/MBC Testing

Antimicrobial tests to determine the amount of material needed to inhibit bacteria growth (minimum inhibitory concentration, MIC) and kill all bacteria (minimum bactericidal concentration, MBC) were performed using the broth microdilution method established by Wiegand *et. al.*[16] All tests were performed against BSL-2 strains of *E. coli*

and *S. aureus*, AATCC 25922 and 25923, respectively. The modified procedure utilized for clearing zone tests with silk fabrics was established by the American Association of Textile Chemists and Colorists (AATCC);[17,18] these methods are summarized below. All tests were performed in a BSL-2 laboratory at Tyndall Air Force Base, FL.

To test the minimum inhibitory (MIC) and bactericidal concentrations (MBC) of antimicrobial agents 2*x* Mueller-Hinton (MH) medium was prepared and autoclaved before usage. Also, a solution of 1 M D-glucose was prepared in MH medium and sterile filtered. Sterile-packed, conical-bottom, low protein binding 96-well polypropylene plates were used for MIC testing. A 1:1 dilution of each antimicrobial agent was prepared across the rows of the plate, down to a low concentration of 1:512. Cultures of either *E. coli* or *S. aureus,* of a population $\geq 1 \times 10^5$ cfu, were pipetted into columns 1 – 11, with the eleventh column having no antimicrobial agent to serve as a control to check for cell growth. The top of the wells were then sealed with an air-permeable plastic film and placed in a 37 °C incubator overnight on an orbital shaker at 60 rpm.

The following morning the plates were removed from the oven and centrifuged for 5 minutes at 1000 x *g*. The wells were then inspected for cell growth by looking through the bottom of the plate for a cell pellet (**Figure 3.9**). The well with the lowest concentration of antimicrobial agent which showed no cell pellet was labeled as the MIC. To test the MBC the contents of all wells with no cell pellet were removed and plated onto MH-Agar plates which were labeled with the concentration of composite used in the MIC test. These were placed in a 37 °C incubator overnight and inspected the following morning for the presence of bacterial colonies. The plate which had been subjected to the

78

lowest composite concentration during MIC testing and showed no bacteria was identified as the MBC.
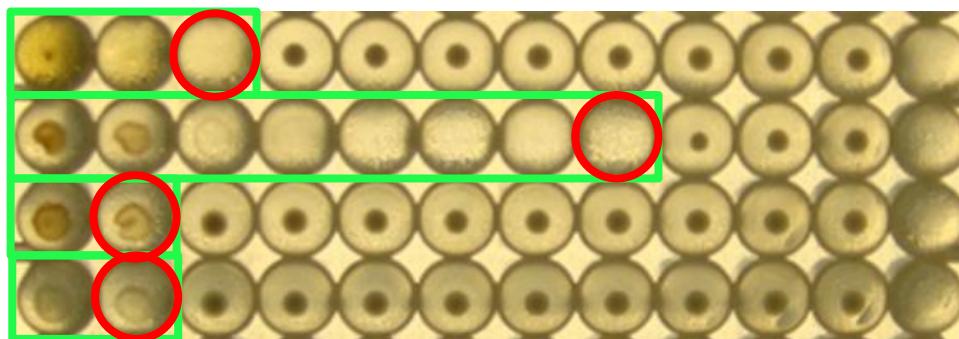
Figure 3.9: Underside view of a 96-well plate upon completion of MIC testing. The concentration of antimicrobial agent decreased from left to right until the tenth well. The wells framed with a red circle denote the MIC, as it was the well furthest right to show no cell pellet. All wells within the green rectangles were used for MBC determination

To ascertain the cell population used in the MIC/MBC tests the test cultures were diluted as follows. After preparation of the MIC tests 10 µL of the inoculation culture was diluted into 990 µL MH medium, which was vigorously mixed and then 100 µL of it was further diluted into 900 µL MH medium for a 10^4 dilution. This was vigorously mixed and 100 µL was extracted and diluted into 900 µL MH medium for a 10^5 dilution. 100 µL of the 10^4 and 10^5 dilutions were plated onto MH plates and incubated overnight in a 37 °C incubator. The following morning the number of colonies on each plate was counted and the numbers averaged for the overall cell count used in the MIC/MBC test.

3.6.4.2 Glucose and H_2O_2 Determination

To investigate any interaction of H_2O_2 with AgNPs the following assays were performed. To assay the activity of GOx-PA, the enzyme-containing particles were resuspended in 18 µL of 1 M D-glucose and 192 µL of 50 mM NaAc pH 5.1, then

incubated for 20 minutes at room temperature under constant shaking. Subsequently, the reaction mixture was filtered through a 0.2 μm pore size filter, and 100 μL of the filtrate was combined with 25 μL of 8 mM oDS and 10 μL of 10 mg mL^{-1} HRP, and incubated for 2 min at room temperature. The absorbance at 460 nm was then recorded. All absorption measurements were recorded on a Biotek Synergy 2 multi-well plate reader (Biotek, Winooski, VT, USA).

To determine the concentration of D-glucose remaining after performing the immobilized GOx-PA activity assay part of the filtrate was subjected to a hexokinase-based glucose determination assay kit (Sigma Aldrich, St. Louis, MO, USA). This kit was chosen since it does not use H_2O_2 for detection, and hence is separate from GOx-PA activity assays. The kit uses hexokinase, ATP, NAD, and Glucose-6-phosphate dehydrogenase to first phosphorylate glucose to glucose-6-phosphate (via hexokinase), and then reduce NAD to NADH (via Glucose-6-phosphate dehydrogenase). NADH has an absorption maximum at 340 nm which was measured using the same plate reader used for GOx activity assays.3.6.4.3 Ag$^+$ Quantification

To quantify Ag$^+$ released by the interaction of t-AgNPs with H_2O_2 the conditions of MIC/MBC tests were mimicked. Composite-coated spheres were placed in MH medium containing 10 mM glucose for 2, 4, 6, and 16 hours at 37 °C. The samples were then filtered in centrifugal filter tubes of 1 kDa MWCO (Millipore Corp., Billerica, MA, USA) to separate silver cations from the composite and any desorbed t-AgNPs, and the filtrate was subjected to elemental analysis via atomic emission spectroscopy at the Chemical Analysis Laboratory at the University of Georgia-Athens (Athens, GA, USA).

3.6.4.4 Exposure Time Viability of *E. coli*

The relative ATP concentration over time was measured my luminescence using the BacTiterGlo Microbial Cell Viability Assay Kit (Promega Corp., Madison, WI). Cultures in polypropylene 96-well plates were completed as performed for MIC/MBC testing, where several replicate wells contained 100 µL of cells and a set concentration of composite material. At regular time intervals 100 µL of BacTiterGlo assay reagent was added to a well and the luminescence was measured according to the manufacturer's instruction using a Synergy 4 microplate reader (Biotek Inc., Winooski, VT).

3.6.4.5 Storage Stability Testing

The retention of antimicrobial activity of the composites after prolonged storage was also gauged. For storage, the composites were placed in a -20 °C freezer for a period of one to three months. For testing, samples were removed, allowed to thaw to room temperature, and MIC/MBC tests were performed as detailed previously.

3.6.5 Functionalized Silk Fibroin Construction and Testing

3.6.5.1 Preparation of Composite-functionalized Silk Fibroins

The preparation of the regenerated silk fibroin and electrospinning of fibroin/polyethylene oxide (PEO) fibers were conducted by modifying the protocols established by Jin *et al.*[24,25] The electrospinning dope was produced through the combination of 2 g aqueous fibroin solution (10.7 wt%) with 2 g of 5 wt% PEO (900 kDa MW) and a 0.5 ml suspension of Stöber spheres at 10 mg/mL in water. It should be noted that the combined fibroin/PEO spin dope should be prepared fresh daily, as extended storage at 4°C results in gelation of this solution. The silk/PEO/Stöber sphere solution was pumped through an 18-gauge blunt-tip needle at a flow rate of 0.5 mL/h

utilizing a syringe pump. A positive DC voltage of 15-17 kV was applied between the spinneret needle and the grounded collection plate. 4" silicon wafers (University Wafer, Inc., Boston, MA, USA) treated with a hydrophobic silane solution (Rain-X) were utilized as the collection plate to facilitate the easy recovery of the non-woven mats. The regenerated fibroin-based electrospun fabrics were annealed in a humidity chamber (100% RH, 25 °C) for 16 h in order to render the fibroin water-insoluble.[24,25]

3.6.5.2 Bacterial Clearing Zone Testing

To test the antimicrobial efficacy of the LbL-coated spheres that had been electrospun in silk fabrics, samples were evaluated on their ability to inhibit *E. coli* and *S. aureus* colony formation in the vicinity of the fabric. This was performed by cutting a patch of silk from the fiber sample and placing it onto an MH-Agar plate supplemented with 10 mM glucose. Prior to placement of silk, 0.1 mL of a growing culture containing 10^5 cells mL^{-1} of either *E. coli* or *S. aureus* was spread onto the surface of the plate and dried at 37 °C. The plates were incubated overnight in a 37 °C incubator overnight. Finally, the distance between the edge of the silk sample and bacteria colonies was measured using a micrometer in six places around each sample and averaged to obtain the "clearing zone," which is the distance around the sample wherein bacteria growth is inhibited.

3.6.6 Table and Figure Data Analysis

All antimicrobial activity assays are the range of values for three independently prepared samples tested with three independently prepared cultures of the specified bacterium. Glucose, H_2O_2, and Ag^+ determination assays are the average and standard deviation of three independently prepared samples. ATP Luminescence data are the

average and standard deviation of eight independently prepared samples. Textile clearing

zone assays are the average and standard deviation of six measurements each from three

independently prepared samples. All cell counts are the average of three independently

prepared cultures, presented as the number of colony forming units (cfu).

3.7 References

1. Kumar, R., and Munstedt, H. (2005) Silver Ion Release from Antimicrobial Polyamide/silver Composites, *Biomater. 26*, 2081.

2. Lansdown, A. B. G. (2010) A Pharmacological and Toxicological Profile of Silver as an Antimicrobial Agent in Medical Devices, *Adv. Pharmacol. Sci. 2010*, 1.

3. Monteiro, D. R., Gorup, L. F., Takamiya, A. S., Ruvollo-Filho, A. C., Camargo, E. R. d., and Barbosa, D. B. (2009) The Growing Importance of Materials that Prevent Microbial Adhesion: Antimicrobial Effect of Medical Devices Containing Silver, *Int. J. Antimicrobial Agents 34*, 103.

4. Rai, M., Yadav, A., and Gade, A. (2009) Silver Nanoparticles as a New Generation of Antimicrobials, *Biotechnol. Adv. 27*, 76.

5. Dibrov, P., Dzioba, J., Gosink, K. K., and Häse, C. C. (2002) Chemiosmotic Mechanism of Antimicrobial Activity of Ag^+ in *Vibrio cholerae*, *Antimicrob. Agents Chemother. 46*, 2668.

6. Dubas, S. T., Kumlangdudsana, P., and Potiyaraj, P. (2006) Layer-by-layer Deposition of Antimicrobial Silver Nanoparticles on Textile Fibers, *Coll. and Surf. A 289*, 105.

7. Jung, W. K., Koo, H. C., Kim, K. W., Shin, S., Kim, S. H., and Park, Y. H. (2008) Antibacterial Activity and Mechanism of Action of the Silver Ion in *Staphylococcus aureus* and *Escherichia coli*, *Appl. Envir. Microb. 74*, 2171.

8. Zan, X., and Su, Z. (2010) Polyelectrolyte Multilayer Films Containing Silver as Antibacterial Coatings *Thin Solid Films 518*, 5478.

9. Lok, C.-N., Ho, C.-M., Chen, R., He, Q.-Y., Yu, W.-Y., Sun, H., Tam, P. K.-H., Chiu, J.-F., and Che, C.-M. (2007) Silver Nanoparticles: Partial Oxidation and Antibacterial Activities, *J. Biol. Inorg. Chem. 12*, 527.

10. Kittler, S., Greulich, C., Diendorf, J., Köller, M., and Epple, M. (2010) Toxicity of Silver Nanoparticles Increases during Storage Because of Slow Dissolution under Release of Silver Ions, *Chem. Mater. 22*, 4548.

11. Vartiainen, J., Rättö, M., and Paulussen, S. (2005) Antimicrobial Activity of Glucose Oxidase-immobilized Plasma-activated Polypropylene Films, *Packaging Technol. and Sci. 18*, 243.

12. Eby, D. M., Schaeublin, N. M., Farrington, K. E., Hussain, S. M., and Johnson, G. R. (2009) Lysozyme Catalyzes the Formation of Antimicrobial Silver Nanoparticles, *ACS Nano 3*, 984.

13. Ben-Yoav, H., and Freeman, A. (2008) Enzymatically Attenuated *in situ* Release of Silver Ions to Combat Bacterial Biofilms: A Feasibility Study, *J. Drug Del. Sci. Tech. 18*, 25.

14. Guo, J.-Z., Cui, H., Zhou, W., and Wang, W. (2008) Ag Nanoparticle-catalyzed Chemiluminescent Reaction Between Luminol and Hydrogen Peroxide, *J. Photochem. and Photobiol. A: Chem. 193*, 89.

15. Cao, H., Zhu, Y., Tang, L., Yang, X., and Li, C. (2008) A Glucose Biosensor Based on Immobilization of Glucose Oxidase into 3D Macroporous TiO_2, *Electroanal. 20*, 2223.

16. Wiegand, I., Hilpert, K., and Hancock, R. E. W. (2008) Agar and Broth Dilution Methods to Determine the Minimal Inhibitory Concentration (MIC) of Antimicrobial Substances, *Nature Prot. 3*, 163.

17. Colorists, A. A. o. T. C. a. (2008) Antibacterial Activity Assessment of Textile Materials: Parallel Streak Method, *AATCC Technical Manual TM 147-2004*.

18. Colorists, A. A. o. T. C. a. (2008) Antibacterial Finishes on Textile Materials: Assessment of, *AATCC Technical Manual TM 100-2004*.

19. Huang, T., and Murray, R. W. (2003) Luminescence of Tiopronin Monolayer-Protected Silver Clusters Changes To That of Gold Clusters upon Galvanic Core Metal Exchange, *J. Phys. Chem. B 107*, 7434.

20. Kobayashi, Y., Katakami, H., Mine, E., Nagao, D., Konno, M., and Liz-Marzan, L. M. (2005) Silica Coating of Silver Nanoparticles Using a Modified Stöber Method *J. Coll. Inter. Sci. 283*, 392.

21. Haase, N. R., Shian, S., Sandhage, K. H., and Kroger, N. (2011) *Adv. Funct. Mater. 21*, 4243.

22. Block, S., ed. (2001) *Disinfection, Sterilization, and Preservation*, 5 ed., Lippincott, Williams, & Wilkins, Philadelphia, PA.

23.   Ivanova, O. S., and Zamborini, F. P. (2010) Size-Dependent Electrochemical Oxidation of Silver Nanoparticles, *J. Am. Chem. Soc. 132*, 70.

24.   Jin, H.-J., Fridrikh, S. V., Rutledge, G. C., and Kaplan, D. L. (2002) Electrospinning *Bombyx mori* Silk with Poly(ethylene oxide), *Biomacromol. 3*, 1233.

25.   Jin, H.-J., Park, J., Karageorgiou, V., Kim, U.-J., Valluzzi, R., Cebe, P., and Kaplan, D. (2005) Water-Stable Silk Films with Reduced β-Sheet Content, *Adv. Funct. Mater. 15*, 1241.

CHAPTER 4: Application of the Protamine-Modified Enzyme Laccase for the

Enhanced Electrocatalytic Reduction of Oxygen

This chapter is distinct from, though represents a summary of the studies presented in the following publication:

Berrigan, J. D.*, Haase, N. R.*; Strack, G.; Cai, Y.; Luckarift, H. R.; Johnson, G. R.; Kröger, N. K.; Sandhage, K. H. *xxxx*, 2012, in preparation.

4.1 Abstract

This chapter presents research utilizing a modified enzyme for the electrocatalytic reduction of dioxygen to water. The oxygen-reducing enzyme laccase was cross-linked to protamine, biochemically characterized, and immobilized onto pressed sheets of multi-walled carbon nanotube electrodes. The quantity and biochemical activity of the immobilized enzyme was also determined. Electrochemical measurements were recorded to ascertain the changes that occur in the electrocatalytic reduction of oxygen and overall performance of the enzymatic cathode upon modification of laccase. The native and modified enzymes are compared, and reasons for the observed changes in electrochemical activity are discussed in correlation with the bio- and electrochemical measurements.

4.2 Introduction

4.2.1 Enzymatic Biofuel Cells

Fuel cells are devices in which chemical energy is directly converted into electrical energy. They differ from conventional electricity generators, which convert

chemical energy first into mechanical energy and then into electrical energy (e.g. those in coal-fired power plants). In the search for more efficient means of green energy, attention is turning towards converting the bond energy of molecules into electricity using biocatalysts.[1-3] Enzymatic biofuel cells are currently being explored as a strategy to accomplish this task, since the reactions of some enzymes involve electron transfer with widely available molecules such as carbohydrates or alcohols. In such fuel cells, oxidoreductase enzymes, which catalyze the exchange of electrons between appropriate biomolecules, electrodes, and oxygen are immobilized on the surfaces of electrodes. The anode is constituted by an enzyme that catalyzes the transfer of electrons from a biomolecule (e.g., alcohol, monosaccharide) to the electrode, while an enzyme on the cathode catalyzes the transfer of electrons to combine oxygen and protons to form water. This chapter presents research at the cathode of an enzymatic biofuel cell.

In enzymatic cathodes two enzymes commonly used are bilirubin oxidase and laccase (Lac),[4-10] with Lac being employed in this research. Laccase from *Trametes versicolor* is a multi-copper oxidase enzyme that catalyzes the four-electron reduction of oxygen to water, **Equation 4.1**, utilizing organic compounds, **Equation 4.2**.[11,12]

$$O_2 + 4e^- + 4H^+ \rightarrow 2H_2O \qquad\qquad E^0 = 1.23 \text{ V} \quad (4.1)$$

$$(4.2)$$
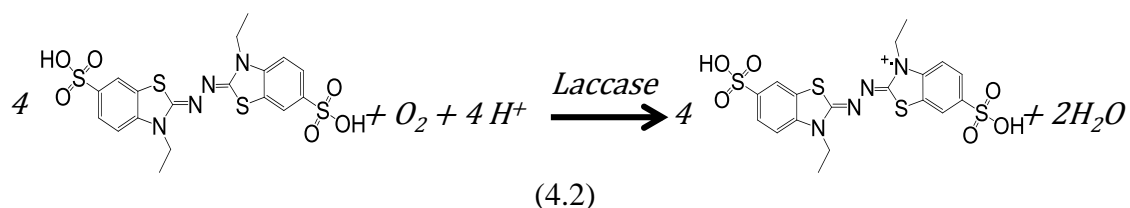
The overall reaction occurs via four one-electron transfers to the enzyme, followed by intra-enzyme electron transfer between the three copper sites, and finishing with the

successive transfer of electrons to O_2, forming two H_2O molecules.[13]   The multi-copper

oxidase Laccase, used in this research, contains four copper atoms in their active site;

they are divided into three separate metal centers. These can be seen in **Figure 4.1** and

consist of T1, T2, and T3 Cu sites. The T1 site accepts electrons from the electrode and

transfers them over 1.3 nm, via histidine-cysteine-histidine hopping, to the T2/T3 sites

(the T3 site is a bi-nuclear copper site) to reduce O_2.[14-16]
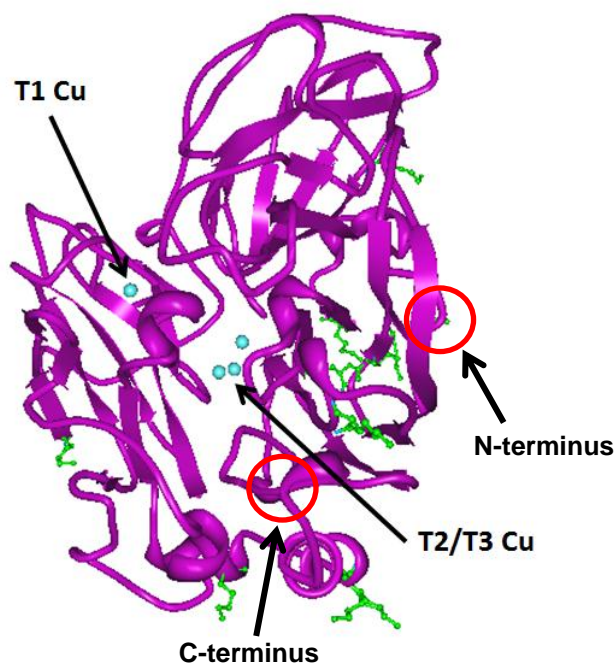
**Figure 4.1:   Crystal structure of Laccase from *Trametes versicolor* (PDB code
1GYC).[11]** The T1 and T2/T3 copper sites are shown in blue; they are separated by 1.3
nm. The eight lysine residues and N-terminus of the protein used for cross-linking are
shown in green. The positions of the N- and C-termini, which are hidden from clear
view, are indicated on the structure.

Laccase from *Trametes versicolor* was selected for use in this research due to its

previous utilization in the development of biocathodes;[8,14,17,18]   the 70 kDa enzyme

contains the T1 copper site 0.12 nm inside the enzyme.[11,14] Current research into the

modification of multi-copper oxidases, including laccase, has focused on improving electron transfer and substrate access characteristics of the active site.[19-22] Mutations of the outer residues on copper efflux oxidase from *E. coli*, which is another multi-copper oxidase enzyme, have resulted in better substrate access to the T1 Cu site,[21] while mutations of inner residues between the T1 and T2/T3 Cu sites increased the redox potential of this enzyme.[20] However, these studies were not aimed at electrochemical applications. Gelo-Pujic et al. truncated the C-terminus of laccase from *Trametes versicolor* and achieved an increased electron transfer rate.[23] The research herein details the cross-linking of laccase with protamine in the hopes of yielding greater enzyme immobilization and better retention of activity upon immobilization, as was observed with GOx-PA in Chapter 2. This enzyme has nine candidate locations for cross-linking to protamine using the BS3 method (detailed in Chapter 2), eight lysine residues and the N-terminus. Cross-linking to protamine was employed since, for GOx, it allowed full retention of enzymatic activity while providing more secure immobilization versus the unmodified enzyme. However, this addition of material to the enzyme is in contrast with the aforementioned studies, which sought to remove amino acids from the enzyme. This approach poses the question of whether or not the aforementioned advantages of protamine cross-linking, namely higher enzyme immobilization and retention of catalytic activity, will outweigh the drawback of having additional distance for DET.

4.2.2 Current Methods for Enzyme Immobilization in Biofuel Cells

An issue of great importance in constructing enzymatic biofuel cells is the immobilization of the enzyme. For DET the enzyme must be in close proximity to an electron transporter, such as the electrode or a molecule which mediates electron transfer

between the electrode and enzyme. The immobilization method must be relatively benign to the enzyme, as disturbing the conformation would be detrimental to the enzyme activity. Since the enzyme must also be close to the electrode the loading capacity of the enzyme is limited, and the amount of electrochemically active enzyme possible to immobilize must be maximized to achieve high total electrocatalytic activity.

Lim and coworkers encapsulated bilirubin oxidase on gold electrodes using a mixture of sol-gel derived silica, polyethylene glycol, and carbon nanotubes (which acted as electron transporters).[10] However, in this method the carbon nanotubes were randomly oriented with respect to both the enzyme and electrode. While this method increased the electron transfer the method does not ensure a direct "wire" between the enzyme and electrode. Hydrogels have also been employed as a matrix for the immobilization of enzymes in biofuel cells and have been utilized to facilitate electron transfer.[24,25] These materials, in which enzymes are immobilized either on the electrode surface or within the hydrogel network, contain immobilized electron transfer mediators to allow enzyme molecules further from the electrode surface to remain electrochemically active.[26] These mediators help shuttle electrons between the enzyme and electrode, but each mediator transfer step is another energy barrier that must be crossed. Direct electron transfer has only one energy barrier, between the electrode and enzyme, which can result in more efficient electron transfer. Furthermore, theoretically the full energy from the oxidation of the substrate biomolecule, or reduction of O_2, can be harnessed. Also, as hydrogels have a random structural organization, electron transfer between the enzyme and electrode along the shortest route of mediators is not ensured.
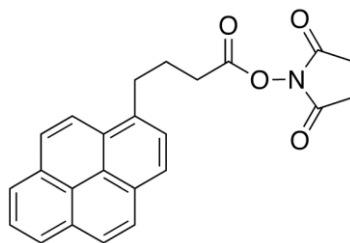
Figure 4.2: Chemical structure of 1-pyrenebutanoic acid, succinimidyl ester (PBSE). The heterobifunctional molecule immobilizes to CNTs via its pyrene group, which is covalently linked to an NHS ester for cross-linking with proteins.

Recent research in enzymatic biofuel cells has been conducted by immobilizing enzymes to carbon nanotube electrodes. This has been achieved by first functionalizing conductive carbon materials with heterobifunctional cross-linking molecules.[8,17,18,27,28] One of these molecules, 1-pyrenebutanoic acid, succinimidyl ester (PBSE), was used in this research, and its structure can be seen in **Figure 4.2**. PBSE forms strong non-covalent interactions with CNTs via π-π stacking interactions using its pyrene moiety. It covalently bonds with proteins through its NHS ester, the predominant reaction site of which is primary amines such as lysine and a protein's N-terminus. However, it has been shown that NHS esters can react with residues containing hydroxyl side chains (serine, threonine, and tyrosine) that are in close proximity to residues with secondary amines, such as arginine.[29,30] Ramasamy et al. used PBSE to immobilize laccase to pressed sheets of multi-walled carbon nanotubes, yielding stark improvements in the biocatalytic performance of the cathode.[17] For this research, serine and threonine residues are present on protamine for the immobilization of cross-linked Lac.

4.2.3 Electrochemical Characterization

In this research cross-linked and native Lac are compared by their electrochemical reduction of oxygen when immobilized to pressed sheets of multi-walled carbon

nanotubes. This process occurs through the transfer of electrons from the nanotubes to the T1-Cu site of Lac, meaning there must be a driving force for the electron to reduce the T1 copper. In this application the driving force is an electrical potential, and in a thermodynamically ideal setting the potential would 1.23 V, the value noted in **Equation 4.1**. However, a thermodynamically ideal setting rarely occurs, and thus there must be an additional potential applied to bring about electron transfer between the enzyme and electrode.[31] This potential, termed the *overpotential*, is given in **Equation 4.3**.

$$\eta = E - E_{eq} \qquad\qquad\qquad (4.3)^{31}$$

E describes the overall potential that must be applied to perform the electron transfer, while E_{eq} describes the thermodynamic potential of the reaction, and is equivalent to E^0 in Equation 4.1. Therefore, η is the overpotential applied to initiate electron transfer, and a smaller overpotential indicates both a more thermodynamically ideal reduction reaction as well as a more efficient electrode.

Basic testing of the biocathode was conducted using cyclic voltammetry (CV) measurements. In this experiment the potential of the electrochemical cell is increased at a constant rate until reaching a specified maximum while recording the current. It is then reduced at the same rate until it reaches a specified minimum value, and this process is repeated as desired. When a redox reaction begins during this measurement the current will change. CV measurements yield basic information on the potential at which the oxidation/reduction reaction begins, allowing for a qualitative examination of how thermodynamically ideal the system is performing.[31]

To obtain quantitative information on the overall electrochemical performance of the biocathode potentiostatic polarization experiments were conducted. In these

measurements the potential of the electrochemical cell is held constant at specified values for specified times while monitoring the current. The measured current is then divided by the area of the electrode to obtain the current density (current per unit area), and the potential is plotted as a function of the current density. This measurement yields information on the overall performance of the cell, including the effect of electron transfer and mass transport on the system.[31] The lifetime measurements used are to simulate the half-cell under load, to evaluate its stability in an application setting.

4.3 Results & Discussion

This section presents the results of biochemical and electrochemical experiments on Lac and Lac-PA immobilized to CNT-BP electrodes. All results will be detailed before they are interpreted together in a discussion subsection.

4.3.1 Characterization of Lac-PA

DLS and zeta potential measurements showed that, at pH 7, Lac possessed a zeta potential of $\zeta = -9.54 \pm 0.94$ mV while Lac-PA exhibited a less negative zeta potential of $\zeta = -3.65 \pm 0.16$ mV. This reduction in negative magnitude is consistent with the presence of multiple protamine moieties to the outer surface of the enzyme. The zeta potential of Lac-PA is likely not positive, as GOx-PA was, due to there being seven fewer sites for protamine cross-linking. Measurement of the enzymatic oxidation of ABTS showed Lac-PA to exhibit only slightly lower activity than the unmodified enzyme (>90 %, **Figure 4.3**) demonstrating that the attached protamine moieties have little effect on catalysis.

93
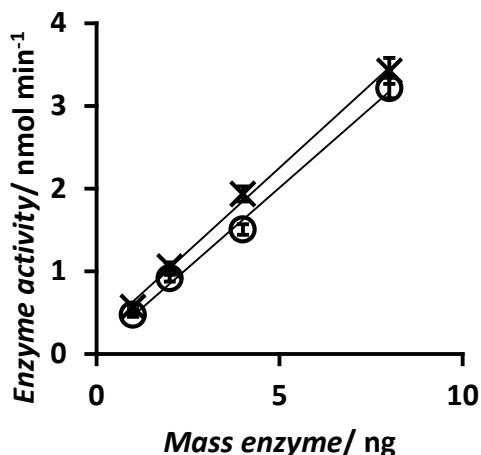
Figure 4.3: Enzymatic activity of Lac (X) and Lac-PA (O). The mass of the enzymes was determined using a BCA protein determination assay, and the activity was measured as the nanomoles of oxygen gas reduced per minute. The results are the average and standard deviation of triplicate measurements.

4.3.2 Biochemical Activity of Immobilized Lac-PA

Both Lac and Lac-PA were subsequently immobilized onto highly conductive (255 S cm^{-1}) pressed multi-walled carbon nanotube sheets (CNT-BP) which had been cut into 0.12 cm^2 discs. Prior to enzyme immobilization, these electrodes were incubated in PBSE, then Lac and Lac-PA were immobilized onto either PBSE-treated or unmodified CNT-BP electrodes. While the primary amines on Lac-PA are likely used during cross-linking, the serine and threonine residues on protamine, which are adjacent to arginine residues, are accessible reaction sites for PBSE. These residues are also present on the laccase moiety of Lac-PA, but they are likely more difficult to access than those on protamine, which is bonded to the surface of laccase.

After incubation of the CNT-BP electrodes with Laccase or Lac-PA, the activity of the bound (electrode) and unbound (supernatant) enzyme was assayed relative to the free enzyme in solution. The mass of enzyme immobilized is shown in **Table 4.1**, while

Table 4.1: **Mass of enzyme immobilized on CNT-BP electrodes.** The mass was calculated by calculating the molar amount of enzyme present in the unbound portion, then subtracting it from the mass of enzyme exposed to the CNT-BP electrodes. The results are the average and standard deviation of triplicate measurements.

Electrode specimen	Mass of enzyme immobilized (µg)
Laccase	175 ± 5
Lac-PA	161 ± 22
PBSE + Laccase	169 ± 4
PBSE ± Lac-PA	191 ± 2

the results of this assay are presented in **Figure 4.4**. Surprisingly, the amount of Lac immobilized on the electrode was essentially identical for both physiorbed and PBSE-tethered Lac. However, when Lac-PA was bound to PBSE-treated electrodes 13% more enzyme was immobilized compared to Lac on PBSE-treated electrodes. Remarkably, the biochemical activity of Lac-PA/PBSE was 48% higher than Lac/PBSE, suggesting
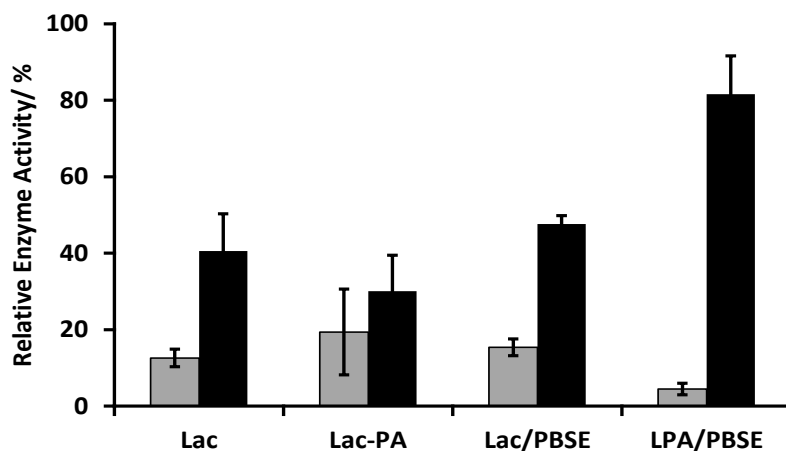
Figure 4.4: **Immobilization of Lac and Lac-PA CNT-BP electrodes.** The specified enzyme (LPA = Lac-PA) was incubated with CNT-BP electrodes that were unmodified or treated with PBSE. The activity of enzyme bound (black bars) or unbound (grey bars) was determined. The results are the average and standard deviation of triplicate measurements.

PBSE-mediated immobilization of Lac-PA is less detrimental to the enzyme's activity. CNT-BP electrodes not functionalized with PBSE revealed no significant difference in either the amount of enzyme immobilized or its relative activity. For both Lac and Lac-PA, physisorption to CNT-BP electrodes led to a decrease in biochemical activity of ~60% compared to the free enzyme in solution, whereas Lac-PA/PBSE electrodes lost only 18% of free enzyme activity. These results demonstrate the high likelihood that protamine is reacting with PBSE, and not the laccase moiety, resulting in a higher retention of enzyme activity upon immobilization.

4.3.3 Electrochemical Activity of Immobilized Lac-PA

4.3.3.1 Open Circuit Potential and Cyclic Voltammetry

Electrochemical testing was conducted to investigate the electrochemical activity, utility, and electrical connection of the enzyme to the CNT-BP electrode. In an O_2 atmosphere, blank and PBSE-treated electrodes showed only capacitive currents, no Faradaic currents, and similar OCPs of 199 ± 4.4 mV ($n = 4$) and 211 ± 3.2 mV ($n = 3$), respectively. The OCPs of all CNT-BP electrodes are presented in **Table 4.2**. CNT-BP electrodes with physisorbed Lac and Lac-PA also had similar OCPs (624 ± 4.5 mV, $n = 4$ and 621 ± 6.3 mV, $n = 3$, respectively), indicating that protamine and BS3 do not significantly impede direct electron transfer from the electrode to the T1 Cu-site of the enzyme on these electrodes.

Table 4.2: Open circuit and onset potential for O_2 reduction in O_2-saturated solutions. The results are the average and standard deviation of triplicate measurements.

Specimen	Open Circuit Potential (mV)	Onset Potential (mV)
Blank	199 ± 4.4	N.A.
PBSE	211 ± 3.2	N.A.
Lac	624 ± 4.5	582 ± 4.2
Lac-PA	621 ± 6.3	606 ± 3.1
Lac/PBSE	641 ± 6.3	602 ± 9.3
Lac-PA/PBSE	657 ± 3.4	635 ± 4.8

CV sweeps of both physisorbed Lac and Lac-PA, displayed in **Figure 4.5**, showed an obvious deflection from the N_2-flushed and bare CNT-BP controls below 600 mV. The onset potentials for Lac and Lac-PA were 582 ± 4.2 mV; $n = 4$ and 606 ± 3.1 mV, $n = 3$, respectively, indicating protamine reduces the voltage necessary for the O_2 reduction reaction. Note that the reversible peaks observed at ~150 mV are characteristic of the CNT-BP and are typically observed in blank electrodes.
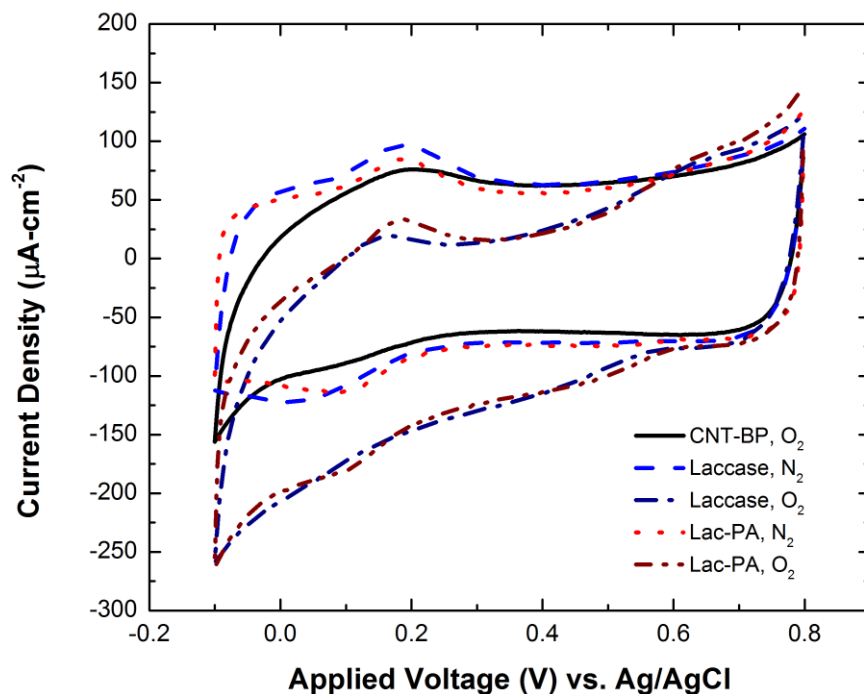
Figure 4.5: Cyclic voltammograms of CNT-BP electrodes with and without Lac or Lac-PA. Experiments were performed in 50 mM NaAc pH 5.1 in both O_2- and N_2-flushed solutions. Data was recorded across ten sweeps at a scan rate of 10 mV s^{-1}.

When Lac and Lac-PA were immobilized to the CNT-BP via PBSE the electrocatalytic activity improved for both enzymes compared to their physisorbed counterparts, as evidenced by the cyclic voltammograms in **Figure 4.6**. The cathodic sweeps of both electrodes in an O_2-flushed solution show an obvious deflection compared to the blank CNT-BP electrodes, as well as enzyme-immobilized electrodes tested in nitrogen-flushed solutions. Lac/PBSE electrodes showed an OCP of 637 ± 3.8 mV; $n = 5$, and reduced O_2 at an onset potential of 602 ± 9.3 mV; $n = 5$. The half-peak potential was 479 ± 22 mV; $n = 5$, and O_2 reduction became mass transport limited at ~400 mV.
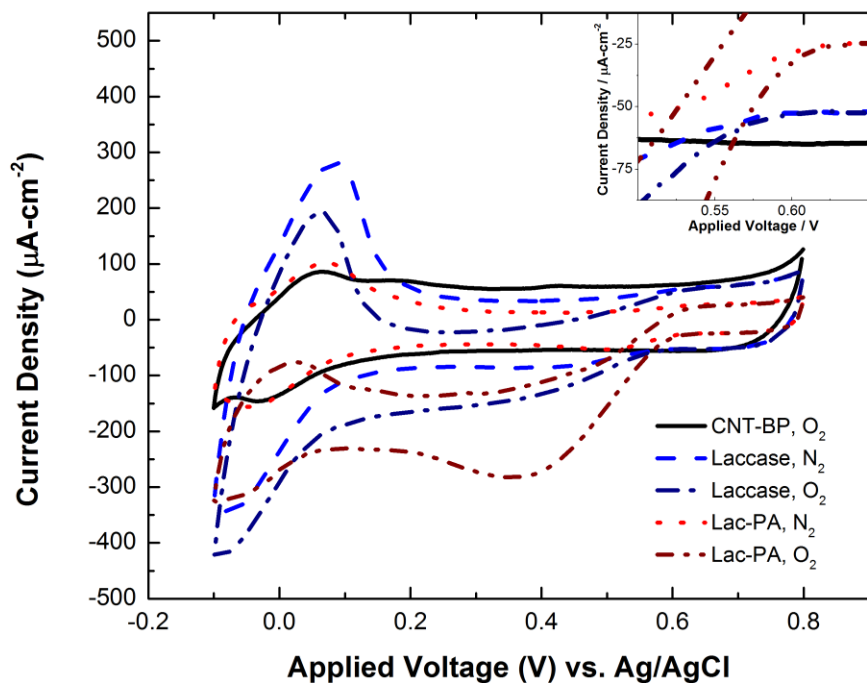
Figure 4.6: **Cyclic voltammograms of PBSE-treated CNT-BP electrodes with Lac and Lac-PA immobilized.** Measurements were performed in O_2- and N_2-flushed solutions of 50 mM NaAc pH 5.1 for ten sweeps at a scan rate of 10 mV s^{-1}. The inset highlights the difference in the onset of oxygen reduction observed with Lac-PA/PBSE electrodes.

These results are in good agreement with previous work using Lac bonded to PBSE-treated CNT-BP electrodes.[17] Lac-PA/PBSE electrodes showed an increase in OCP to 657 ± 3.4 mV; $n = 5$, with an onset potential of 635 ± 4.8; $n = 5$, and half-peak potential of 514 ± 15 mV; $n = 5$. The improvement in the onset potential by ~20 mV is highlighted in the inset of **Figure 4.5** and indicates that the addition of protamine to the outer shell of laccase is facilitating the O_2 reduction reaction. Finally, the reversible peak at 73 ± 13 mV that appears in all specimens was attributed to the bare CNT-BP material.

99

Aerobic potentiostatic polarization curves of all electrodes are shown in **Figure 4.7**. Bare and PBSE-treated CNT-BP electrodes showed minimal current densities (~20 µA cm^{-2}), as expected. Physisorbed Lac and Lac-PA performed similarly to one another, showing low current densities (~55 µA cm^{-2}). This observation could be due to the way these enzymes physisorbed to these electrodes. The CNT-BP electrodes are highly hydrophobic and as such, the favorable enzyme/electrode interaction is for Lac and Lac-PA to expose their inner hydrophobic residues to the CNT-BP material. This deformation of the enzyme conformation is associated with a decrease in catalytic activity. Once the enzyme was immobilized to PBSE-treated CNT-BP electrodes the performance increased significantly. Lac/PBSE electrodes demonstrated current
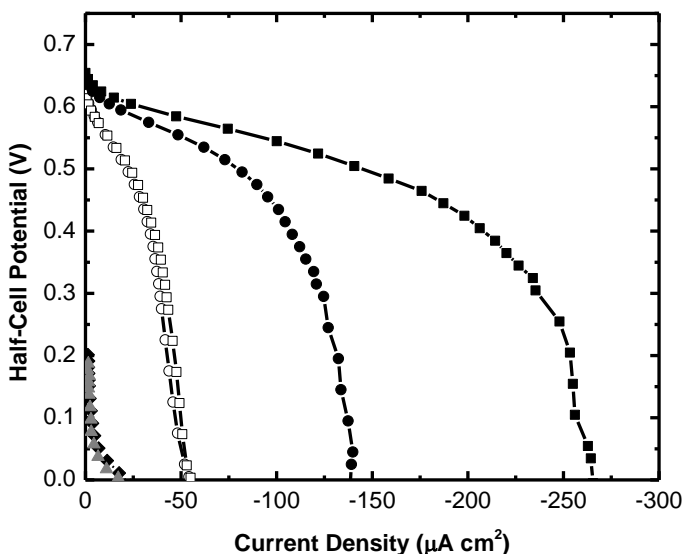
Figure 4.7: Potentiostatic polarization curves of immobilized-enzyme CNT-BP electrodes. The experiments were performed in oxygen-flushed 50 mM NaAc pH 5.1. CNT-BP (closed triangle), PBSE-treated CNT-BP (closed diamond), physiorbed Lac (open circle) and Lac-PA (open square), and PBSE-treated CNT-BP Lac (closed circle) and Lac-PA (closed square). The results are the average of triplicate measurements.

densities in excess of 137 µA cm^{-2}, similar to previous reports.[17] Lac-PA/PBSE showed

an almost two-fold improvement in maximum current density, at 271 µA cm^{-2}.

4.3.3.3 Lifetime Stability Measurements

The lifetimes of PBSE-bonded Lac and Lac-PA CNT-BP electrodes were

measured by monitoring the degradation of OCP and half-cell potential (HCP) after each

cycle of galvanostatic polarization, to simulate an electrical load being placed on the cell.

The results of this experiment are plotted in **Figure 4.8**. While both the native and

modified forms of laccase exhibited identical decreases in OCP, losing only 1% of their

initial potentials, the HCP of the modified enzyme was more stable than native laccase.

Lac-PA on PBSE lost 9 ± 1.5% of its HCP, Lac lost 17.5 ± 1.2% of its HCP. These

results show Lac-PA to retain a greater amount of electrocatalytic activity with repeated

usage, meaning the modified-enzyme cathode remains functional longer than the native

enzyme.
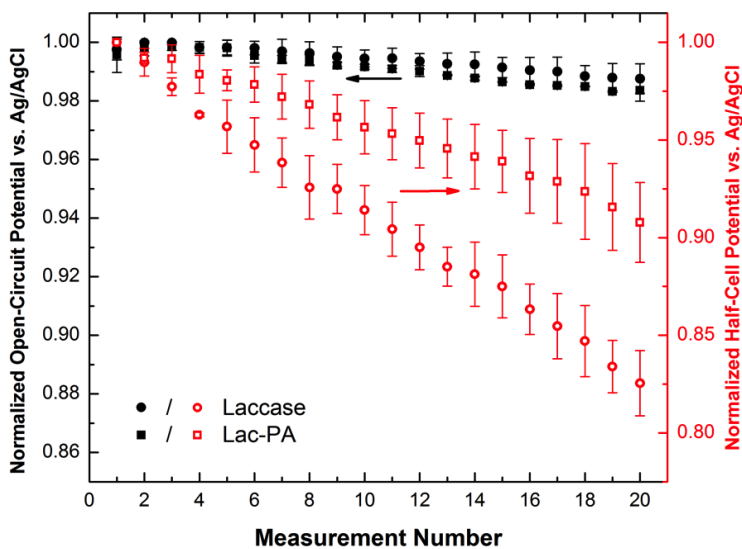
Figure 4.8: Lifetime stability of Lac and Lac-PA on CNT-BP electrodes. The results
are the average and standard deviation of triplicate measurements.

4.3.4 Discussion of Results

The biochemical activity testing indicated that not only does the cross-linking of laccase to protamine improve the molar amount of enzyme immobilized, but the enzyme remains significantly more active on the PBSE-treated electrode surface (**Figure 4.3**). With respect to the purely biochemical reaction, the increase in relative activity on the PBSE-treated CNT-BP surface is larger than the difference in molar quantity of Lac-PA versus Lac immobilized. In electrochemical testing, this difference is also observed in the current density of the Lac-PA/PBSE vs. Lac/PBSE cathodes (**Figure 4.7**). Taken together, the biochemical and electrochemical experimental results indicate the possibility of a secondary benefit to protamine cross-linking. Lac-PA also demonstrated a significant improvement in the O_2 reduction reaction over unmodified laccase both with and, to a lesser extent, without PBSE bonding.

The increase in enzyme immobilization on Lac-PA/PBSE electrodes is interesting in that protamine modification adds a significant mass to the outer shell of the enzyme (~36 kDa). Given that there are a limited number of available PBSE molecules on the CNT-BP to which Lac or Lac-PA can covalently bond, the smaller and unmodified Lac was expected to exhibit higher immobilization conceptually. That more enzyme is immobilized in the case of Lac-PA/PBSE could be due to the possibility of laccase dimers being formed during cross-linking, although efforts were taken to limit their formation.

Given that the DET probability from the electrode to the T1 Cu-site of Lac decays exponentially with distance, the cross-linking of PA to Lac (which occurs on the outer surface of the enzyme) should conceptually increase the tunneling distance, thereby

decreasing DET probability. Thus, the improved catalytic activity of Lac-PA immobilized to PBSE-treated CNT-BP electrodes may be the result of multiple factors which outweigh any increased tunneling distance. In the case of Lac bonding with PBSE, the enzyme could have its conformation distorted when the multiple lysine residues (and N-terminus) react with PBSE; this distortion would lower the enzyme activity. On the other hand, if Lac-PA is bonding to PBSE via serine and threonine residues on protamine, the laccase moiety may suffer less distortion, helping to retain the enzyme activity. This bonding mechanism could also affect the substrate access to the enzyme's active site, as well as the intra-enzyme electron transfer between the Cu sites; both these aspects would affect the overall enzyme activity. In electrochemical testing, Lac-PA may bond to PBSE in a more preferred orientation of the T1 Cu-site to CNT-BP surface. Overall, more research is needed to elucidate the mechanisms primarily responsible for the improved electrocatalysis in PBSE-bonded Lac-PA electrodes.

4.4 Conclusions and Outlook of Modified Enzymes in Biofuel Cells

The research in this chapter detailed the covalent modification of the oxygen-reducing enzyme laccase by cross-linking it with the peptide protamine. This approach resulted in retention of >90% of the enzymatic activity. The modified laccase was then immobilized to pressed sheets of multi-walled carbon naontubes that had been modified with adsorbed 1-pyrenebutanoic, succinimidyl ester. This immobilization resulted in both a higher molar amount of modified laccase being immobilized and a greater retention of enzymatic activity on the electrode, compared to the unmodified enzyme. When electrochemical measurements were performed the modified enzyme showed

improved oxygen reduction over the native enzyme, as well as greater current density, owing to the higher degree of total enzymatic activity on the electrode. These advantages were realized despite the addition of ~36 kDa of mass to the outer shell of the enzyme, which should decrease the probability of direct electron transfer from electrode to enzyme.

Future research in this area of enzyme modification and immobilization would be in the genetic modification of the outer surface of the enzyme. While this modification proved advantageous towards the electrochemical activity, the construction of an enzyme that can be expressed and put to immediate use in a biofuel cell, versus the cross-linking and additional purification process presented here. These fusion enzymes would contain specific domains for surface immobilization that are inserted into an enzyme's amino acid sequence. This strategy could result in even greater gains in the degree of enzyme immobilized, better retention of activity once immobilized, and direct electron transfer from the electrode to the enzyme. This work would complement current research in the genetic modification of an enzyme's active site, which is also directed at achieving superior electrocatalytic activity. A combination of these approaches would result in a genetically engineered enzyme containing domains with superior surface immobilization and electrocatalytic abilities.

4.5 Materials & Methods

4.5.1 Materials

The materials used for cross-linking GOx and PA and zeta potential measurements in section 2.6.3 were used here for cross-linking Laccase (Lac) to PA. The

materials used for immobilizing enzymes to electrodes are as follows. Laccase was supplied from Sigma-Aldrich, St. Louis, MO, USA. The electrodes used were pressed sheets (27.6 ± 4 μm thick) of mult-walled carbon nanotubes (known as buckypaper, referred to as CNT-BP) were sourced from Buckeye Composites, Kettering, OH, USA. Dimethyl sulfoxide (DMSO) was sourced from ThermoFisher, Rockford, IL, USA. 1-pyrenebutanoic acid, succinimidyl ester (PBSE) was purchased from Anaspec Inc., Fremont, CA, USA. The filter paper used was 185 mm diameter, Grade 1, from Whatman, Piscataway, NJ, USA.

For electrochemical testing Glassy carbon working electrodes were purchased from CH Instruments Inc., Austin, TX, USA, and capped with a Teflon™ cap which had a 0.5 cm^2 hole in the center. These electrodes were placed in a voltammetric cell from Ace Glass, Vineland, NJ, USA. To complete the apparatus a platinum counter electrode was used in conjunction with a Ag/AgCl reference electrode (MF-2013 and MF-2052, respectively, BASi Inc., West Lafayette, IN, USA). These experiments were conducted in solutions bubbled continuously with either ultra-high purity N_2 or O_2 (Airgas, Atlanta, GA, USA).

4.5.2 Cross-linking and Characterization of Laccase with Protamine

The enzyme Laccase (Lac, from *Trametes Versicolor*) was cross-linked to protamine (making Lac-PA) using a procedure similar to the one used to form GOx-PA in section 2.6.3, with the following changes. As there are nine primary amine groups on each Lac subunit (eight lysines and the N-terminus), a 20:1 PA:Lac ratio was used, while the BS3:Lac ratio was 40:1. Lac was prepared for use by dialyzing against 3 changes of 20 mM potassium phosphate pH 5.8, then frozen in liquid nitrogen, lyophilized for at

least 24 h, and stored at -20 °C until used. For cross-linking, Lac was diluted to 1 mg

mL^{-1} in 50 mM NaAc pH 5.1; all other conditions and procedures for cross-linking were

held constant. Zeta potential measurements were performed according to section 1.5.2.2.

4.5.3 Laccase Enzymatic Activity Measurement

Lac or Lac-PA was used at a stock concentration of 1 µg mL^{-1} in 50 mM NaAc

pH 5.1. 2,2'-azino-bis(3-ethylbenzothiazoline-6-sulphonic acid, ABTS 20 mM) was used

at a concentration of 5 mM in 50 mM NaAc pH 5.1. The assay was incubated for 20 min

at RT followed by recording the absorption at 418 nm. The percentage of "relative

enzyme activity" was obtained by comparing the activity of Lac (or Lac-PA)

immobilized within a given specimen to that of the corresponding free enzyme in

solution.

4.5.4 Laccase Immobilization to Multi-walled Carbon Nanotubes

The CNT-BP electrodes were functionalized by incubating them for 1 h at RT in

300 µL of 10 mM PBSE in DMSO. Control electrodes, on which the enzyme was

physisorbed, were incubated in DMSO for 1 h at RT. After incubation all electrodes

were blotted dry on filter paper. The electrodes were then incubated in 1 mL of 50 mM

NaAc pH 5.1 containing 0.2 mg mL^{-1} enzyme for 1 h at 4 °C, then rinsed three times in 1

mL 50 mM NaAc pH 5.1 and stored at 4 °C until used. All supernatants were kept for

activity measurements.

4.5.5 Electrochemical Characterization of Enzymatic Cathodes

Enzyme-functionalized CNT-BP electrodes were retained in Teflon^{TM}-capped

glassy carbon working electrodes and tested in a voltammetric cell containing 200 mL 50

mM NaAc pH 5.1, a platinum counter electrode, and a Ag/AgCl reference electrode, and

continuously bubbled with ultra-high purity O_2 or N_2. All electrochemical measurements were recorded using a potentiostat and the associated software (Gamry Instruments Reference 600 Potentiostat/Galvanostat/ZRA; Gamry EChem Analyst Software, v. 5.65; Warminster, PA, USA). The open-circuit potential (OCP) was observed every second for 20 min. CV measurements were obtained by scanning the potential range of 0.7 to -0.1 V at rate of 10 mV s^{-1} while recording data every second for ten cycles.

Potentiostatic polarization measurements were obtained only under O_2 bubbling. An over-potential, η ($\eta = E - E_{eq}$), was applied over the range of 0.0 to -0.7 V, at intervals of 20 mV, for 15 min. During this time the current was measured.

4.5.6 Enzymatic Cathode Lifetime Measurement

The lifetime stability of the enzymatic cathodes was determined using the following procedure. Under O_2 bubbling a current density of 40 µA cm^{-2} was applied for 4 h and the potential was recorded at every 10 sec. This process was repeated 20 times. While the measured potential did decrease when the current was first applied, it did not drop by more than 0.1 V. This procedure was developed and performed by J. Dan Berrigan.

4.5.7 Table and Figure Data Analysis

All biochemical assay data are the average and standard deviation of three independently prepared samples. Open Circuit, Onset, and Polarization Potential data are the average and standard deviation of three independently prepared measurements, as are the lifetime stability measurement data.

4.6 References

1.   Barton, S. C., Galloway, J., and Atanassov, P. (2004) Enzymatic Biofuel Cells for Implantable and Microscale Devices, *Chem. Rev. 104*, 4867.

2.   Minteer, S. D., Liaw, B. Y., and Cooney, M. J. (2007) Enzyme-based Biofuel Cells, *Curr. Op. in Biotechnol. 18*, 228.

3.   Willner, I., Yan, Y.-M., Willner, B., and Tel-Vered, R. (2009) Integrated Enzyme-Based Biofuel Cells – A Review, *Fuel Cells 9*, 7.

4.   Mano, N., Fernandez, J. L., Kim, Y., Shin, W., Bard, A. J., and Heller, A. (2003) Oxygen Is Electroreduced to Water on a "Wired" Enzyme Electrode at a Lesser Overpotential than on Platinum, *J. Am. Chem. Soc. 125*, 15290.

5.   Song, J., Shin, H., and Kang, C. (2011) A Carbon Nanotube Layered Electrode for the Construction of the Wired Bilirubin Oxidase Oxygen Cathode, *Electroanal. 23*, 2941.

6.   Blanford, C. F., Heath, R. S., and Armstrong, F. A. (2007) A Stable Electrode for High-potential, Electrocatalytic O_2 Reduction Based on Rational Attachment of a Blue Copper Oxidase to a Graphite Surface, *ChemComm 43*, 1710.

7.   Ivnitski, D. M., Khripin, C., Luckarift, H. R., Johnson, G. R., and Atanassov, P. (2010) Surface Characterization and Direct Bioelectrocatalysis of Multicopper Oxidases, *Electrochim. Acta 55*, 7385.

8.   Parimi, N. S., Umasankar, Y., Atanassov, P., and Ramasamy, R. P. (2012) Kinetic and Mechanistic Parameters of Laccase Catalyzed Direct Electrochemical Oxygen Reduction Reaction, *ACS Catal. 2*, 38.

9.   Xu, F. (1997) Effects of Redox Potential and Hydroxide Inhibition on the pH Activity Profile of Fungal Laccases, *J. Biol. Chem. 272*, 924.

10.   Lim, J., Cirigliano, N., Wang, J., and Dunn, B. (2006) Direct Electron Transfer in Nanostructured Sol–gel Electrodes Containing Bilirubin Oxidase, *Phys. Chem. Chem. Phys. 9*, 1809.

11.   Piontek, K., Antorini, M., and Choinowski, T. (2002) Crystal Structure of a Laccase from the Fungus *Trametes versicolor* at 1.90-Å Resolution Containing a Full Complement of Coppers, *J. Biol. Chem. 277*, 37663.

12.   Thurston, C. F. (1994) The Structure and Function of Fungal Laccases, *Microbiol. 140*, 19.

13.   Lee, S.-K., George, S. D., Antholine, W. E., Hedman, B., Hodgson, K. O., and Solomon, E. I. (2002) Nature of the Intermediate Formed in the Reduction of O_2 to H_2O at the Trinuclear Copper Cluster Active Site in Native Laccase, *J. Am. Chem. Soc. 124*.

14.	Ivnitski, D. M., and Atanassov, P. (2007) Electrochemical Studies of Intramolecular Electron Transfer in Laccase from *Trametes versicolor*, *Electroanal. 19*, 2307.

15.	Quintanar, L., Stoj, C., Taylor, A. B., Hart, P. J., Kosman, D. J., and Solomon, E. I. (2007) Shall We Dance? How A Multicopper Oxidase Chooses Its Electron Transfer Partner, *Acc. Chem. Res. 40*, 445.

16.	Solomon, E. I., Sundaram, U. M., and Machonkin, T. E. (1996) Multicopper Oxidases and Oxygenases, *Chem. Rev. 96*, 2563.

17.	Ramasamy, R. P., Luckarift, H. R., Ivnitski, D. M., Atanassov, P. B., and Johnson, G. R. (2010) High Electrocatalytic Activity of Tethered Multicopper Oxidase–carbon Nanotube Conjugates, *ChemComm 46*, 5977.

18.	Strack, G., Luckarift, H. R., Nichols, R., Cozart, K., Katz, E., and Johnson, G. R. (2011) Bioelectrocatalytic Generation of Directly Readable Code: Harnessing Cathodic Current for Long-term Information Relay, *Chem. Comm. 47*, 7662.

19.	Hong, G., Ivnitski, D. M., Johnson, G. R., Atanassov, P., and Pachter, R. (2011) Design Parameters for Tuning the Type 1 Cu Multicopper Oxidase Redox Potential: Insight from a Combination of First Principles and Empirical Molecular Dynamics Simulations, *J. Am. Chem. Soc. 133*, 4802.

20.	Kataoka, K., Hirota, S., Maeda, Y., Kogi, H., Shinohara, N., Sekimoto, M., and Sakurai, T. (2011) Enhancement of Laccase Activity through the Construction and Breakdown of a Hydrogen Bond at the Type I Copper Center in *Escherichia coli* CueO and the Deletion Mutant ⊿R5-7 CueO, *Biochem. 50*, 558.

21.	Kataoka, K., Komori, H., Ueki, Y., Konno, Y., Kamitaka, Y., Kurose, S., Tsujimura, S., Higuchi, Y., Kano, K., Seo, D., and Sakurai, T. (2007) Structure and Function of the Engineered Multicopper Oxidase CueO from *Escherichia coli*—Deletion of the Methionine-Rich Helical Region Covering the Substrate-Binding Site, *J. Mol. Biol. 373*, 141.

22.	Chen, Z., Durao, P., Silva, C. S., Pereira, M. M., Todorovic, S., Hildebrandt, P., Bento, I., Lindley, P. F., and Martins, L. O. (2010) The Role of Glu498 in the Dioxygen Reactivity of CotA-laccase from *Bacillus subtilis*, *Dalton Trans. 39*, 2875.

23.	Gelo-Pujic, M., Kim, H.-H., Butlin, N. G., and Palmore, G. T. R. (1999) Electrochemical Studies of a Truncated Laccase Produced in *Pichia pastoris*, *Appl. Environ. Microbiol. 65*, 5515.

24.	Chen, T., Barton, S. C., Binyamin, G., Gao, Z., Zhang, Y., Kim, H.-H., and Heller, A. (2001) A Miniature Biofuel Cell, *J. Am. Chem. Sco. 123*, 8630.

25.	Heller, A. (2004) Miniature Biofuel Cells, *Phys. Chem. Chem. Phys. 6*, 209.

26.   Heller, A. (2006) Electron-conducting Redox Hydrogels: Design, Characteristics and Synthesis, *Curr. Op. in Chem. Biol. 10*, 664.

27.   Lau, C., Adkins, E. R., Ramasamy, R. P., Luckarift, H. R., Johnson, G. R., and Atanassov, P. (2012) Design of Carbon Nanotube-Based Gas-Diffusion Cathode for O_2 Reduction by Multicopper Oxidases, *Adv. Energy Mater. 2*, 162.

28.   Chen, R. J., Zhang, Y., Wang, D., and Dai, H. (2001) Noncovalent Sidewall Functionalization of Single-Walled Carbon Nanotubes for Protein Immobilization, *J. Am. Chem. Soc. 123*, 3838.

29.   Mädler, S., Bich, C., Touboul, D., and Zenobi, R. (2009) Chemical Cross-linking with NHS Esters: a Systematic Study on Amino Acid Reactivities, *J. Mass. Spectrom. 44*, 694.

30.   Mädler, S., Gschwind, S., and Zenobi, R. (2010) Role of Arginine in Chemical Cross-linking with N-hydroxysuccinimide Esters, *Anal. Biochem. 398*, 123.

31.   Bard, A. J., and Faulkner, L. R. (2001) *Electrochemical Methods: Fundamentals and Applications*, 2nd ed., John Wiley & Sons, Inc., Hoboken, NJ.

CHAPTER 5:   STRUCTURE-FUNCTION CORRELATION IN SYNTHETIC PEPTIDE ADSORPTION AND MINERAL DEPOSITION

5.1 Abstract

This chapter presents initial research to elucidate the structure-function relationships of poly-arginine-rich peptides towards gaining a greater understanding of the polyamine-induced mineral deposition process. This phenomenon is explored by investigating how the content and distribution of arginine residues in synthetic peptides affects the ability of these molecules to adsorb to silica and titanium oxide surfaces, and then subsequently to deposit titanium oxide. In addition to the role of arginine, the effect of serine and the N- and C-termini on adsorption and mineral deposition is discussed. Both short- and long-term research outlooks will be discussed, with the short-term outlook presented alongside discussion of the current results; the long-term outlook will be discussed at the conclusion of this chapter.

5.2 Introduction

5.2.1 Structure-function Relationships of Biomineralizing Peptides

The general principles of natural and biomimetic mineralization are known, but many questions remain. Mizutani, *et al*. reported that polyamine polymers could induce the polymerization of silicic acid to silica, suggesting that amine groups facilitate proton transfer between silanol and silanolate groups.[1]   A naturally-occurring example of this polyamine was reported by Kröger, *et al*., wherein peptides isolated from diatom cell

walls, called silaffins, were posttranslationally modified by the addition of *N*-methyl-propylamine oligomers and could precipitate silica from silicic acid solutions.[2] Fang, *et al*. demonstrated that the poly-arginine cationic peptide protamine could be used to deposit titania from an aqueous precursor in a biomimetic fashion.[3] The structures of the mineral precursors from these studies, silicic acid and TiBALDH, are shown in **Figure 5.1**.
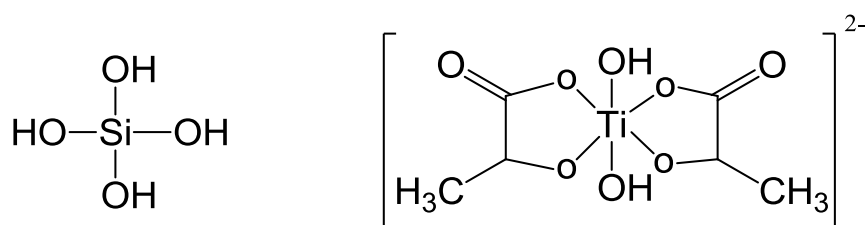
Figure 5.1: Chemical structures of the aqueous mineral precursor molecules silicic acid (left) and TiBALDH (right).

It is thought that when multiple precursor molecules are brought in close proximity by interacting with adjacent amine side chains on peptides, the local precursor concentration rises to a critical level to induce condensation of the precursor to a mineral oxide.[4-8] Ahn, *et al*. investigated the Ti-O precipitation ability of oligo-lysine chains, ranging in length from 1 − 8 lysine residues, and found that as the number of lysines in the oligomer increased, Ti-O mineralization occurred faster and more TiBALDH molecules interacted with the oligomer chains.[6] The incorporation of lysine oligomers into precipitated Ti-O was observed by the presence of amide groups in FT-IR spectra of precipitates, as well as the decomposition of lysine during thermogravimetric analysis.[6]

It is has also been postulated that hydroxyl-functional amino acids can contribute to the mineral precipitation process by the formation of hydrogen bonds with mineral precursors.[4,8,9] The influence of both amine and hydroxyl groups on mineral precipitation was investigated by Cha and co-workers, who tested the Si-O precipitation ability of a range of co-polypeptides.[9] They observed that co-polypeptides consisting of serine and lysine exhibited different Si-O morphologies than precipitates of lysine polypeptides.[9] Also, Kröger, *et al*. noted the presence of multiple serine residues in silaffin peptides.[2] Due to the evident influence of amine and hydroxyl groups on biomimetic mineral precipitation, this research will focus on the contribution of the cationic amino acid arginine, and the hydroxyl-containing amino acid serine, to peptide adsorption and mineral deposition (**Figure 5.2**).
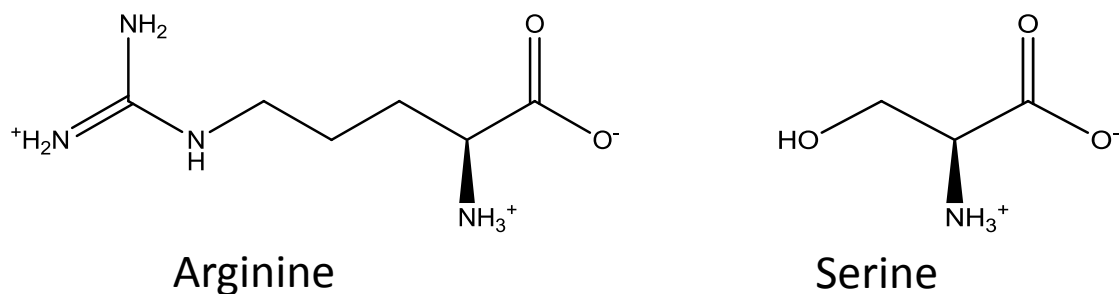
Figure 5.2: Chemical structures of arginine and serine.

In the adsorption of peptides to surfaces, it is generally accepted that electrostatic attraction of positively-charged polyamines towards negatively-charged surfaces is responsible for the adsorption of mineral-precipitating peptides and polymers.[3,10,11] However, the charge characteristics needed to enable electrostatic surface adsorption are not well understood; it is also not known if the same residues responsible for surface

adsorption contribute to subsequent mineral deposition. In studying peptide adsorption to mineral oxides, Gertler, *et al.* studied the adsorption of the peptide Lys-(Gly)$_5$-Lys to 10 μm diameter TiO$_2$ particles.[12] The heptapeptide adsorbed to both anatase and rutile TiO$_2$ at pH 7.4 in Tris and phosphate buffers. However, the peptide desorbed from anatase and rutile TiO$_2$ at 80 and 220 mM NaCl, respectively, in Tris buffer. In phosphate buffer NaCl concentrations of 460 and 240 mM were necessary for peptide desorption from anatase and rutile TiO$_2$, respectively. This experiment proved electrostatic interaction to be the mechanism of adsorption, and also that the crystal structure of the surface, as well as the buffering salt, are important for adsorption. It was observed that Tris adsorbed to TiO$_2$; this adsorption was thought to be responsible for desorption of the peptide at lower salt concentrations in Tris versus phosphate buffer. These results in agreement with the finding of Fang, *et al.* that protamine could not induce Ti-O deposition in 1 M NaCl.[3]

Focusing on the peptide, Phillips, *et al.* and Mermut and coworkers studied the effects of sequence, length, and side chain on the adsorption of binary 7- and 14-mer peptides to silica and polystyrene surfaces.[13,14] The general sequence of 14-mers was Ac-XYYXXYXXYYXXYX-NH$_2$, the general 7-mer sequence was Ac-XYXYXYX-NH$_2$, and the X and Y amino acid pairings were leucine (L) with lysine (K), alanine (A) with lysine, alanine with arginine (R), and phenylalanine (F) with arginine. The N-termini of these peptides were acetylated ("Ac") and the C-termini were amidated ("NH$_2$"). From quartz crystal microbalance measurements, it was found that all 14-mer peptides adsorbed to silica-coated sensors; the only 7-mer peptide to show appreciable adsorption contained alanine and arginine.[13] Of the 14-mer peptides, A-R showed 44% more adsorption than A-K. This result, along with A-R being the only 7-mer peptide to adsorb

to silica, indicates that arginine may have a stronger interaction with silica than lysine, possibly owing to the multiple amine groups in the amino acid side chain. In using Sum Frequency Generation (SFG) vibrational spectroscopy and circular dichroism (CD) spectroscopy Mermut, *et al*. found 14-mer lysine-leucine peptides to exhibit an *α*-helical structure and that the lysine side-chain was responsible for its adsorption to silica.[14]

While the above studies demonstrate the important role of amine-containing amino acids in mineral precipitation and peptide adsorption, there has not been much study on peptides used for surface deposition of minerals, which is a combination of these two actions. The research herein begins to investigate the sequence, length, and side chain influences on the ability of peptides to adsorb to silica and Ti-O surfaces and subsequently deposit Ti-O coatings on the surface. The number and distribution of arginine residues will be investigated to see how these parameters affect adsorption and mineral deposition. Furthermore, the effect of non-amine-containing residues on the adsorption and mineral deposition process will be investigated, as Phillips showed the influence of uncharged side chains on peptide adsorption[13] and Cha, *et al*. revealed that hydroxyl-containing amino acids such as serine can control the morphology of Si-O precipitates.[9]

5.2.2 Quartz Crystal Microbalance Measurement

In these research efforts, Quartz Crystal Microbalance (QCM) measurements were employed to investigate peptide adsorption and mineral deposition. This method enables the real-time observation of the interaction of molecules with a surface. In this method a piezoelectric quartz crystal is placed between two gold electrodes and is oscillated by the driving force of a constant electrical potential. The surface of one of the

electrodes can be coated with a variety of materials; in this research sensors were coated with 50 nm of amorphous silica. As material adsorbs to the surface, the oscillation frequency decreases, while it increases when material dissociates from the surface. The change in frequency is directly proportional to the mass which adsorbs or desorbs from the surface. This relationship is given in the Sauerbrey relation (**Equation 5.1**), wherein the mass adsorbed is treated as an extension of the sensor surface:

$$\Delta m = -C\frac{1}{n}\Delta f \qquad\qquad (5.1)^{15}$$

Δm is the change in mass on the sensor; C is the mass sensitivity constant of the sensor (17.7 ng Hz^{-1} cm^{-2} for sensors used herein), n is the overtone of the sensor monitored (the seventh harmonic was used in this appendix), and Δf is the change in frequency. The overtone is a vibration frequency of the sensor which is higher than the fundamental frequency. As the overtone recorded increases, the area of the sensor sampled decreases. This decrease in sampled area decreases the sensitivity of the measurement, which can be useful to omit noise caused by issues such as turbulent fluid flow over the sensor. The 1st, 3rd, 5th, 7th, 9th, 11th, and 13th overtones are monitored during QCM measurement, allowing for data analysis with an overtone exhibiting the highest signal-to-noise ratio. The seventh overtone was used for all data analysis presented herein. Since QCM measurements record the change in frequency, and not the absolute frequency, any differences between samples do not affect their comparison. Finally, this method can detect nano-gram changes in molecules interacting with the sensor surface.

5.3 Experimental Methodology

5.3.1 Amino Acid Selection

This investigation focused on those factors thought to exert the greatest effect on adsorption and mineral deposition. The peptide protamine is LbL-capable,[3] and the most abundant residues in protamine are arginine and serine (**Table 5.1**). The number and distribution of arginine residues was the primary factor studied. Secondary factors studied were the N-terminus and serine. The influence of the N-terminus could increase with decreasing arginine content, and substitution of serine for non-hydroxyl residues could influence the adsorption and/or mineral deposition ability of the peptides studied.

Table 5.1: **The sequence of the biomimetic mineralizing peptide protamine**. Arginine residues are shown in **bold red**, while serine residues are shown in **bold blue**.

Peptide	*Sequence*
Protamine	H_3N^+-A**RRRRSSSR**PI**RRRR**P**RRR**TT**RRRR**AG**RRRR**-CO_2^-

5.3.2 Peptide Design

To study the aforementioned questions, synthetic peptides with specific sequences were used. Most peptides tested were 16 residues in length, which is about half the length of protamine (31 residues). The peptides were assessed regarding their ability to adsorb to silica surfaces and, subsequently, to deposit a mineral oxide layer on the surface. Silica was chosen as the foundation due to its use in characterizing protamine-induced mineral oxide coatings in Chapter 1, as well as the high cost of titania-coated

sensors. Ti-O was chosen for deposition instead of Si-O because silicic acid is prone to auto-polycondensation, which could result in uncontrolled silica formation not induced by adsorbed peptide molecules.

All 16-residue peptides consisted of arginine, serine or alanine, and one tryptophan residue. Tryptophan was included since its spectroscopic absorption at 278 nm allows for accurate determination of peptide concentration. The peptides were named using a system which identified the number and size of arginine clusters, and the number of non-arginine residues in the peptide, and the identification of the non-arginine residues present (with the exception of tryptophan). For example, the peptide with sequence H_3N^+-RRRRSSSSWSSSRRRR-CO_2^- is identified as $R_4R_4S_7$, where R_4R_4 denotes two separate clusters of four arginine residues, and S_7 denotes seven serine residues in the peptide. In alanine-containing peptides the alanine content is denoted using the same system as for serine notation. For single arginine clusters located at the N- or C-terminus, "n" and "c," respectively, were used to denote the location of the cluster. "Ac" denotes the N-terminus was acetylated, while "cam" denotes the C-terminus was amidated. In cases where all arginine residues were spaced evenly across the sequence the peptide was identified as "eR_x." A full list of the peptides used in this study can be found in **Table 5.2**. The peptides 5R and 6R denote peptides with just five or six arginine residues.

Table 5.2: Synthetic peptides used in this study.

Peptide Name	Sequence
$R_5R_4S_6$	RRRRRSSSWSSSRRRR
$R_4R_5S_6$	RRRRSSSSWSSRRRRR
eR_8S_7	RSRSRSRSWRSRSRSR
$R_4R_4S_7$	RRRRSSSSWSSSRRRR
$R_4R_3S_8$	RRRRSSSSWSSSSRRR
$R_3R_4S_8$	RRRSSSSSWSSSRRRR
nR_7S_8	RRRRRRSSWSSSSSSS
$R_3R_3S_9$	RRRSSSSSWSSSSRRR
$R_3R_3S_8A_1$	RRRSSSSSWSSSARRR
$R_3R_3S_5A_4$	RRRASASSWSASARRR
$R_3R_3A_9$	RRRAAAAAWAAAAARR
$R_2R_2R_2S_9$	RRSSSSSRRSSWSSRR
eR_6S_9	RSRSRSSRSWSRSSSR
nR_6S_9	RRRRRRSSWSSSSSSS
cR_6S_9	SSSSSSSSWSRRRRRR
Ac-cR_6S_9	Ac-SSSSSSSSWSRRRRRR
cam-cR_6S_9	SSSSSSSSWSRRRRRR-cam
camAc-cR_6S_9	Ac-SSSSSSSSWSRRRRRR-cam
R_6	RRRRRR
R_5	RRRRR
nR_5S_{10}	RRRRRSSSWSSSSSSS
cR_5S_{10}	SSSSSSSSWSSRRRRR
$R_3R_2S_{10}$	RRRSSSSSWSSSSSRR
$R_2R_2S_{11}$	RRSSSSSSWSSSSSRR

5.4 Results & Discussion

5.4.1 Identifying the Minimum Arginine Content for Adsorption and Mineral Deposition

QCM observation of protamine adsorption and subsequent Ti-O mineral deposition was measured to profile the standard behavior of this peptide-induced mineral deposition method when subjected to QCM analysis (**Figure 5.3**). Protamine was flowed over the sensor, resulting in 27.3 ± 0.8 ng cm^{-2} protamine adsorption (a 10.8 Hz drop in frequency), and washing until the resonance frequency stabilized with 21.2 ± 1.3 ng cm^{-2} protamine adsorbed. This observation demonstrated that some protamine desorbed from the sensor during washing, perhaps due to crowding on the surface. Exposure of the protamine-coated sensor to TiBALDH resulted in 111.8 ± 1.5 ng cm^{-2} Ti-O deposition,
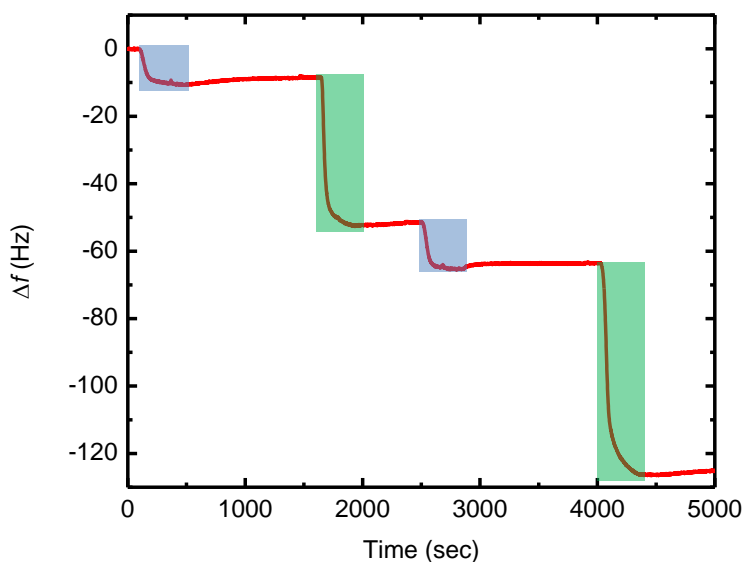
Figure 5.3:   QCM observation of protamine adsorption and Ti-O deposition. The blue-shaded regions indicate when protamine was present in the sample chamber, while green-shaded regions indicate when TiBALDH was present. Un-shaded regions denote only washing buffer in the chamber.

with no desorption during subsequent washing. The Ti-O-coated sensor was then subjected to protamine adsorption and additional Ti-O deposition This cycle resulted in the addition of 30.6 ± 0.6 ng cm^{-2} protamine and 155.5 ± 1.3 ng cm^{-2} Ti-O, demonstrating 44% and 39% increases in peptide adsorption and Ti-O deposition versus the first cycle, respectively. This increase could be due to protamine adsorbing to pore walls of the first Ti-O layer. In both cycles protamine represented ~16% of the total mass gain, revealing the greater Ti-O deposition to be due to the presence of additional protamine, and not an effect of the process occurring on Ti-O vs. SiO$_2$. It should be noted that this experiment represents a real-time observation of the protamine-induced LbL deposition of Ti-O demonstrated by Fang, *et al* and observed with AFM in Chapter 1.[3,16]

To begin identification of the minimum arginine content necessary for a 16-mer peptide to perform LbL deposition, the peptides R$_4$R$_4$S$_7$, R$_3$R$_3$S$_9$, and R$_2$R$_2$S$_{11}$ were subjected to QCM analysis. The results are displayed in **Figure 5.4** and show R$_2$R$_2$S$_{11}$ largely desorbed from the sensor during washing. In fact, when TiBALDH entered the sample chamber any remaining R$_2$R$_2$S$_{11}$ desorbed from silica, leaving the sensor bare. R$_3$R$_3$S$_9$ and R$_4$R$_4$S$_7$ were both able to perform LbL mineral deposition, but there were differences between the two peptides. They showed similar adsorption (within 2.5 ng cm^{-2}, just above noise), but displayed different responses during Ti-O deposition. Both exhibited an initial ~88.5 ng cm^{-2} mass addition, and both showed subsequent partial desorption of material from the sensor. However, upon stabilization of the frequency after washing R$_3$R$_3$S$_9$ showed an overall Ti-O deposition of 11.9 ± 3.3 ng cm^{-2}, while that of R$_4$R$_4$S$_7$ was 62.4 ± 2.0 ng cm^{-2}. The species that desorbed Ti-O deposition is not
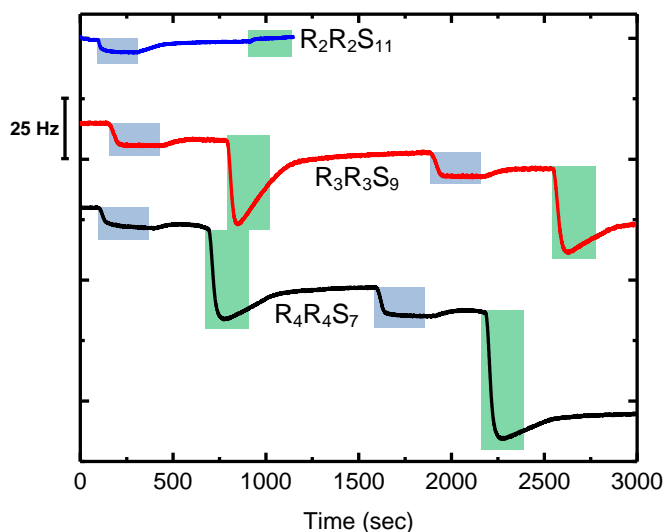
Figure 5.4: QCM observation of synthetic peptide adsorption and Ti-O deposition. The peptides were observed during adsorption and Ti-O deposition on silica-coated quartz sensors. Blue-shaded regions indicate peptide in the sample chamber, while green-shaded regions indicate TiBALDH in the sample chamber. Un-shaded regions denote washing buffer in the sample chamber.

known. It could be nascent Ti-O nanoparticles that do not remain associated with the adsorbed peptide, or perhaps these peptides have some preference to adsorb to the surface of Ti-O, causing desorption of some peptide along with newly-formed Ti-O. Ultimately, both peptides were able to adsorb to the new Ti-O surface and deposit a new Ti-O layer, and both deposited more Ti-O in the second layer versus the first (57.1 ± 3.0 ng cm^{-2} and 104.9 ± 2.5 ng cm^{-2} Ti-O for $R_3R_3S_9$ and $R_4R_4S_7$, respectively). These results, along with QCM observation of protamine in **Figure 5.3**, indicate that higher arginine content yields both a higher amount of Ti-O deposition and a lower degree of material desorption from the surface.

Since $R_2R_2S_{11}$ completely desorbed and $R_3R_3S_9$ exhibited much desorption upon TiBALDH exposure, continued research focused around this arginine content. 16-mer

peptides containing five, six, or seven arginine residues were tested to identify the arginine content necessary for LbL mineral deposition. In these peptides all arginine residues were clustered at either the N- or C-terminus. Also, 5-mer and 6-mer peptides consisting solely of arginine were also tested. The results are in **Table 5.3** and revealed new questions in this investigation. The peptides nR_5S_{10} and nR_6S_9 desorbed during TiBALDH exposure, while their C-terminally clustered counterparts, cR_5S_{10} and cR_6S_9, were both able to perform LbL mineralization. These results indicate the N- and /or C-termini may play a prominent role in adsorption and/or mineralization.

Interestingly, nR_7S_8 was able to perform LbL mineralization, indicating seven consecutive arginine residues at the N-terminus are sufficient to keep the peptide and Ti-O associated with the foundation. Also, comparison of R_5 and R_6, both with 100% arginine, showed arginine content to not be the sole characteristic necessary for LbL deposition, as R_5 could not perform LbL deposition, but R_6 did. This comparison shows that while arginine alone can induce surface deposition of Ti-O, the arginine oligomer must meet a minimum length requirement to deposit Ti-O successfully.

Table 5.3: Change in mass association on silica-coated quartz crystal sensors upon peptide adsorption and attempted Ti-O deposition of N- and C-terminally arginine-clustered 16-mer peptides. The standard deviation is the noise recorded upon reaching an equilibrium resonance frequency.

Sequence	1st round Δm (ng cm^{-2})		2nd round Δm (ng cm^{-2})	
	Peptide	Ti-O	Peptide	Ti-O
nR_5S_{10}	13.1 ± 0.6	-11.1 ± 1.3	N.A.	N.A.
nR_6S_9	28.8 ± 2.0	-20.2 ± 2.3	N.A.	N.A.
nR_7S_8	36.4 ± 0.5	100.6 ± 0.6	32.6 ± 0.5	135.8 ± 0.5
cR_5S_{10}	6.1 ± 0.3	15.7 ± 0.6	10.1 ± 0.3	21.0 ± 0.6
cR_6S_9	11.6 ± 1.5	25.5 ± 2.0	15.4 ± 2.0	16.2 ± 2.3
R_5	6.8 ± 0.6	1.0 ± 0.5	N.A.	N.A.
R_6	9.1 ± 0.3	23.8 ± 0.3	10.6 ± 2.0	30.6 ± 0.6

5.4.2 Effect of Arginine Cluster Size and Distribution

The ability of cR_6S_9 to perform LbL deposition while nR_6S_9 could not indicated the distribution of cationic residues in peptides to be important to mineral deposition. Therefore, several 16-mer peptides containing 6-9 arginine residues in various cluster lengths and distributions were probed via QCM measurement. First, 6- and 8-arginine-containing 16-mers were tested wherein the cationic residues were clustered or separated throughout the peptide chain. The results are displayed in **Table 5.4**, combined with the results of $R_3R_3S_9$ and $R_4R_4S_7$. eR_8S_7, with the arginine residues distributed equally throughout the peptide chain, performed LbL deposition, but with much less material deposition than $R_4R_4S_7$. For peptides containing six arginine residues, reducing the arginine cluster size below three resulted in no LbL deposition ($R_2R_2R_2S9$ and eR_6S_9). This results also showed 16-mer peptides containing six arginine residues to be very sensitive in their adsorption and Ti-O deposition ability. It would be worthwhile to probe seven-arginine peptides with these same arginine cluster sizes and distributions. Since eR_6S_9 could not deposit Ti-O but eR_8S_7 could, a 16-mer peptide with seven arginine residues may have the minimum arginine content necessary for LbL deposition regardless of their distribution.

Table 5.4: Results of QCM observation of peptide adsorption and Ti-O deposition with 6- and 8-arginine containing peptides. The standard deviation is the noise recorded upon reaching an equilibrium resonance frequency.

Sequence	1st round Δm (ng cm^{-2})		2nd round Δm (ng cm^{-2})	
	Peptide	Ti-O	Peptide	Ti-O
eR_6S_9	5.3 ± 1.3	-3.8 ± 1.3	N.A.	N.A.
$R_2R_2R_2S_9$	10.9 ± 1.8	-7.1 ± 1.8	N.A.	N.A.
$R_3R_3S_9$	18.8 ± 1.8	11.9 ± 3.3	18.0 ± 2.5	57.1 ± 3.0
$R_4R_4S_7$	20.5 ± 1.8	62.4 ± 2.0	27.0 ± 2.0	104.9 ± 2.5
eR_8S_7	10.4 ± 1.3	4.6 ± 0.6	11.9 ± 1.3	7.1 ± 1.3

The effects of arginine cluster distribution with respect to the N- and C-termini were also tested with peptides containing seven and nine arginine residues split into two clusters. These clusters differed in content by only one arginine residue, and the placement of the larger cluster was switched between the N- and C-termini of the peptides. The results of QCM observation of these peptides are organized in **Table 5.5**. Both sets of peptides exhibited similar Ti-O deposition characteristics in that, when the larger arginine cluster was placed at the C-terminus, more Ti-O was deposited. These results are consistent with the results reported in **Table 5.3**, wherein C-terminally clustered arginine residues could perform LbL mineral deposition while some N-terminally clustered arginine residues could not. It could be that when all cationic groups (arginine and the N-terminus) are clustered together they preferably adsorb to a nascent Ti-O nanoparticle, desorbing from the surface. The results displayed in **Tables 5.4 and 5.5** demonstrate the influence of the distribution of cationic residues within a peptide chain. As the N-terminus was shown to affect the adsorption and mineral deposition of peptides, future experiments with peptides which have acetylated N-termini will enable the isolated study of arginine cluster size and distribution.

Table 5.5: Change in mass association on silica-coated quartz crystal sensors upon peptide adsorption and attempted Ti-O deposition of 16-mer peptides containing uneven clusters of arginine residues. The standard deviation is the noise recorded upon reaching an equilibrium resonance frequency.

Sequence	1st round Δm (ng cm^{-2})		2nd round Δm (ng cm^{-2})	
	Peptide	Ti-O	Peptide	Ti-O
$R_3R_4S_8$	27.8 ± 0.5	53.4 ± 1.3	18.0 ± 1.0	46.8 ± 1.0
$R_4R_3S_8$	14.2 ± 0.5	18.4 ± 0.5	14.9 ± 0.6	28.3 ± 0.5
$R_4R_5S_6$	19.5 ± 0.5	72.3 ± 0.6	22.8 ± 0.6	89.8 ± 0.5
$R_5R_4S_6$	18.4 ± 0.3	43.2 ± 0.6	20.2 ± 0.6	63.0 ± 1.0

5.4.3 Effect of N- and C-termini on Adsorption and Deposition

QCM observations have consistently shown that, as arginine residues are placed closer to the N-terminus, peptides either deposit less Ti-O or desorb during TiBALDH exposure. It is also evident that peptides containing six arginine residues exhibit Ti-O deposition that is highly dependent on the arginine cluster size and distribution. Therefore, six-arginine peptides were selected to investigate the effect of the N- and C-termini on mineral deposition. The peptide cR_6S_9 was modified via acetylation of the N-terminus and/or amidation of the C-terminus. These results are tabulated in **Table 5.6** and show that deletion of the N-terminal primary amine group decreases peptide adsorption and, subsequently, Ti-O deposition. Interestingly, addition of an amide group at the C-terminus improved peptide adsorption and mineral deposition, in contrast to nR_6S_9, which desorbed during Ti-O deposition. This difference could indicate that amide groups interact with surfaces and mineral precursor molecules differently than amine groups, which can be tested with peptides in which the arginine residues have been replaced with glutamine.

Table 5.6: Change in mass association silica-coated quartz crystal sensors upon peptide adsorption and Ti-O deposition terminally modified cR$_6$S$_9$. The standard deviation is the noise recorded upon reaching an equilibrium resonance frequency.

Sequence	1st round Δm (ng cm^{-2})		2nd round Δm (ng cm^{-2})	
	Peptide	Ti-O	Peptide	Ti-O
cR$_6$S$_9$	11.6 ± 1.5	25.5 ± 2.0	15.4 ± 2.0	16.2 ± 2.3
Ac-cR$_6$S$_9$	7.1 ± 0.5	19.2 ± 1.8	11.1 ± 0.5	19.2 ± 1.3
cam-cR$_6$S$_9$	20.2 ± 0.3	76.1 ± 0.6	18.4 ± 0.5	97.6 ± 1.0
camAc-cR$_6$S$_9$	10.4 ± 0.5	25.5 ± 0.5	11.9 ± 0.5	31.6 ± 0.6

5.4.4 Substitution of Serine to Alanine

Thus far, this investigation has focused on arginine and its role in the adsorption and mineralization process. To assess the contribution of hydroxyl groups to adsorption and deposition, serine residues were replaced with alanine. While alanine's methyl side chain increases the hydrophobicity of the peptide, its size is similar to that of serine, thus controlling for any influence of sterics. Peptides containing six arginine residues were selected for alanine substitution since they displayed such sequence-dependent adsorption and deposition abilities (**Tables 5.4 and 5.6**). The peptide R$_3$R$_3$S$_9$ was subjected to both partial and full serine substitution, and the adsorption and mineral deposition characteristics of these peptides were observed using a QCM. Two partially substituted peptides were tested, one in which the serine residue adjacent to the C-terminal arginine cluster was changed to alanine, and another where half of the non-arginine residues were alanine, evenly spread out between the arginine clusters. The QCM measurement results are displayed in **Table 5.7**.

Table 5.7: Change in mass association silica-coated quartz crystal sensors upon peptide adsorption and Ti-O deposition of six-arginine, 16-mer peptides containing serine and alanine residues. The standard deviation is the noise recorded upon reaching an equilibrium resonance frequency.

Sequence	1st round Δm (ng cm^{-2})		2nd round Δm (ng cm^{-2})	
	Peptide	Ti-O	Peptide	Ti-O
$R_3R_3S_9$	18.8 ± 1.8	11.9 ± 3.3	18.0 ± 2.5	57.1 ± 3.0
$R_3R_3S_8A$	19.5 ± 2.0	3.8 ± 2.3	16.7 ± 1.8	11.1 ± 2.3
$R_3R_3S_5A_4$	12.4 ± 2.0	1.8 ± 1.8	N.A.	N.A.
$R_3R_3A_9$	16.2 ± 2.0	-8.3 ± 2.0	N.A.	N.A.

As more serine residues were substituted with alanine a concomitant decrease in Ti-O deposition was observed. $R_3R_3S_8A$, in which the serine adjacent to the C-terminal arginine cluster was replaced with alanine, showed a >50% decrease of Ti-O deposition in both layers. QCM observation of $R_3R_3S_8A$, in which the alanine is adjacent to the N-terminal arginine cluster, would yield information on the prevalence of one cluster over the other in terms of adsorption and mineral deposition. For $R_3R_3S_5A_4$, in which half of the serine residues had been exchanged for alanine, the peptide did not exhibit Ti-O deposition above noise. Once all serine residues had been exchanged for alanine ($R_3R_3A_9$) there was a net desorption of material upon TiBALDH exposure.

These peptides show the exchange of serine for alanine to be detrimental to the mineral deposition ability of the peptide. However, these experiments yield no information as to whether serine contributes to mineral deposition or if alanine inhibits it. A firm answer would require elucidating the mechanism of peptide-induced mineralization, but insight can be gained by QCM observation of R_3R_3 peptides in which serine residues are substituted for glycine in a pattern identical to the alanine substitutions presented in **Table 5.2**. These peptides would still represent a deletion of hydroxyl side

chains while not contributing the hydrophobic side chain of alanine. It is also possible that alanine changes the secondary conformation of the peptide. This change could affect the arrangement of arginine side groups in a conformation favorable for deposition; a phenomenon observed by Mermut, *et al* for the adsorption of lysine-leucine 14-mers.[14]

5.4.5 Effect of Experimental Conditions on Adsorption and Mineral Deposition

During initial tuning of experimental conditions for QCM measurements, some interesting observations were made that are worth noting for future research. First, the buffering salt used can affect both the sensitivity of QCM measurements and mineral deposition ability of some synthetic peptides. In Chapter 1 Tris-HCl was used to pH buffer solutions, and it was initially used in QCM measurements. However, Tris-HCl on its own displayed a 25.3 ± 2.3 ng cm^{-2} adsorption to the sensor, while Na-P contributed only a 5.1 ng cm^{-2} adsorption to silica-coated QCM sensors (data not shown). The five-arginine peptide $R_3R_2S_{10}$ was subjected to QCM observation in 50 mM Tris-HCl and 50 mM Na-P, both pH 7; the comparison of these measurements can be seen in **Figure 5.5**. A net 10.4 ± 0.3 ng cm^{-2} adsorption of the peptide was observed in Tris-HCl, while it was 19.2 ± 1.3 ng cm^{-2} in Na-P buffer. This result in agreement with the findings of Gertler, *et al* on peptide adsorption to titania.[12] However, when Ti-O deposition was attempted in Tris-HCl there was a net mass addition of 18.2 ± 1.0 ng cm^{-2}, while attempting deposition in Na-P resulted in full desorption of the peptide.

Future investigations of this observation should be focused towards a wider study comparing the mineral deposition ability of peptides in different buffering salts, such as phosphate/citrate and HEPES. This study could reveal more differences in peptide-
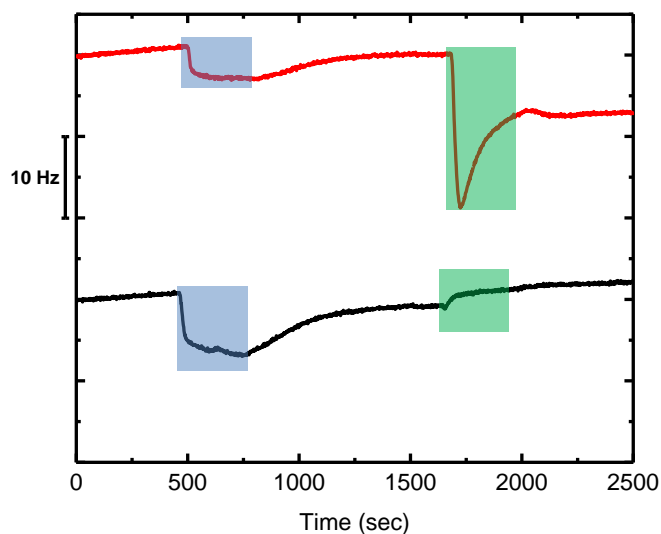
Figure 5.5: QCM observation of $R_3R_2S_{10}$ adsorption and Ti-O deposition. The experiment was performed in **Tris-HCl** and **Na-P**, both pH 7. Blue-shaded regions indicate peptide in the sample chamber, while green-shaded regions TiBALDH in the sample chamber. Un-shaded regions denote washing buffer in the sample chamber.

induced mineral deposition, ultimately allowing one to tune the thickness of deposited mineral oxide layers by performing deposition in different buffering salts.

Another experimental condition that affected the mineral deposition characteristics of synthetic peptides was the concentration of TiBALDH used during QCM observation. The results of attempting Ti-O deposition using $R_4R_4S_7$ with TiBALDH concentrations of 1, 5, and 20 mM are shown in **Figure 5.6**. As the TiBALDH concentration increased the overall Ti-O deposition decreased, and at 20 mM TiBALDH there was no net mass addition during Ti-O deposition. However, the temporary drop in frequency indicated that an interaction of TiBALDH and adsorbed $R_4R_4S_7$ did occur.
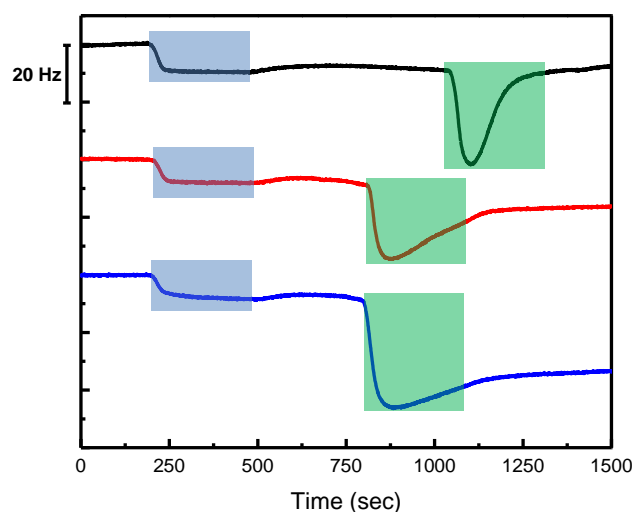
Figure 5.6: QCM observation of R$_4$R$_4$S$_7$ adsorption and Ti-O deposition at different TiBALDH concentrations. The experiment was performed in **1 mM**, **5 mM**, and **20 mM** TiBALDH. Blue-shaded regions indicate peptide in the sample chamber, while green-shaded regions indicate TiBALDH in the sample chamber. Un-shaded regions denote washing buffer in the sample chamber.

The temporary drop in frequency, coupled with no net mass addition, could be due to either the formation of Ti-O nanoparticles, which then desorb from the surface, or perhaps some Ti-O remains adsorbed while some peptide desorbs. Partial mass desorption during Ti-O deposition was also seen in **Figure 5.4** for R$_3$R$_3$S$_9$ and R$_4$R$_4$S$_7$, and the cause could not be determined by optical probing for peptide in the flow-through, because any desorbed peptide will precipitate Ti-O in solution. Also, any Ti-O nanoparticles in solution could have desorbed from the surface, so observing for turbidity would not be an indication of peptide desorption. This problem can be investigated using fluorescently labeled peptides, as the fluorescence could be detected even in a turbid solution. While this approach would not be quantitative, it would prove the cause of desorption seen during Ti-O deposition. If no fluorescent peptide is present in the flow-

through, a turbid solution would indicate desorption of nascent Ti-O nanoparticles from the peptide-coated surface.

5.5 Conclusions

The research presented here on the structure-function correlations of 16-mer peptides to adsorb to silica and TiO, and deposit Ti-O has demonstrated the many aspects which contribute to these processes. It has also been shown that high arginine content in a peptide alone is not sufficient for deposition of Ti-O, as R_5 could not perform LbL mineralization but R_6 could. In 16-mer peptides the presence of six arginine residues is enough to yield secure adsorption to silica, but the distribution of arginine residues is critical to the Ti-O deposition ability of these peptides. It was observed that non-cationic residues influence the mineral deposition ability of peptides, as the substitution of just one serine residue for alanine in $R_3R_3S_9$ caused a decrease in Ti-O deposition. However, it could not be determined if this effect was due to the inclusion of a hydrophobic side chain or the exclusion of a hydroxyl side chain. Finally, QCM observations revealed the buffering salt used to control pH can also influence the Ti-O deposition ability of peptides, and also that increasing the TiBALDH concentration can be detrimental to the Ti-O deposition ability of $R_4R_4S_7$.

The immediate future experiments of this study were discussed following experimental results in the previous section, as they addressed the question raised by the corresponding results. Looking ahead, investigation can continue by studying the structure-function correlations of arginine content at and above the threshold of mineral deposition ability. The Ti-O deposition ability of 16-mer peptides with six arginine

residues was strongly dependent on arginine cluster size and distribution, while all 16-mer peptides with eight arginine residues tested deposited Ti-O. Studying 16-mer peptides with the same sequence motifs but different arginine content will provide a more informative picture of the phenomenon occurring on peptide-coated surfaces when exposed to a mineral precursor. For instance, $R_3R_3S_9$ could perform LbL mineralization while eR_6S_9 could not, while $R_4R_4S_7$ and eR_8S_7 could perform LbL mineralization, but eR_8S_7 deposited far less Ti-O. This comparison shows that de-clustering arginine residues is detrimental to mineral deposition, and also changes the minimum arginine content necessary for LbL mineralization.

Also, studying these same peptides in which serine residues are exchanged for non-hydroxyl amino acids will reveal greater information on how the side chain functionality of non-amine residues affects adsorption and mineral deposition. These studies should be coupled with CD spectroscopy to investigate any secondary structures present in these peptides. With the vast library of possible sequences to study, it would be prudent to group side chains together in terms of similar size or functionality (i.e., hydrophobic, cationic, anionic, etc.). For instance, comparing the LbL mineralization performance of eR_8S_7 to eR_8E_7, wherein the serine residues are replaced with glutamate, could show that anionic residues cancel out the electrostatic interactions of arginine with mineral oxide surfaces.

The utilization of a quartz crystal microbalance has proven very effective in providing insight into the system-scale dynamics of peptide-induced mineral deposition, but the need for single molecule investigation is critical to better the understanding of QCM measurements. Different amounts of the peptides used in this chapter remained

adsorbed during washing, suggesting they may exhibit different adhesion forces or have different footprints on the sensor surface. To study adhesion, Atomic Force Microscopy can be used to quantify the strength of peptide adsorption, as shown in the literature.[14,17-19] This technique could be valuable in comparing the adhesion forces of peptides with identical arginine content but different cluster size and distribution. This study could also be performed on peptides adsorbed to deposited Ti-O layers, opening up the comparison of adhesion forces of a peptide on starting foundations and newly-deposited mineral oxides.

Multiple studies of peptide adsorption have employed Sum Frequency Generation (SFG) vibrational spectroscopy to investigate the interaction of peptide moieties both before and after immobilization.[13,14,20,21] This nonlinear optical technique can be performed on adsorbed peptides to probe the functional groups interacting with the adsorbing surface. Performing SFG measurements both before and after mineral deposition could provide insight into any structural changes peptides undergo during the deposition process. In addition to identifying the functional groups which interact with a surface, the presence of any secondary structure of peptides could prove important to both SFG spectroscopy and AFM measurements. Phillips, *et al*. investigated this property using CD spectroscopy, and revealed that an amphiphilic 14-mer peptide containing alternating lysine and leucine residues exhibited an α-helical structure, translating to the lysine side chains in the same orientation.[13] This structure could allow for stronger adsorption of the peptide, since the amine groups could all be oriented towards a hydrophilic surface. However, with all hydrophobic leucine side chains facing solution, mineral deposition could be inhibited by repulsion of precursor molecules.

5.6 Materials & Methods

5.6.1 Peptide Solution Preparation

Peptides were ordered from Genscript, Inc., Piscataway, NJ, USA; and prepared by Yixin Zhang, B-CUBE, TU Dresden, Germany; they were received as lyophilized powders. The peptides were dissolved in sodium phosphate buffer at pH 7 (10 mM) to a concentration of 20 $^{mg}/_{mL}$ based on the specific peptide mass (total powder mass multiplied by the purity as a decimal). The solutions were put in 1.5 mL tubes in 25 μL aliquots, flash frozen in liquid nitrogen, and stored at -20 °C until used.

5.6.2 Quartz Crystal Microbalance Measurements

Adsorption and mineral deposition of synthetic peptides was tested using QCM to monitor the real-time peptide adsorption and desorption from sensor surfaces, as well as the deposition of Ti-O coatings. All sensors, modules, and instruments were attained from Biolin Scientific, Inc., Linthicum Heights, MD, USA. The sensors used were gold-on-quartz, 14 mm diameter, 0.3 mm thick, <3 nm RMS roughness, and coated with a 50 nm thick layer of amorphous silica; the sensors resonate at a fundamental frequency of 4.95 MHz ± 50 Hz. The instruments used were the Q-Sense E1 and E4. These differed only in that the E4 allows for the monitoring of four sensors simultaneously while the E1 can only monitor a single sensor. The sensors were placed in a flow module and subjected to the constant flow of various solutions over the sensors while monitoring the change in resonance frequency of the sensor.

The sensors were prepared for experimentation by placement in a UV/ozone chamber (BioForce Nanosciences, Inc., Ames, IA, USA) for 10 min, followed by incubation in 2% SDS for 30 min at RT. Finally, the sensors were washed thoroughly

with ultrapure H_2O dried under a stream of 99.999% pure nitrogen gas. Finally, they were again placed in the UV/ozone chamber for 10 min.

Solutions of peptide, buffer, or TiBALDH were flowed over resonating sensors using a peristaltic pump. As material adsorbed/desorbed to/from the sensor surface the change in frequency was monitored using the associated software (QSoft, also from Biolin Scientific). A flow rate of 75 µL min^{-1} was used for all solutions. Peptide solutions had a concentration of 0.10 mg mL^{-1}, TiBALDH was used primarily at a concentration of 1 mM (concentrations of 5 mM and 20 mM were used where indicated). The peptides and TiBALDH were diluted in 50 mM Na-P pH 7. The same buffer was used for washing steps. Unless otherwise noted, peptide and TiBALDH solutions were flowed over the sensor for a period of five minutes, whereas wash solutions were flowed over the sensor until the frequency change stabilized for a period of approximately 2 minutes. A stabilization of frequency change indicated that adsorption/desorption had either ceased or at least reached a state of equilibrium. For all samples the seventh harmonic frequency was used for data analysis.

After experiments were completed the sensor and module were washed with 2% SDS at a flow rate of 0.579 mL min^{-1} (maximum flow rate) for 10 min, followed by ultrapure H_2O flow for 10 min (at maximum flow rate), and then dried under a steady stream of 99.999% pure nitrogen gas. The sensors were then exposed to 10 min of UV/ozone treatment and stored in a padded case until future use. Final plotting and analysis of data was performed using Microcal Origin v.8.5 (OriginLab Corporation, Northampton, MA, USA).

5.7 References

1.   Mizutani, T., Nagase, H., Fujiwara, N., and Ogoshi, H. (1998) Silicic Acid Polymerization Catalyzed by Amines and Polyamines, *Bull. Chem. Soc. Jpn. 71*, 2017.

2.   Kröger, N., Deutzmann, R., and Sumper, M. (1999) Polycationic Peptides from Diatom Biosilica That Direct Silica Nanosphere Formation, *Science 286*, 1129.

3.   Fang, Y., Wu, Q., Dickerson, M. B., Cai, Y., Shian, S., Berrigan, J., Poulsen, N., Kröger, N., and Sandhage, K. H. (2009) Protein-Mediated Layer-by-Layer Syntheses of Freestanding Microscale Titania Structures with Biologically Assembled 3-D Morphologies, *Chem. Mater. 21*, 5704.

4.   Filocamo, S., Stote, R., Ziegler, D., and Gibson, H. (2011) Entrapment of DFPase in titania coatings from a biomimetically derived method, *J. Mater. Res. 26*, 1042.

5.   Belton, D. J., Patwardhan, S. V., Annenko, V. V., Danilovtseva, E. N., and Perry, C. C. (2008) From biosilicification to tailored materials: Optimizing hydrophobic domains and resistance to protonation of polyamines, *Proc. Natl. Acad. Sci. 105*, 5963.

6.   Ahn, S., Park, S., and Lee, S.-Y. (2011) Oligo(L-lysine)-induced titanium dioxide: Effects of Consecutive Lysine on Precipitation, *J. Crystal Growth 335*, 100.

7.   Kim, D. J., Lee, K.-B., Chi, Y. S., Kim, W.-J., Paik, H.-j., and Choi, I. S. (2004) Biomimetic Formation of Silica Thin Films by Surface-Initiated Polymerization of 2-(Dimethylamino)ethyl Methacrylate and Silicic Acid, *Langmuir 20*, 7904.

8.   Coradin, T., and Lopez, P. J. (2003) Biogenic Silica Patterning: Simple Chemistry or Subtle Biology?, *ChemBioChem 3*, 1.

9.   Cha, J. N., Stucky, G. D., Morse, D. E., and Deming, T. J. (2000) Biomimetic synthesis of ordered silica structures mediated by block copolypeptides, *Nature 403*, 289.

10.   Knecht, M. R., and Wright, D. W. (2003) Functional analysis of the biomimetic silica precipitating activity of the R5 peptide from Cylindrotheca fusiformis†, *Langmuir 20*, 4728.

11.   Jiang, Y., Yang, D., Zhang, L., Sun, Q., Sun, X., Li, J., and Jiang, Z. (2009) Preparation of Protamine–Titania Microcapsules Through Synergy Between Layer-by-Layer Assembly and Biomimetic Mineralization, *Adv. Funct. Mater. 19*, 150.

12.   Gertler, G., Fleminger, G., and Rapaport, H. (2010) Characterizing the Adsorption of Peptides to TiO$_2$ in Aqueous Solutions by Liquid Chromatography, *Langmuir 26*, 6457.

13.   Phillips, D. C., York, R. L., Mermut, O., McCrea, K. R., Ward, R. S., and Somorjai, G. A. (2007) Side Chain, Chain Length, and Sequence Effects on Amphiphilic Peptide Adsorption at Hydrophobic and Hydrophilic Surfaces Studied by Sum-Frequency Generation Vibrational Spectroscopy and Quartz Crystal Microbalance, *J. Phys. Chem. C 111*, 255.

14.   Mermut, O., Phillips, D. C., York, R. L., McCrea, K. R., Ward, R. S., and Somorjai, G. A. (2006) In Situ Adsorption Studies of a 14-Amino Acid Leucine-Lysine Peptide onto Hydrophobic Polystyrene and Hydrophilic Silica Surfaces Using Quartz Crystal Microbalance, Atomic Force Microscopy, and Sum Frequency Generation Vibrational Spectroscopy, *J. Am. Chem. Soc. 128*, 3598.

15.   Sauerbrey, G. (1959) Verwendung von Schwingquarzen zur Wägung dünner Schichten und zur Mikrowägung, *Z. Phys. 155*, 206.

16.   Haase, N. R., Shian, S., Sandhage, K. H., and Kroger, N. (2011) Biocatalytic Nanoscale Coatings Through Biomimetic Layer-by-Layer Mineralization, *Adv. Funct. Mater. 21*, 4243.

17.   Yamashita, I., Kirimura, H., Okuda, M., Nishio, K., Sano, K.-I., Shiba, K., Hayashi, T., Hara, M., and Mishima, Y. (2006) Selective Nanoscale Positioning of Ferritin and Nanoparticles by Means of Target-Specific Peptides, *Small 2*, 1148.

18.   Hayashi, T., Sano, K.-I., Shiba, K., Kumashiro, Y., Iwahori, K., Yamashita, I., and Hara, M. (2006) Mechanism Underlying Specificity of Proteins Targeting Inorganic Materials, *Nano Lett. 6*, 515.

19.   Hayashi, T., Sano, K.-I., Shiba, K., Iwahori, K., Yamashita, I., and Hara, M. (2009) Critical Amino Acid Residues for the Specific Binding of the Ti-Recognizing Recombinant Ferritin with Oxide Surfaces of Titanium and Silicon, *Langmuir 25*, 10901.

20.   York, R. L., Mermut, O., Phillips, D. C., McCrea, K. R., Ward, R. S., and Somorjai, G. A. (2007) Influence of Ionic Strength on the Adsorption of a Model Peptide on Hydrophilic Silica and Hydrophobic Polystyrene Surfaces: Insight from SFG Vibrational Spectroscopy, *J. Phys. Chem. C 111*, 8866.

21.   York, R. L., Holinga, G. J., and Somorjai, G. A. (2009) An Investigation of the Influence of Chain Length on the Interfacial Ordering of L-Lysine and L-Proline and Their Homopeptides at Hydrophobic and Hydrophilic Interfaces Studied by Sum Frequency Generation and Quartz Crystal Microbalance, *Langmuir 25*, 9369.

APPENDIX A

Antimicrobial Efficacy Supplemental Data

Table A.1: Citrate capping agent control MIC/MBC Tests.

E. coli – 1 x 10^6 cfu

Sample	MIC	MBC
Citrate	N/A	N/A
Citrate + Gi	250 mM (250 $^{\mu g}/_{mL}$)	250 mM (250 $^{\mu g}/_{mL}$)
Gi	250 $^{\mu g}/_{mL}$	250 $^{\mu g}/_{mL}$
GiTo	125 $^{\mu g}/_{mL}$	125 $^{\mu g}/_{mL}$

S. Aureus – 2 x 10^5 cfu

Citrate	31.2 mM	500 mM
Citrate + Gi	15.6 mM (15.6 $^{\mu g}/_{mL}$)	15.6 mM (15.6 $^{\mu g}/_{mL}$)
Gi	7.8 $^{\mu g}/_{mL}$	7.8 $^{\mu g}/_{mL}$
GiTo	7.8 $^{\mu g}/_{mL}$	7.8 $^{\mu g}/_{mL}$

Table A.2: Tiopronin capping agent controls

E. coli – 3 x 10^5 cfu

Sample	MIC	MBC
Tiopronin	37.5 mM	75 mM
Tiopronin + Gi	75 mM (125 $^{\mu g}/_{mL}$)	75 mM (125 $^{\mu g}/_{mL}$)
Gi	125 $^{\mu g}/_{mL}$	125 $^{\mu g}/_{mL}$
GiTo	62.5 $^{\mu g}/_{mL}$	62.5 $^{\mu g}/_{mL}$

S. Aureus – 3 x 10^5 cfu

Tiopronin	4.7 mM	75 mM
Tiopronin + Gi	4.7 mM (7.8 $^{\mu g}/_{mL}$)	75 mM (125 $^{\mu g}/_{mL}$)
Gi	7.8 $^{\mu g}/_{mL}$	7.8 $^{\mu g}/_{mL}$
GiTo	3.9 $^{\mu g}/_{mL}$	3.9 $^{\mu g}/_{mL}$

Table A.3: MIC/MBC Tests with fluctuating GOx-PA:AgNP ratios.

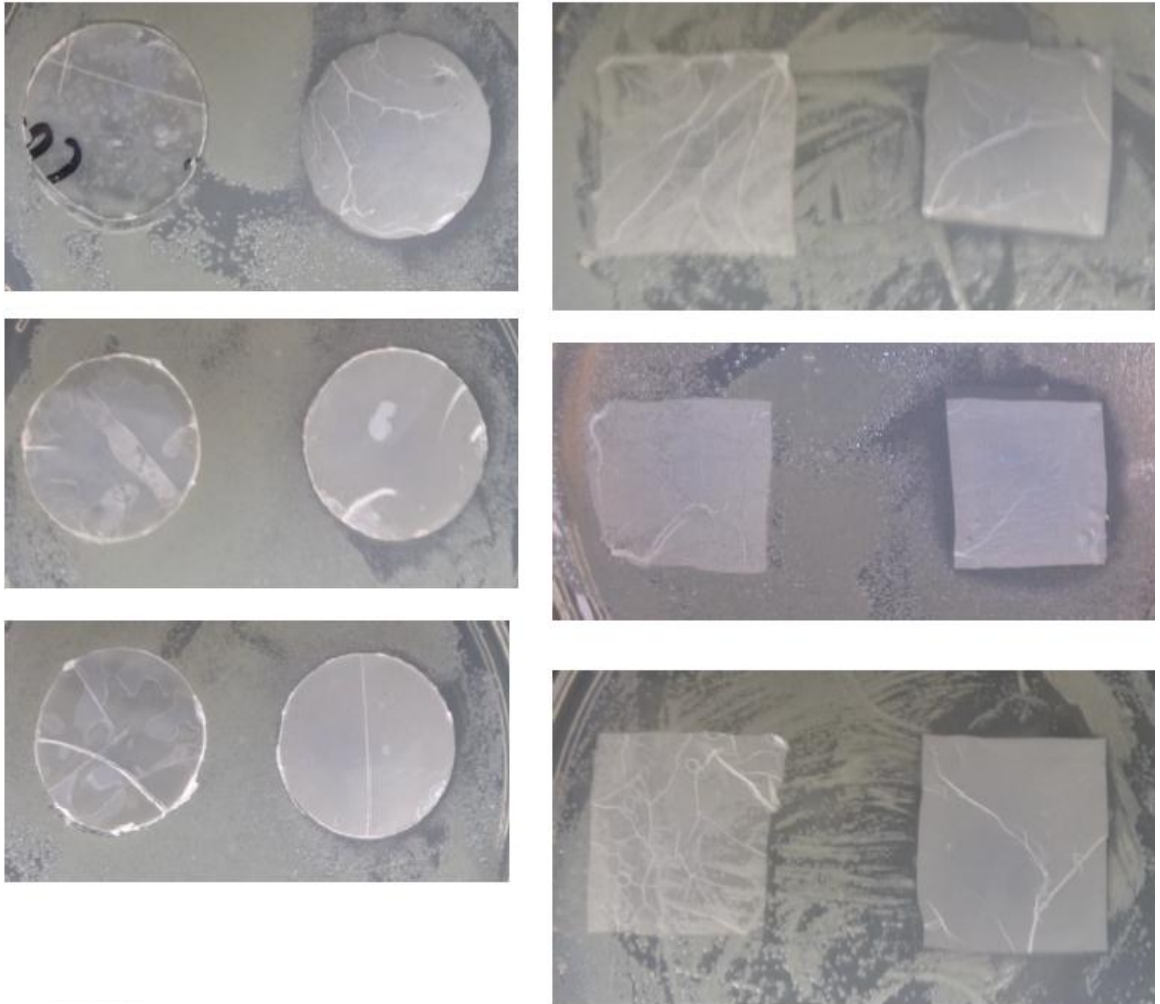| GOx-PA:AgNP (fractions vs. previous amounts)	MIC (μg/mL)	MBC (μg/mL)
$E.\ coli:\ 3\ x\ 10^5 cfu$		
1:1	62.5 – 125	62.5 – 125
1:$^1/_4$	62.5 – 125	62.5 – 125
1:$^1/_8$	62.5 – 125	62.5 – 125
1:$^1/_{32}$	125 – 250	125 – 250
$^1/_2$:1	125 – 250	250
$^1/_4$:1	250	≥250
$^1/_8$:1	250	≥250

Figure A.1: Silk clearing zone assays against *E. coli*.
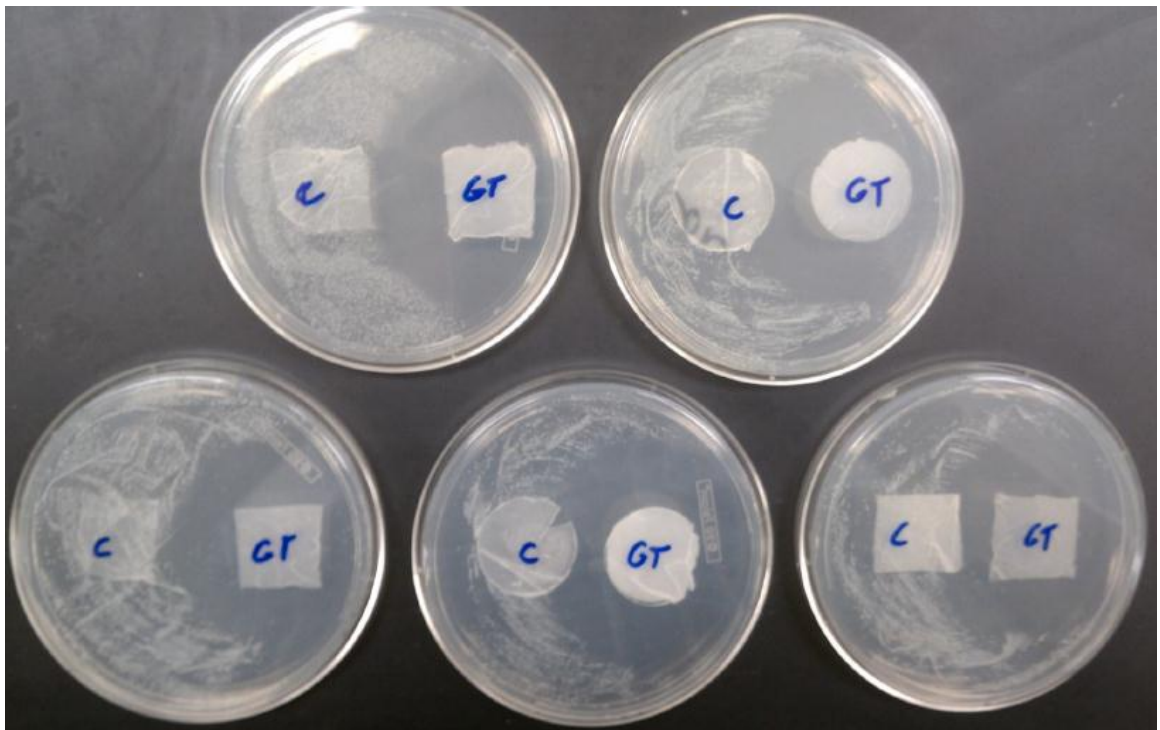
Figure A.2: Silk clearing zone assays against *S. aureus*.

APPENDIX B

Selected Sample Data

B.1 Zeta Potential Measurement Process

This section details measurement of the zeta potential of particles suspended in pH-buffered solutions. The settings used are presented, as well as the data returned by the analysis program. The instrument used in the Malvern Zetasizer Nano ZS, and the program *Zetasizer Software* was used for data collection and analysis.

To set up the software for data recording, information on the optical and electrostatic properties of both the solution and particles in suspension must be entered. **Table B.1** lists the properties needed and values entered for water. These properties are necessary so the analysis program knows the viscosity of the dispersant (how it will retard movement of particles), its refractive index (how it interacts with incident light), and the dielectric constant (how the dispersant will interact with the electric field). For water, the temperature is also entered because the aforementioned properties change with temperature. **Table B.2** lists the properties that must be specified for the material to be studied. The refractive index and absorption are important to provide information on how the particle to be measured refracts and absorbs the incident laser light.

Table B.1: The electrostatic properties of the dispersant, water, used in all zeta potential measurements in this research.

Property	Value
Dispersant	Water
Temperature	25 °C
Viscosity	0.8872 cP
Refractive Index	1.330
Dielectric Constant	78.5

Table B.2: The optical properties of polystyrene latex, the validation standard used with the instrument.

Property	Value
Material	Polystyrene Latex
Refractive Index	1.590
Absorption @ 633 nm	0.01

After specifying the properties of the dispersant and material to be studied, other settings must be entered for data recording and analysis purposes. The particle model selected for measurements in aqueous dispersants is the Smoluchowski model. This model specifies that the electrical double layer is much smaller than the particle. The instrument can heat the measurement cell, so this can be set, along with the time allowed for temperature equilibration before beginning measurement. Also, the measurement cell must be specified, and in this research the ZEN1002 Zeta dip cell was used. The measurement process is divided into individual sample runs, which are combined and averaged for one measurement. The number of runs can be specified for consistency between samples, or the measurement duration can be set to "automatic," in which case runs will be performed until the recorded data is deemed of sufficient quality by the software. The voltage between the electrodes that is used during the measurement can also be selected, though it is rarely adjusted. It is set by default to 40 V, and this was the voltage used in this research.

The final setting to be adjusted is the analysis model used to fit the data. By default, this is set to "Auto mode," which allows the software to choose the proper model based on the data recorded. "General purpose" is used for most measurements of

particles. For analyzing proteins, the "Monomodal" setting is selected. The "Low mobility" setting is chosen for materials which have zeta potentials within 2.5 mV of zero. This setting is specific for materials which are near-neutral, and thus may have particles of positive or negative zeta potential present in the sample population.

After a measurement is recorded, four key average values are returned; these are the dispersant conductivity, the particle mobility, the zeta potential, and the count rate. The dispersant conductivity, given in mS cm^{-1}, is a measure of how well the electric field was conducted through the solution. The electrophoretic mobility of the particle, reported in μmcm (Vs)$^{-1}$, is the velocity of the moving particle as a function of the electric field potential. The mobility is used to calculate the zeta potential using **Equation 1.2**. The advantage of reporting zeta potential, instead of the electrophoretic mobility, is that the zeta potential is an intrinsic property of a particle, whereas the electrophoretic mobility is dependent on the electric field in which it is placed. Finally, the average count rate is reported in kilo-counts per second (kcps). This is a measure of the amount of particles for which data was collected; a target count rate is 100 – 400 kcps. If the count rate is too low insufficient data will be collected, and if it is too high light will not be scattered by other particles in the sample and not reach the detector. The zeta potential and electrophoretic mobility are also reported graphically as a population distribution of the observed values, and usually have Gaussian distributions. The distribution curves provide insight into the uniformity of the zeta potential for a given sample by reporting the deviation of values about the mean zeta potential observed. An example of a zeta potential distribution graph is shown in **Figure B.1**, wherein the distribution of zeta potentials for the Malvern Instruments polystyrene latex standard at

pH 7 is reported. The x-axis plots the zeta potential values observed, while the y-axis plots the total number counts recorded for each zeta potential value. If the measurement returns more than one distribution of zeta potential values, i.e., multiple peaks, statistics on the mean zeta potential and total percent area of the curve for each peak is given.
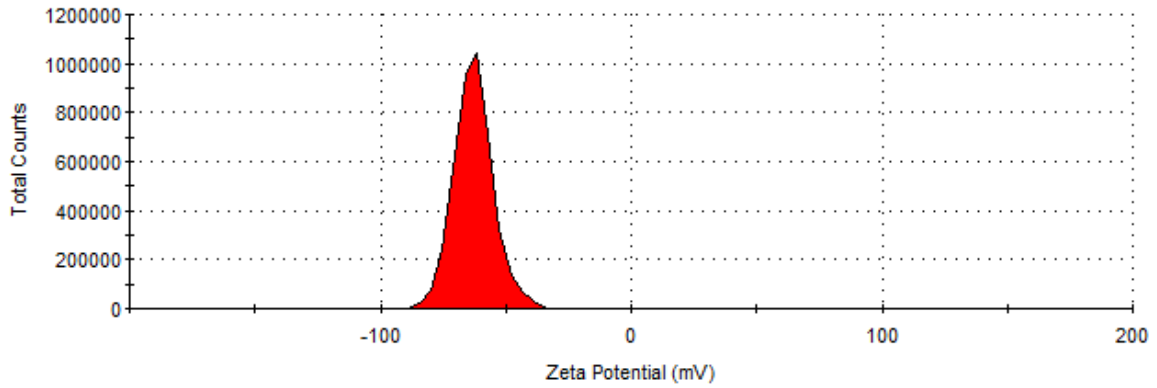

Figure B.1: Zeta potential distribution of Malvern validation standard polystyrene latex beads at pH 7.

B.2 Michaelis-Menten Kinetic Property Determination

In studying the effects of GOx-PA upon its immobilization, the Michaelis-Menten kinetic properties were investigated. The determination of the Michaelis constant, K_M, and maximum velocity, V_{max}, of the GOx-PA reaction was conducted by performing the enzymatic reaction at a range of glucose concentrations. The results are then plotted as inverse velocity of the reaction vs. the inverse glucose concentration (**Figure B.2**); this is called a Lineweaver-Burk Plot. A linear regression line is then fitted to the data, K_M is determined by calculating the negative reciprocal of the x-intercept, and V_{max} is determined by calculating the reciprocal of the y-intercept.
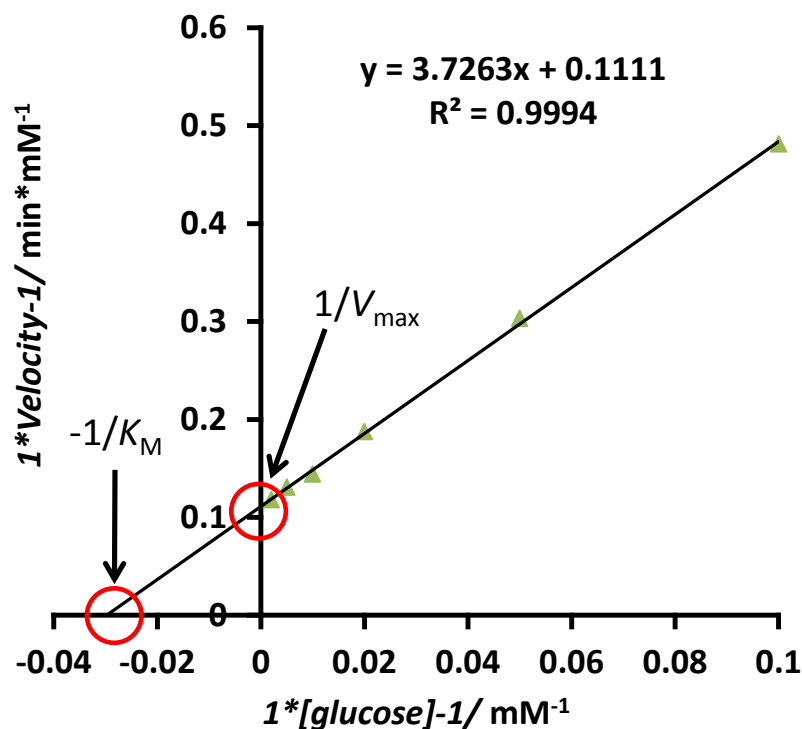
148

Figure B.2: Lineweaver-Burk Plot of GOx-PA. The x- and y-intercepts are identified, as they are used to calculate the Michaelis constant and maximum velocity.

B.3 Determination of Electrochemical Onset Potential of Oxygen Reduction

In investigating the effects of protamine cross-linking on the electrochemical activity of laccase, cyclic voltammetry measurements were conducted to identify the potential at which reduction of oxygen begins. Cyclic voltammetry records the current of an electrode while the potential is changed at a constant rate. When no electrochemical reaction is occurring the current remains constant with changing potential. However, once an electrochemical reaction begins the current will change as the potential changes; the potential where this occurs is called the onset potential. After the onset potential has been reached, the current will begin changing linearly with changing potential. In this research the onset potential was identified by first forming two linear regression lines,

one using data from the linear region before the onset potential is reached, and the other formed with data from the linear region after the electrochemical reaction has begun. The onset potential is identified as the x-coordinate where these two lines intersect. **Figure B.3** presents a graphical representation of this for a CNT-BP electrode onto which Lac-PA was immobilized. While this is not an exact method of onset potential determination, the inset in **Figure 4.6** shows that upon reaching onset potential the change in current is at first very slight, and thus difficult to concretely identify. The method presented here is a practical, repeatable method that can be applied to any cyclic voltammetry measurement.
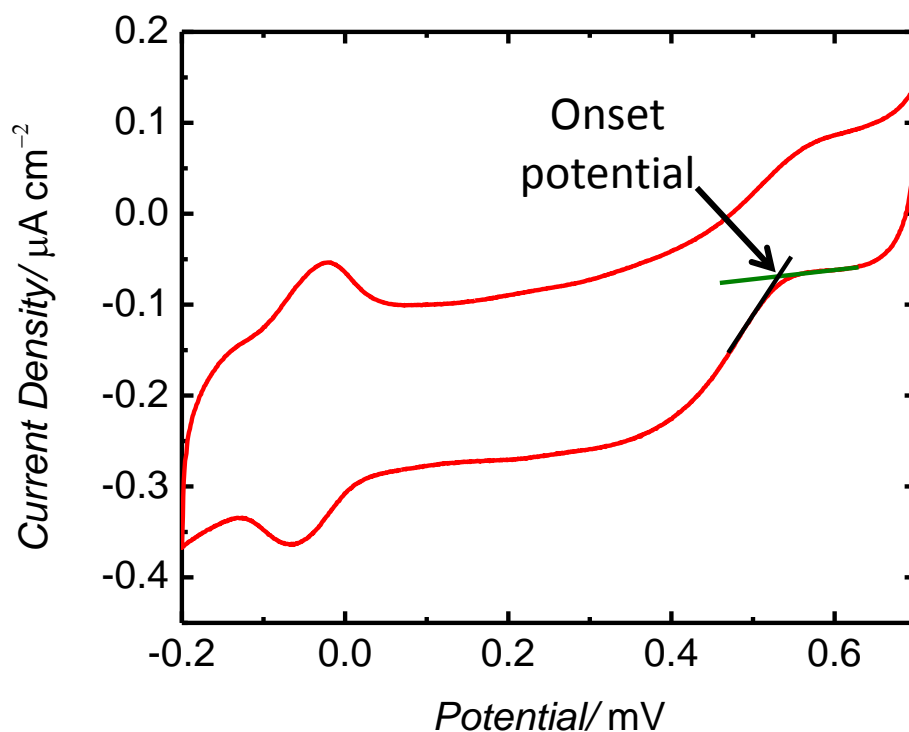

Figure B.3: **Calculation of the onset potential of oxygen reduction by Lac-PA immobilized to a CNT-BP electrode.** The regression line on the right was formed using data prior to the onset of oxygen reduction, while the regression line on the left was formed using data during a constant change in current during oxygen reduction.

VITA

Nicholas Rudy Haase was born in Plainfield, Indiana, and at age 12 moved to Martinsville, Indiana, where he attended Martinsville High School. He enrolled in Purdue University in West Lafayette, Indiana, and graduated in May 2006 with a B.S. in Biochemistry. In the summer of 2006 he moved to Atlanta, Georgia, to pursue a Doctorate in Chemistry at the Georgia Institute of Technology. Outside of school, Nick enjoys cooking, movies, music, photography, football, and auto racing.